TESIS DE LA UNIVERSIDAD
DE ZARAGOZA

2024

282

Ana Carolina Moreno Maldonado

Synthetic Magnetosomes Integrating Magnetic Hyperthermia and Chemotherapy for Synergistic Effects

Director/es

Goya Rossetti, Gerardo Fabián
Ibarra García, Manuel Ricardo

ISSN 2254-7606

Prensas de la Universidad
Universidad Zaragoza

Universidad de Zaragoza
Servicio de Publicaciones

ISSN 2254-7606

Tesis Doctoral

SYNTHETIC MAGNETOSOMES INTEGRATING MAGNETIC HYPERTHERMIA AND CHEMOTHERAPY FOR SYNERGISTIC EFFECTS

Autor

Ana Carolina Moreno Maldonado

Director/es

Goya Rossetti, Gerardo Fabián
Ibarra García, Manuel Ricardo

UNIVERSIDAD DE ZARAGOZA
Escuela de Doctorado

Programa de Doctorado en Física

2024

Synthetic Magnetosomes Integrating Magnetic Hyperthermia and Chemotherapy for Synergistic Effects

Doctoral Thesis

Ana Carolina Moreno Maldonado

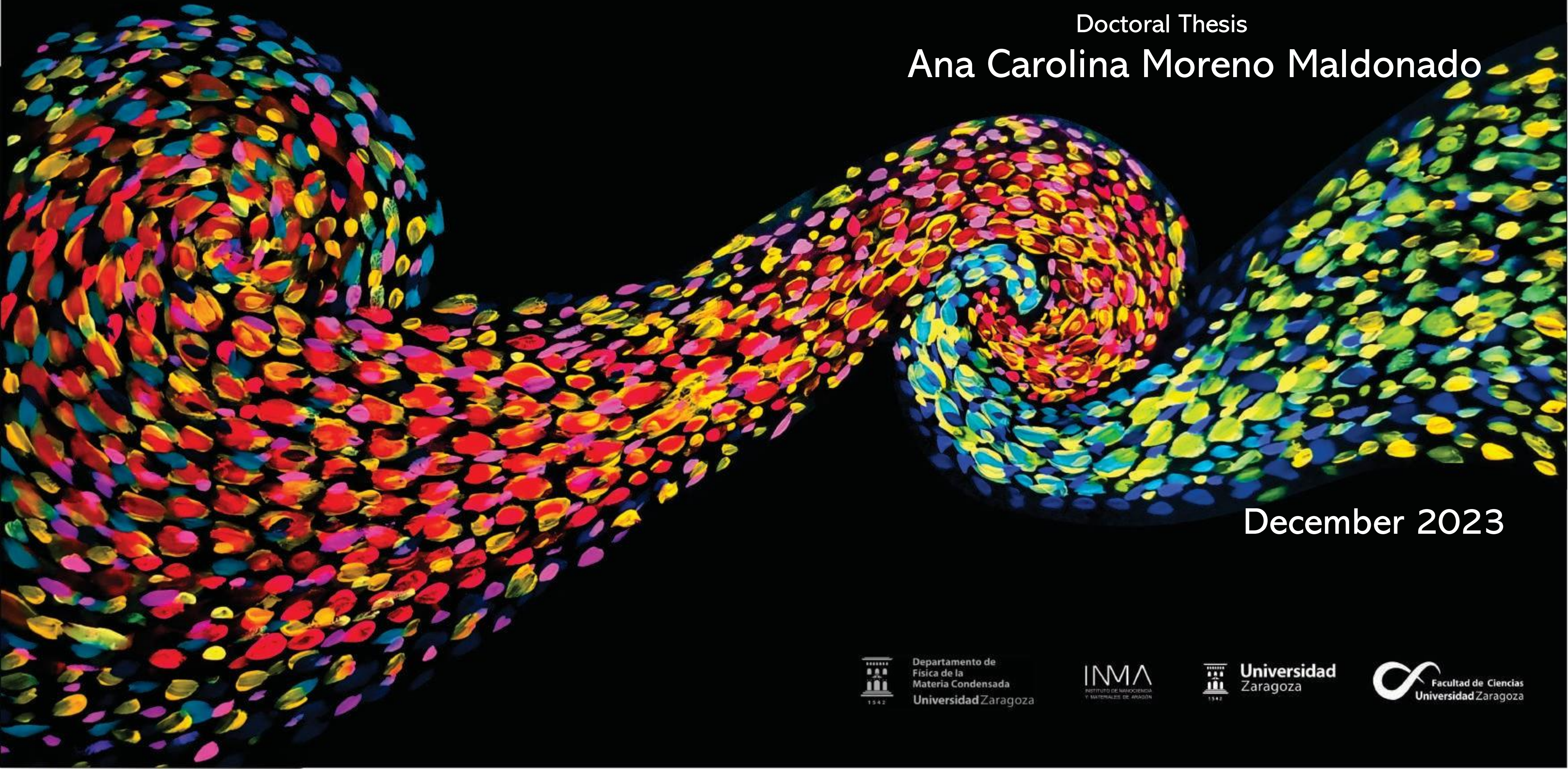

December 2023

Departamento de Física de la Materia Condensada
Universidad Zaragoza

INMA
Instituto de Nanociencia y Materiales de Aragón

Universidad Zaragoza

Facultad de Ciencias
Universidad Zaragoza

Handmade cover by Julieta Moreno.

a Pilar Eluney.

Universidad
Zaragoza
1542

Tesis Doctoral

Synthetic Magnetosomes Integrating Magnetic Hyperthermia and Chemotherapy for Synergistic Effects

Doctoral Thesis

Ana Carolina Moreno Maldonado

Supervisors

Dr. Gerardo F. Goya Rossetti
Dr. M. Ricardo Ibarra García

Facultad de Ciencias / Departamento de Física de la Materia Condensada

December 2023

Table of contents

Acknowledgments

Como dijo Cerati “Tarda en llegar, y al final hay recompensa”.

Agradecer de todo corazón a mis directores Gerardo y Ricardo sin quienes esta tesis no podría haber llegado a un buen puerto, quienes, con *muchísima paciencia*, desinterés y horas de reuniones invirtieron en mi formación profesional. Apoyando, conteniendo y alentándome, en un entorno creativo y libre para la formación y circulación de ideas. Goyita, gracias porque sin conocerme te la jugaste por mí. Te agradezco por tu infinita y admirable paciencia, por recibirme siempre con un abrazo y una sonrisa, tu buena onda, tu sinceridad y tu predisposición. Gracias por acompañarme en estos cinco años en el papel de amigo, compañeros, psicólogo, padre y jefe. Muchas gracias, Ricardo, porque con paciencia supo limarme y sacar a flote mis aptitudes y conocimientos, gracias por sus consejos, su tiempo y su profesionalismo. Gracias a su ambición, su experiencia y su buen ojo, los experimentos y el análisis de datos, alcanzan la estratosfera (aunque al inicio cueste). A ambos agradezco que sean físicos a quien admirar y aspirar.

Quiero agradecer a España por haberme acogido estos cinco años, abriéndome la puerta a infinitas oportunidades, nuevas aventuras y experiencias de vida, nuevas ideas, caminos. Agradecer a Zaragoza porque ahora puedo llamar a este nuevo lugar hogar donde he podido conocer nuevas culturas, personas y creencias; oportunidades que nunca me hubiera imaginado

Agradezco a Clarita, Miriam y Jorge por su compañía, preguntando, aconsejando, preocupándose, que con una sonrisa y un abrazo en el pasillo nos poníamos al día, compartiendo anécdotas y alientos para continuar con el reto diario. A Ignacio Molina agradezco sus charlas y su paciencia con mis preguntas bio que aplanaron e iluminaron el camino.

Nuestro grupo de investigación es pequeño, y me toca agradecer a mis colegas a los que prefiero llamar amigos, por orden de aparición. Negrito, gracias por tu buena onda, por siempre entrar cantando, golpeando a la puerta con un “Familia”, porque eso es lo que creas a tu alrededor, porque entre dicho y dicho me enseñaste desde cómo hacer una síntesis de partículas hasta cómo mejorar un mal día, siempre ofreciendo consejos aprendidos de la experiencia y levantando los ánimos, gracias porque el café de maquina sabia mejor acompañado con vos. Ay, Alfonso siempre voy a agradecer a los astros haberme cruzado con vos, agradecer por haberte tenido en el laboratorio, verte trabajar con delicadeza y precisión era un placer. Sos una hermosa persona, con un humor ácido que me saca. Gracias por las horas y horas de trabajo, que con vos se pasaban volando. Muchas gracias, Jesús por haber estado desde el comienzo hasta el final, por tu apoyo, tu aliento, por compartir tus experiencias, por tu esfuerzo. Gracias por nuestras largas charlas que comenzaban en ciencia, y terminábamos hablando de mil cosas más. Bea, admito que estaba nerviosa por conocerte, pero al instante que te vi me di cuenta de que íbamos a encajar. Gracias bella por estar en todo, por haberte puesto en el rol de madre, de psicóloga y de amiga, por las palabras justas y precisas, por preocuparte, por acomodarme las ideas, por tu abrigo y tu cariño. A este pequeño grupo lleno de personas hermosas, que siempre están sonriendo, acompañando con buenos ánimos, buena música y buena cerveza, dispuestos a darte una mano cuando se te inundaba el laboratorio, les deseo lo más hermoso y una vida llena de trampolines.

Quiero agradecer a los técnicos Íñigo, Nuria, Luis, Rodrigo, Marta, Mariano, Guillermo, Pavel, Gala, Laura, Rubén y Alfonso, porque fueron un apoyo indispensable para esta tesis y para mi formación como profesional. En cada sesión o en el pasillo me brindaron su conocimiento, aportando y mostrando interés en mi trabajo, siguiéndome en el avance de esta tesis,

preocupándose y animándome. Agradezco muchísimo su apoyo y acompañamiento en estos cinco años en el Instituto de Nanociencia y Materiales de Aragón.

Agradecer a la gente de administración, Juan, María Jesús, Rubén. Y a Carmen por ser tan atenta.

Agradecer a los compañeros de la oficina y del INMA, que hacían los días amenos y alegres, por los largos cafés, las discusiones en la oficina, las dudas, compañías, ayudas. Muchas gracias por las risas, los chocolates, por ponerle buena onda al día gracias, Miguel, Tatiana, Lara, Mario, Javier, Rubén, Flaca, Vanina, Sindy, Panos, Sonia, Furqan, Amalia, Pilar, Maricruz. Y a todas las personas que fueron y vinieron, que, con una charla del finde o ciencia y un café en mano, calentaban el alma.

Durante la tesis tuve el agrado de conocer el encanto andaluz de la mano de Rafa y Carmen. A estos dos personajes les quiero agradecer las tapas, las cañas, las discusiones dentro y fuera de la oficina, porque sé que podía contar con ustedes en cualquier momento, y conversar de cualquier tema. Gracias por su calor del sur, su aliento y buena onda, fue hermoso verlos crecer y acompañarlos en el camino de su doctorado.

A los amigos, la familia elegida, un apoyo imprescindible para la buena vida, muchas gracias por los momentos compartidos, por las cervezas, las risas, las comidas, los bailes, las discusiones, las canciones, los viajes, los desvelos juntos. Gracias por preocuparse y acompañarme, son muy importantes en mi vida y sin ustedes esta tesis tampoco hubiese sido posible. Gracias Billy, Guillaume, Jessi, Claudio, María, Laura, Simón, Iván, Hernán, Gaby, Isa, Karlita, Karen, Eric, Clarita, Florián. A Juana, y mis compis de piso Martí e Iván, que alivianaron la pandemia, y que me enseñaron las costumbres de Españas, curiosos por mi cultura y carrera, pase un muy tierno tiempo en la calle Ricla. A todos muchas gracias por su compañía y apoyo, por enseñarme sus culturas y sus países, a través de sus ojos sentí que viajé. Gracias por estos hermosos años en España.

Muchas gracias a mi familia, porque siempre puedo contar con ustedes, desde la distancia me acompañaron, alentaron e impulsaron a no parar. Son indispensables en mi vida, los amo mucho.

Muchas gracias, Beto. Sos el más hermoso compañero fiel, te amo. Gracias, por tanto, perdón por tan poco. Desearía que seas eterno.

Muchas gracias, Martín. Gracias por tu compañía, palabras, confianza, charlas de trabajo, apoyo, gracias por comprender mis sueños. Amo nuestra relación y verla madurar, volvernos cómplices, compartir metas, superarnos personalmente; no cualquiera se banca pasar de estar completamente separados por casi dos años a convivir y compartir todo, las 24 horas del día. Gracias, te amo.

A la Universidad Nacional de Tucumán, la Universidad Nacional de Cuyo y el Instituto Balseiro por darme una base sólida y las herramientas necesarias para mi trabajo como profesional. ¡Que viva la educación pública!

A todos muchísimas gracias, y ¡mañana más!

Abbreviations

DPPC	1,2-Dipalmitoyl-Sn-Glycero-3-Phosphocholine
PEG	1,2-Distearoyl-Sn-Glycero-3-Phosphoethanolamine-N-[Methoxy(Polyethylene Glycol)-2000] (Ammonium Salt)
acac	Acetylacetonate
AC	Alternating Current
AMF	Alternating Magnetic Field
AF	Amplitude Field
T_B	Blocking Temperature
k_B	Boltzmann Constant
τ_B	Brown relaxation
CT	Chemotherapy
Chol	Cholesterol
CisPt	Cis-Diamminedichloroplatinum (II) Or Cisplatinum
LC	CisPt-Loaded Liposomes
LNC	**CisPt-Loaded Synthetic Magnetosomes**
H_C	Coercive Field
D_A	Combination Drug Dose A
D_C	Critical Diameter
T_C	Curie Temperature
DODAB	Didodecyldimethylammonium Bromide
DSC	Differential Scanning Calorimetry
t_D	Doubling Time
DMEM	Dulbecco`s modified Eagle´s medium
DLS	Dynamic Light Scattering
η	Dynamic viscosity
EELS	Electron Energy Loss Spectroscopy
EDS	Energy-Dispersive X-Ray Spectroscopy
t_{CEM43}	Equivalent Minutes At 43°C
EH	External Heating
FFT	Fast Fourier Transform
T_{FST}	Final Synthesis Temperature
FT-IR	Fourier Transform Infrared
FWHM	Full Width at Half Maximum
f	Frequency
HR-TEM	High-resolution TEM
d_A	Individual Drug Dose A
IR	Infrared Spectroscopy
ILP	Intrinsic Loss Power
kcs	Kilo Counts Per Second
LRT	Linear Response Theory
LB	Liposome
H	Magnetic Field
MFH	Magnetic Fluid Hyperthermia
MHT	Magnetic Hyperthermia Therapy
MNPs	Magnetic Nanoparticles
M_r	Magnetic Remanence

K	Magnetocrystalline Anisotropy
ML	Magnetoliposome
T_m	Mean Transition Temperature
M	Mortality
MLV	Multilamellar vesicles
d_{RX}	Nanoparticle Diameter (From RX)
d_{TEM}	Nanoparticle Diameter (From TEM)
τ_N	Néel relaxation
OA	Oleic Acid
OPDA	Ortho Phenil Diamine
PDI	Poli dispersity Index
PID	Proportional-Integral-Derivative
KSCN	Potassium Thiocyanate
PB	Presto Blue
RT	Radiation Therapy
ROS	Reactive oxygen species
τ	Relaxation time
RPE	Reverse Phase Evaporation
M_S	Saturation Magnetization
SEM	Scanning Electron Microscopy
SiO_2	Silicon Dioxide
$LSiO_2$	Silicosomes
S_{AB}	Simultaneous Surviving Fraction
SC	Sodium Citrate
C_p	Specific Heat Capacity
SLP	Specific Loss Power
H_{stab}	Stabilized Field Amplitude
SQUID	Superconducting Quantum Interference Device
χ_{SP}	Superparamagnetic Susceptibility
S	Surviving Fraction
LN	**Synthetic Magnetosome**
T_t	Target Temperature
T	Temperature
TGA	Thermogravimetric Analysis
TEM	Transmission Electron Microscopy
t_T	Treatment Time
TB	Trypan Blue Exclusion Assay
VSM	Vibrating Sample Magnetometer
UV-Vis	Visible-Ultraviolet
WHH	Wave Half Height
RX	X-Ray Diffraction
XPS	X-Ray Photoelectron Spectroscopy

Abstract

One of the most complex challenges in cancer treatment is the ability of tumor cells to develop resistance to therapies, which means that, after a while, treatments may no longer be effective in controlling tumor growth. This situation is particularly critical in pancreatic cancer patients, where cancer cells are able to repair the damage caused by chemotherapy in a matter of days, requiring more intensive treatments, increased doses, and combination therapies, triggering an increase in adverse effects. For this reason, alternative treatments are of great interest. Novel active delivery systems based on remote and non-invasive magnetic stimuli hold the promise of therapeutic advances in nanomedicine. Magnetoliposomes and magnetosomes offer some attractive advantages, e.g., high loading capacities, shielding capabilities, as well as having lipid formulations already approved for clinics. Additionally, targeted delivery allows to increase the solubility of the drugs used, as well as to extend their use to drugs with pharmacokinetics not suitable for clinical use. This doctoral thesis focused on developing an innovative nanomaterial, called "synthetic magnetosome", for a dual, localized and "on-demand" therapy, combining chemotherapy and magnetic hyperthermia. The main objective was to find an integrated nanosystem capable of simultaneously delivering these treatments, looking for possible synergistic effects. This process covered from the synthesis of magnetic nanoparticles with high heating power, the fabrication of synthetic magnetosomes with optimized magnetic response and drug loading capacity, to their application in *in vitro* assays.

Synthetic magnetosomes were fabricated by the reverse phase evaporation method, consisting of an organic phase and an aqueous phase. The first phase consisted of an organic solution of thermosensitive, non-fusible, charged and pegylated lipids. On the other hand, the aqueous phase composed of hydrophilic magnetic nanoparticles with surface charge, optimized for energy absorption in an alternating magnetic field in high viscosity media, was used for the fabrication of magnetosomes loaded with the cytopharmaceutical cisplatin. Transmission electron microscopy imaging study shows that the synthetic magnetosomes present curved chains of magnetic nanoparticles covered by a lipid bilayer. In this arrangement, magnetic interactions of magnetic nanoparticles provide an enhanced magnetic response relative to magnetic heating of random nanoparticles. Mapping of the specific absorption rate distribution in the presence of an alternating magnetic field revealed a strong dependence on frequency in both systems, and an energy absorption value up to three times higher for magnetosomes compared to particles. These values did not change, in the case of magnetosomes, when the system was internalized by the cell, but tripled in the case of nanoparticles.

The synergistic effects of the dual and simultaneous therapy of the synthetic magnetosome were confirmed by *in vitro* assays in the PAN02 cell line, indicating that at a lower dose a greater effect is obtained than the separate chemotherapy and magnetic hyperthermia treatments. Also, the use of liposomes as a coating for the magnetic nanoparticles and as a vehicle for the cisplatin increased the concentration of the systems inside the cell. Studying the *in vitro* experiments results, we have developed a proposal to unify the dose-effect relationship of different thermal therapies in a universal function, simplifying in a single equation the effect of different mechanisms and distinguishing the sensitivity to diverse treatments in the same cell line.

Keywords: synthetic magnetosome, magnetic hyperthermia, dipolar interaction, cisplatin, liposome, synergy.

Resumen

Uno de los desafíos más complejos en el tratamiento del cáncer es la capacidad de las células tumorales para desarrollar resistencia a las terapias, lo que significa que, después de un tiempo, los tratamientos pueden dejar de ser eficaces para controlar el crecimiento tumoral. Esta situación es particularmente crítica en pacientes con cáncer de páncreas, donde las células cancerosas son capaces de reparar el daño causado por la quimioterapia en cuestión de días, requiriendo tratamientos más intensivos, aumento de dosis y terapias combinadas, desencadenando un incremento de los efectos adversos. Por este motivo, los tratamientos alternativos cobran gran interés. Los novedosos sistemas de liberación activa basados en estímulos magnéticos remotos y no invasivos son una promesa de avances terapéuticos en nanomedicina. Los magnetoliposomas y los magnetosomas ofrecen algunas ventajas atractivas, por ejemplo, grandes capacidades de carga, mimetización con el entorno, además de contar con formulaciones lipídicas ya aprobadas para las clínicas. Adicionalmente, la administración dirigida permite elevar la solubilidad de los medicamentos utilizados, como también ampliar al uso a medicamentos con farmacocinética no adecuada para uso clínico. Esta tesis doctoral se enfocó en desarrollar un nanomaterial innovador, denominado "*magnetosoma sintético*", para una terapia dual, localizada y "a demanda", que combina la quimioterapia e hipertermia magnética. El objetivo principal fue encontrar un nanosistema integrado capaz de administrar simultáneamente estos tratamientos, buscando posibles efectos sinérgicos. Este proceso abarcó, desde la síntesis de nanopartículas magnéticas con alta potencia de calentamiento, la fabricación de los magnetosomas sintéticos con respuesta magnética y capacidad de carga de medicamento optimizada, hasta su aplicación en ensayos *in vitro*.

Los magnetosomas sintéticos se fabricaron por el método de evaporación de fase reversa, compuesta por una fase orgánica y una fase acuosa. La primera, formada por una solución orgánica de lípidos termosensibles, no fusionables, cargados y pegilados. Por su parte, la fase acuosa compuesta de nanopartículas magnéticas hidrofílicas con carga superficial, optimizadas para la absorción de energía ante un campo magnético alterno en medios de alta viscosidad, fue utilizada para la fabricación de los magnetosomas cargados con el citofármaco cisplatino. El estudio mediante imágenes de microscopía electrónica de transmisión mostró que los magnetosomas sintéticos presentan cadenas curvas de nanopartículas magnéticas cubiertas por una bicapa lipídica. En esta disposición, las interacciones magnéticas de nanopartículas magnéticas proporcionan una respuesta magnética mejorada en relación al calentamiento magnético de las nanopartículas no organizadas. El mapeo de la distribución de la tasa de absorción especifica en presencia de un campo magnético alterno reveló una fuerte dependencia con la frecuencia en ambos sistemas, y un valor de absorción de energía de hasta tres veces mayor para los magnetosomas en comparación con las partículas. Estos valores no se modificaron, en el caso de los magnetosomas, cuando el sistema fue internalizado por la célula, pero se triplico para el caso de las nanopartículas.

Los efectos sinérgicos, en la terapia dual y simultánea del magnetosoma sintético se confirmaron por ensayos *in vitro* en la línea celular PAN02, indicando que a una menor dosis se obtiene un mayor efecto que los tratamientos de quimioterapia e hipertermia magnética por separado. Así también, el uso de liposomas como recubrimiento de las nanopartículas magnéticas, y como vehiculización del cisplatino incrementó la concentración de los sistemas en el interior celular. Mediante el estudio de los resultados de experimentos *in vitro* hemos desarrollado una propuesta para unificar la relación dosis-efecto de las diferentes terapias térmicas en una función universal, simplificando en una única ecuación el efecto de los diferentes mecanismos y logrando diferenciar la sensibilidad a los distintos tratamientos en una misma línea celular.

Palabras clave: Magnetosoma sintético, hipertermia magnética, interacción dipolar, cisplatino, liposoma, sinergia.

Preface

As a physicist, my driving force behind the research presented in this thesis has been the exploration of biomedical and clinical applications of nanomaterials. It is a well-acknowledged fact that nanoscience is an interdisciplinary field focused on the fabrication and manipulation of nanomaterials. However, when talking about nanomedicine it becomes suddenly clear that there is an inherent multidisciplinary in the way it incorporates nanomaterials into a field that, until recently, seemed quite distant. The *very* complex interactions between materials and biological systems, have been a persistent motivation behind the undertaking of this thesis.

The beginnings of my PhD research are related to the nanoHeat project, being developed some years ago among the MAGNA group of Universidad de Zaragoza, which I joined, the Departamento de Bioquímica y Biología Molecular e Inmunología at the Universidad de Granada, and nB NanoScale Biomagnetics, in the framework of a RETOS national call funded by the Science Ministry of Spain. The objective of the project was the "development and preclinical validation of the nanoHeat system," that is, to develop a new type of nanovector against cancer cells that could provide a synergistic effect of magnetic hyperthermia and chemotherapy, triggered by magnetic fields. The project included the *in vitro* and *in vivo* assessment (by both Zaragoza and Granada University Teams) of the efficacy of this new nanosystem.

This project, which involved the development of this nanosystem in colloidal form, at scales suitable for future commercialization, included extensive research on the conditions necessary for working with volumes compatible with commercial production. This meant scaling up from the typical laboratory volumes of $1\ mL$ in the manufacturing of nanovector to producing $80\ mL$ required for all planned systematic *in vivo* experiments. Such an increase in scale naturally posed significant challenges in terms of maintaining sterile conditions, ensuring reproducibility, and adapting protocols for large-scale production. This part of the work has not been detailed in this doctoral thesis due to it being considered part of the behind-the-scenes aspects of the research presented. However, I believe it is a very important part because of what it signifies in terms of the current challenges in many fields of nanotechnology, bridging the gap between the laboratory and industry. Therefore, thanks to this interdisciplinary collaboration, I had the unique opportunity to actively participate and contribute to the whole process from the design and synthesis of the nanovector, up to the *in vivo* trials, working with colleagues specialized in biology and immunology (mainly with my laboratory partner MSc. Carmen Jiménez at the Immunology group of Dr. I Molina, UG), gaining an invaluable experience for my future work.

As part of another behind-the-scenes aspect of this work, which has not been fully completed and therefore is not included in this thesis, I must mention that one of the initial objectives was to design and develop a device for studying and measuring the release kinetics of the drug and chemotherapy agent (cisPt) encapsulated in the nanovector, called synthetic magnetosomes. This device, which I effectively designed and constructed during my thesis work, allows for the real-time measurement of drug release profiles using spectrophotometry, under conditions of applied magnetic field release. However, the final part, which would involve a systematic and detailed study of the release profiles of the synthesized magnetosomes, required a time investment that exceeded the available for this thesis. This is the reason why, although extremely interesting, we have not delved into the nature of magnetosomes as nanocarriers of chemotherapeutic drugs or their detailed release profile under magnetic fields.

What this Thesis *do* report and discuss is the complete process from the synthesis and characterization of the novel system for simultaneous chemotherapy and magnetic hyperthermia treatment, to the confirmation of its efficacy and potential for dual therapies. The manufacturing process of a dual nanocarrier for drug and magnetic particles is detailed, from the synthesis of optimized magnetic particles as nanoheaters, drug encapsulation and its final application in *in vitro* experiments to study the synergistic effects in treatment. The thesis is organized as follows:

- Chapter 1 provides an introduction with basic concepts of nanomedicine, chemotherapy, liposomes, magnetic hyperthermia, and outlines the main objectives of the thesis.

- Chapter 2 describes all the steps and experimental methods along the synthesis and characterization of the synthetic magnetosomes, highlighting those details within experimental protocols that could serve as a guide for other researchers and students.

- Chapter 3 presents results from the physicochemical characterization of synthetic magnetosomes, including constituent magnetic nanoparticles, lipid compound characterization, lipid membrane features and the interaction among these components.

- In Chapter 4, the focus is on the magnetic properties of synthetic magnetosomes, detailing the unique magnetic behavior found in magnetosomes, and their remarkable response to alternating fields for magnetic hyperthermia, covering also *in vitro* performance.

- Finally, Chapter 5 details *in vitro* assays of toxicity, internalization tests, and primarily explores the combined effects of magnetic hyperthermia and chemotherapy with cisplatin. The concept of thermal dose is introduced, discussing synergistic effects observed when applying these two therapies simultaneously using a single nano-platform comprising synthetic magnetosomes.

CHAPTER 1

Introduction

"…Aunque me fuercen yo nunca voy a decir,

que todo tiempo por pasado fue mejor.

Mañana es mejor…"

L. A. Spinetta

1.1.Motivation

According to the World Health Organization, cancer can be defined as the rapid generation of abnormal cells that exceed their usual boundaries, invading adjacent body parts and spreading to other organs [1]. The Global Cancer Conservatory's 2020 statistics reveal that deaths due to the metastasis of malignant tumors rank first or second among causes of death for individuals aged 30 to 70 (Figure 1.1) [2] in 112 out of 183 evaluated countries [3]. This places cancer as the second leading cause of death for individuals over 80, following cardiovascular diseases.

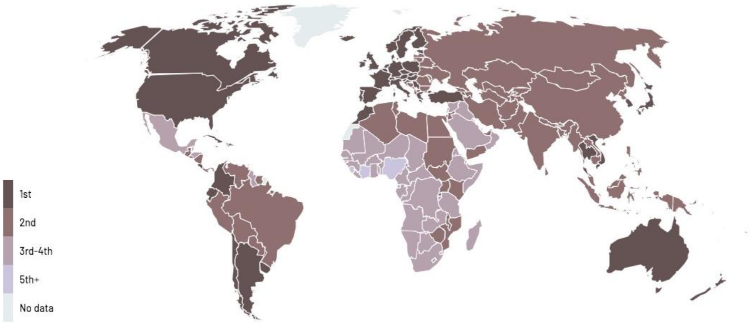

Figure 1.1. Cancer ranks as leading cause of death at ages x, [30< x <70] in 2018. Data source: Cancer atlas, Global Cancer Conservatory - World Health Organization.

The primary strategies for addressing cancer include detection, diagnosis, and treatment. Medical professionals emphasize the crucial role of prevention and early detection in the fight against oncological diseases. The specific diagnosis and treatment depend on the type of cancer. Systemic treatments, such as chemotherapy (CT), are prescribed for blood tumors affecting the entire body. In contrast, local treatments like radiation therapy (RT) and surgery are common procedures for solid tumors. The primary objective of treatments is to eliminate the tumor while causing minimal damage to surrounding healthy tissues. In recent years, the combined administration of therapies has gained prominence to reduce the dose and, consequently, the adverse effects of each treatment. As a result, emerging and alternative therapies are becoming promising treatment options.

Nanotechnology involves the study, production, and manipulation of systems where at least one dimension is less than 100 nm. The nanometric scale enables increased interaction with biological entities of similar sizes, such as cells, viruses, and organelles, sparking significant interest in the medical and pharmaceutical communities. Advances in drug release, diagnosis, and surgery have been achieved through nanotechnology [4]. A multidisciplinary collaboration of physicists, chemists, biotechnologists, mathematicians, and various specialists contributes to the progress, interaction, and application of this rapidly evolving field of science.

Nanomaterials, owing to their small size relative to cells yet sufficient to encapsulate or adsorb lipid and water-soluble components, along with a large surface-to-volume ratio, functionalization capabilities, and the ability to interact with matter, absorb and re-emit energy, possess properties that make them valuable in the prevention, detection, diagnosis, and treatment of oncological diseases(Figure 1.2) [1, 4] [5]. The increasing interest in oncology has led to the development of numerous new nanomaterials and improvements to existing ones. While many are still in the laboratory or preclinical phases, some have gained approval and are already in clinical use; Table 1.1 summarizes some of these materials [6] [7]. Currently, there is no definitive consensus on the risks associated with nanomaterials. Their evaluation poses a challenge due to a lack of evidence, the complexity, and the vastness of nanomaterials without established frameworks for evaluating their hazards.

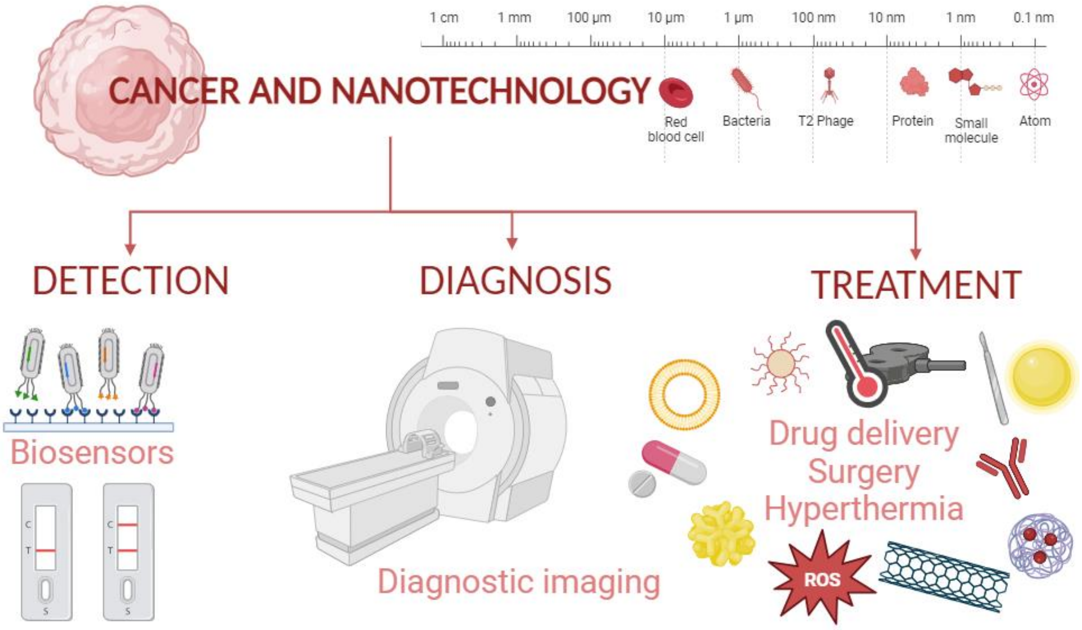

Figure 1.2. Scheme of the advances of nanoscience for the development in detection, diagnosis, and treatment in cancer disease.

Of the 43 nanoparticle-based therapeutic compounds that have received approval from the Food and Drug Administration or the European Medicines Agency, a notable majority, 23 formulations, utilize lipid-based nanoparticles. This prevalence shows the versatility and effectiveness of lipid-based systems in drug delivery and therapeutic applications, but also is a clear evidence of the safety and efficacy that nanotechnology can achieve using a diversity of nanomaterials. The clinically approved applications based on nanoparticle-containing formulations include for treating neoplasms (13 lipid-based formulations approved), carrying chemotherapeutic agents directly to tumor cells and minimizing damage to healthy tissues. Other applications are found for anesthesia (2), macular degeneration (2), and various infections (2) [8] [9]. A specific remark deserves the success of nanoparticle-based platforms in vaccine development, particularly highlighted during the COVID-19 pandemic with lipid nanoparticles successfully implemented in clinical settings for the delivery of mRNA, by shielding the mRNA from degradation while facilitating its uptake into cells and subsequent release. [10]

Table 1.1. Nanotechnology approved treatments. Data source: [6, 7] [11] [12].

Approval date	Product	Company	Nanoparticle	Drug	Indicated
1995-1999-2003	Doxil	Johnson and Jonhson	Liposome	Doxorubicin	Kaposi´s sarcoma, ovarian and breast cancer
1996	DaunnnoXome	Galen	Liposome	Daunorubicin	Kaposi`s sarcoma
1999	DepoCyt	Pacira	Liposome	Cytarabine	Neoplastic meningitis
2002	Ferucarbotran	Resovist/Ciavist	IONs	-	MRI contrast
2005	Abraxane	Abraxis/Celgene	Nanoparticle-bound albumin	Plaxitaxel	Breast cancer, pancreatic cancer, non-small cell lung cancer
2006	Oncaspar	Enzon-sigma-tau	Polym protein conjugate	L-asparginase	Leukemia
2009	Ferumoxytol	Feraheme/Rienso	IONs	-	Iron deficiency treatment and MRI contrast
2010	Lipoplatin	Regulon	Liposome	Cisplatin	non-small cell lung cancer
2010	NanoTherm	Magforce Nanotechnologies	IONs	-	Glioblastoma
2012	Marqibo	Talon	Liposome	Vincristine	Acute lymphoid leukemia
2015	Onivyde	Merrimack Pharma	Liposome	Irinotecan	Pancreatic cancer
2017	Vyxeos	Celator/Jazz Pharma	Liposome	Cytarabine/Daunorubicin	Acute myeloid leukemia

Liposomes are artificial bilayer vesicles (Figure 1.3), primarily composed of phospholipids. These phospholipids are amphiphilic molecules characterized by a hydrophilic group head and a hydrophobic tail (Figure 1.3 a), leading to the spontaneous formation of micelles in the presence of an aqueous solution (Figure 1.3 b). In micelles the hydrophobic tails point to the center of the structures, creating a hydrophobic interior called lumen. In contrast, in liposomes, the phospholipids are arranged in bilayer structures, forming a hydrophilic lumen (Figure 1.3 c). Liposomes can be formed by a single bilayer (Figure 1.3 d) or by a set of bilayers, known as multilamellar vesicles (Figure 1.3 e).

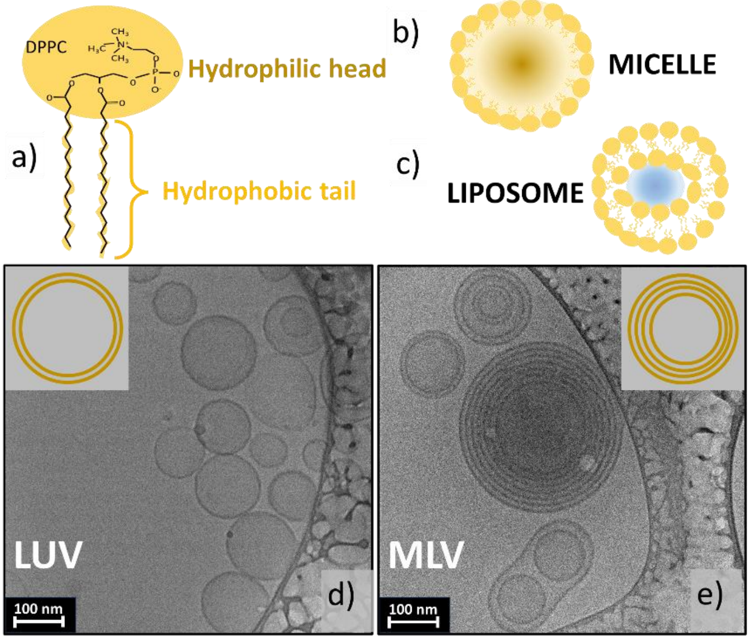

Figure 1.3. Structural components and arrangements of DPPC (1,2-dipalmitoyl-sn-glycero-3-phosphocholine) phospholipids: a) detailed diagram illustrating the molecular structure of DPPC, a common phospholipid. b) Schematic representation showing the arrangement of lipids in a micelle formation. c) Diagram depicting the lipid organization within a liposome. d) Cryo-TEM image capturing (d) a large unilamellar vesicle (LUV), showcasing its singular lipid bilayer structure; (e) a large multilamellar vesicle (MLV), highlighting its multiple concentric lipid bilayers

Since the discovery of liposomes in 1965 by Bangham et al. [13], food, cosmetics and pharmaceutical industries have shown great interest in investing to take advantage of it. The advances in lipid formulations have been achieved by focusing on completing and improving the requirements:

1) encapsulating a relevant therapeutic drug load,

2) prolonging drug circulation while avoiding mononuclear phagocytic system,

3) accumulating in the target tissue,

4) releasing the loaded drug.

These advancements in liposome technology have evolved steadily, and they can be considered today as concomitant with many applications in various industries. In pharmaceuticals, they have led to more effective and safer drug delivery systems. In cosmetics, they improve the delivery and efficacy of active ingredients. In the food industry, liposomes encapsulate additives and nutrients, ensuring stability of these molecules.

Liposomes are typically categorized into various general families based on the size of the vesicles and the number of bilayers, as detailed in Table 1.2. Another classification method relates to their structure, which considers the critical packing parameter, categorizing them into structures such as bilayer vesicles, lamellar phases, and others [14] [15]. Regarding their composition, liposomes can be classified into groups like conventional, cationic, long-circulating, fusogenic, immunoliposomes, and stimuli-responsive types.

Table 1.2. Classification of liposomes according to size and number of bilipid membranes. From Ref [16] .

FAMILY	SIZE (nm)	NUMBER OF LIPIDIC BILAYER
Small unilamellar vesicles	20-100	1
Large unilamellar vesicles	>100	1
Giant unilamellar vesicles	10000	1
Oligolamellar vesicles	100-1000	>1
Large multilamellar vesicles	>500	>1
Multivesicular vesicles	>1000	>1
Small unilamellar vesicles	20-100	1

Within the liposome-based formulations, stimulus-responsive liposomes are relevant due to their ability to execute localized chemotherapy with on-demand release triggered by specific stimuli. These stimuli can include variations in pH, temperature increases, enzyme concentration, redox potential, among others. In 1978, Yatvin et al.[17] were pioneers in suggesting the use of liposomes with slightly elevated transition temperatures relative to body temperature for drug release. Thermosensitive liposomes release encapsulated drugs at elevated temperatures (39-45°C), a condition known as hyperthermia. To achieve precise control over drug release, a combination of phospholipids, lysolipids, and synthetic polymers is employed in the preparation of thermosensitive liposomes.[18]

As highlighted in Table 1.1, formulations involving ***magnetic nanoparticles (MNPs)*** are extensively studied and clinically or preclinically evaluated. These MNPs find application as contrast agents in magnetic resonance imaging, for magnetic hyperthermia, immunotherapy, drug delivery, and combatting microbial biofilms [11]. The market for MNPs applied in medicine is anticipated to reach a value of US$5.5 billion by 2024 [19]. One particularly intriguing branch is the encapsulation of MNPs within liposomes, creating ***magnetoliposomes (ML)***. In 1996, the Kobayashi T. group reported one of the pioneering studies on the use of ML to achieve temperature increases up to 43°C in cell culture and a solid matrix [20]. Two years later, employing the same ML, they achieved complete tumor regression after 30 days in rats from the F344 line [21]. In 2001, they further functionalized ML with G250 antibody fragments, enhancing particle concentration in tumors for *in vivo* and *in vitro* experiments, thus improving results in hyperthermia therapy for carcinomas [22]. Over the years, this group and others have continued to make substantial progress in the use of ML for thermal therapy [23] [24] [25].

1.2. Hyperthermia

The aberrant growth of neoplastic cells distinguishes them from their normal ones, creating opportunities for targeted therapeutic interventions. Tumor cells, capable of thriving in hypoxic environments, display heightened sensitivity to temperature changes, particularly during the S phase of the cell cycle, under low pH conditions, in hypoxic environments, and when nutrient deficient. Understanding these differences provides a basis for optimizing neoplastic therapies. According to the National Institutes of Health, hyperthermic therapy involves a controlled increase in body temperature ($37°C$) for enhanced efficacy in cancer treatment. Thermal therapy protocols categorize temperatures into *diathermy* ($T < 41°C$), *hyperthermia* ($41 < T < 46°C$), and *thermal ablation* ($T > 46°C$), with the selection of the method based on the targeted tissue and treatment area.

For over 5000 years, hyperthermia has been considered potential as a therapeutic modality treatment for various diseases by different cultures. The first recognized documentation was the Egyptian papyrus from the 5th century BC, where a breast cancer tumor was exposed to "natural fever" before to surgical removal. In 1866, German surgeon Carl Busch documented tumor regression in a patient following a feverish infection after the removal of a facial sarcoma, sparking significant interest in the scientific community. The interest generated by early observations led to substantial progress in comprehending the effects of hyperthermia on cellular structures and functions. *In vitro* experiments have confirmed that temperature elevation induces alterations in cell membrane and cytoskeleton structures, modifies membrane fluidity and stability, leads to denaturation and aggregation of proteins, induces changes in DNA structure blocking repair and synthesis, and disrupts cellular metabolism.

In most cancer therapies the oncologist prescribes the dosage and the number of sessions based on each individual patient's specific needs. Subsequently, medical physicists undertake the responsibility of preparing the treatment plan to administer the prescribed dose to the target tissue while minimizing damage to healthy tissue. With the growing prominence of hyperthermia as a cancer therapy and its increasing role in clinical practice, it becomes imperative to establish standardized terminology in this multidisciplinary technique. This leads to the necessity of defining a thermal dose, and the model presented by Sapareto and Dewey in 1984 [26] is widely accepted within the scientific community. Sapareto and Dewey defined the thermal dose as cumulative equivalent minutes at 43°C (t_{CEM43}),

$$t_{CEM43} = t\,R^{(43-T)} \qquad 1.1$$

where t is the exposure time (in minutes), and T is the actual temperature (in degrees Celsius). The parameter R is a constant for a given cell line, often taken as 0,5 for $T > 43\ °C$ and 0,25 for $T < 43\ °C$. At the time, 43°C was chosen as an arbitrary temperature, later associated with protein denaturation. The significance of this isotherm lies in its ability to offer continuous monitoring and control of the dose within the tumor by regulating both temperature and time parameters. Furthermore, the same authors highlight the impact of thermotolerance in neoplasms. Therefore, in subsequent years, they proposed a correction to their calculations by introducing the thermotolerance dose ratio, especially for cases involving multiple doses [27].

The primary goal of thermal therapy is to achieve and sustain a uniform treatment temperature in the targeted area, while preserving the integrity of surrounding healthy tissue. Hyperthermia can be applied *locally,* focusing on the tumor and its surrounding tissue; *regionally,* treating an entire organ or limb, or *whole-body* hyperthermia. Whole-body hyperthermia techniques include water or wax baths, thermal suits, thermal blankets, and blood perfusion. These methods aim to elevate the body's temperature uniformly. In regional treatments, protective materials with low thermal conductivity are employed to shield healthy tissue, or regional perfusions are conducted to manage temperature distribution. Several thermal therapy approaches involve the use of electromagnetic waves (Figure 1.4), with their interaction being intricate and potentially damaging to tissues. The penetration of these waves through the skin is dependent on factors such as wavelength and the nature of the radiation, whether ionizing or non-ionizing. Visible light ($\lambda \approx 350 - 700\ nm$) and near-infrared ($\lambda \approx 800 - 1000\ nm$) (Figure 1.4) are commonly employed for regional treatments, with limited tissue penetration of up to ~$3\ cm$ in soft tissue. To enhance these technique, various types of nanoparticles, such as gold nanoparticles acting as photothermal conductive agents, have been used [16].

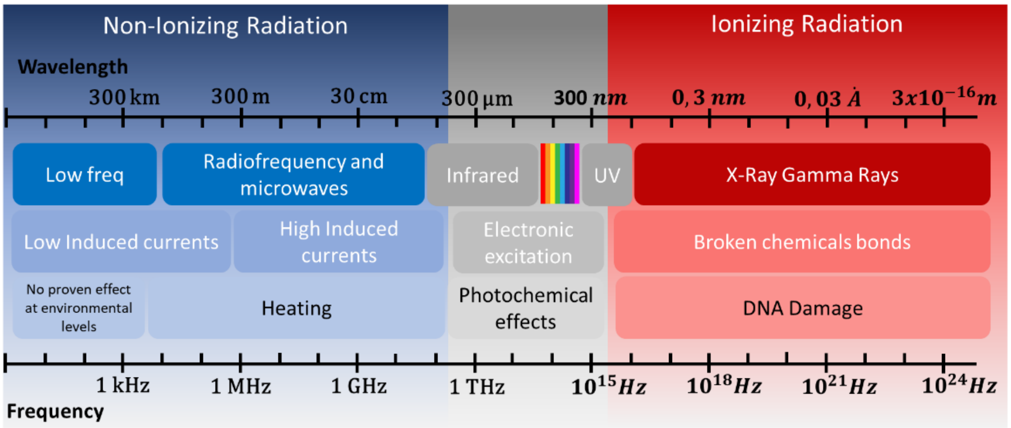

Figure 1.4. Electromagnetic spectrum divided in ionizing and no-ionizing radiation. Wavelength and frequency guides. Biological effect produced by each range.

In current clinical practice, various devices are employed for thermal ablation within tumors ($T > 50°C$). Radiofrequency ablation utilizes a radiofrequency electric current (350-500 kHz) (Figure 1.4) applied to the target area through a needle. Microwave ablation employs applicators transmitting high-frequency electromagnetic waves (900-2450 MHz) (Figure 1.4) to raise the temperature in solid tumors. Despite the minimally invasive nature of these clinical techniques, a key limitation is their restricted tissue penetration, resulting in energy deposition in the surrounding healthy tissue. Nevertheless, Magnetic Fluid Hyperthermia stands out as a promising and attractive strategy. This approach is minimally invasive, offers greater treatment depth, is externally controlled, and highly localized.

1.2.1. Magnetic fluid hyperthermia

When exposing MNPs to an alternating magnetic field (AMF), an increase in temperature can occur due to hysteresis losses and/or magnetic relaxations mechanism resulting from the alignment of magnetic moments with the external field. All these mechanisms act independently, but depending on the magnetic configuration of the MNPs, one of them typically dominates the behavior. The idea of using magnetic colloids as therapeutic heating sources against cancer through inductive heating can be traced back to 1957, when Gilchrist et al.[28] used maghemite (Fe_2O_3) with sizes ranging from 0,02 to 0,1 µm to produce a magnetic colloid and injected into canine lymph nodes to increase temperature 14°C in three minutes(H_0≈120-250 Oe, f= 1.2 MHz).

In the early 2000s, the advancements in the synthesis of nanomaterials made possible to produce suitable magnetic colloids containing iron-oxide MNPs, and their use under low-frequency (100 kHz) magnetic fields for deep tissue heating was reported by Jordan et al. [29] This treatment, known as Magnetic Fluid Hyperthermia (MFH), was based on the combination of a clinically approved magnetic fluid NanoTherm®, consisting in MNPs of 15 nm at a concentration of 112 mg/mL, and the first whole-body magnetic field applicator for MFH treatment operating at $f = 100\ kHz$ with a variable field in the range of 0-15 kA/m. Today, several research groups are focused on studying and applying MFH, and several companies are dedicated to manufacturing field applicators [30] [31] [32]. Although still in clinical stages (Phase I and II), MFH thermal therapy, first applied in humans for prostate carcinoma in 2005, shows promising results both as a standalone treatment and in combination with RT and CT [33]. Table 1.3 summarizes the advances in clinical trials of MFH therapy.

Table 1.3. Clinical trials of thermal therapy by MFH using NanoTherm®. Information of the ref. [33].

Cancer type	Trial Phase	Number of patients	Combined treatment	T_{MAX} (°C)	Year
Prostate carcinoma	I	1	-	48.5	2005
Chondrosarcoma, carcinoma, (cervical, prostate, ovarian, rectal) carcinoma	I	22	RT/CT	39.5	2006
Glioblastoma carcinoma	I	14	RT/CT	44.6	2006
Prostate carcinoma	I	10	-	42.7	2007
Prostate carcinoma	II	10	-	55	2007
Glioblastoma multiforme	II	3	RT/CT	65.6	2009
Glioblastoma multiforme	II	66	RT/CT	82	2011

During MFH, MNPs convert magnetic energy into thermal energy, releasing heat into the medium. The specific loss power (SLP) is the parameter used to quantify power losses (P) of MNPs per unit of mass[1] (m_{MNPS}) in response to an AMF of frequency f and field H,

$$SLP = \frac{P}{m_{MNPS}} \tag{1.2}$$

Also referred to as specific absorption rate (SAR) and specific power absorption (SPA), with units of $\left[\frac{W}{kg}\right]$. The SLP value depends on the MNPs characteristics, such as its size and crystalline order, the state of the sample and the applied H and f.

For a given magnetic fluid, the SLP can be increased by applying larger frequencies and/or applied fields. However, and in addition to technical constraints due to the increasing power required to achieve such conditions, there are also patient-related issues. In the ‘80s, Brezovich conducted experiments to determine the limit of the product $H \times f$ that a patient can tolerate, reporting a maximum value of $4{,}85 \cdot 10^8$ A/(m·s) using a 30 cm coil in a treatment lasting over an

---

[1] The unit of mass can refer to the complete solution, the solid part in suspension or the magnetic material. This should be clarified in the report. In our case we consider the mass of MNPs.

hour [34]. Beyond this limit, the patient experiences discomfort due to the rise in temperature in healthy tissue caused by eddy currents. Nevertheless, if a smaller coil diameter is used, this limit can be exceeded, and thus, it is not always necessary to adhere strictly to these restrictions. For a better understanding of the MFH phenomenon we need to introduce concepts and characteristics of MNPs, which is offered in the next section. A more complete explanation about the basics of power absorption by MNPs is offered in Chapter 4.

1.3.Structural and magnetic properties of ferrite

The general chemical formula for ferrites spinel structure is represented as MFe_2O_4, where M is a divalent metal ion. The first permanent magnetic material discovered was magnetite, which is essentially an iron ferrite ($FeFe_2O_4$). In commonly studied and utilized ferrites, M is typically a transition metal such as Mn, Fe, Co, or Zn, and they were often employed in magnetic memory applications. The spinel structure comprises an FCC arrangement of 56 atoms: 32 oxygen atoms and 24 metal cations. Within this structure, 8 cations occupy the tetrahedral site (A), and 16 occupy the octahedral site (B) [35]. The general formula is expressed as:

$$[M_{(1-i)}Fe_i]^A[M_iFe_{(2-i)}]^B O_4 \tag{1.3}$$

where i is known as the inversion parameter. Depending on the metal cation distribution, the spinel structure can be normal ($i = 0$), inverted ($i = 1$), or partially inverted ($0 < i < 1$). Given its complexity, the structure is often depicted by dividing the unit cell into 8 cubes, in Figure 1.5, the scheme was simplified by omitting some ions, representing a case of inverted spinel [36]. In a normal spinel structure, site A is filled with 8 divalent cations, and site B is filled with 16 trivalent metal cations. In an inverted spinel structure, the 8 divalent metals are in the octahedral position, while the 16 trivalent metals are divided between sites A and B, Figure 1.6 a show magnetite structure. Individual cations Interact indirectly through antiferromagnetic interactions via oxygen anions, known as superexchange interactions [37].

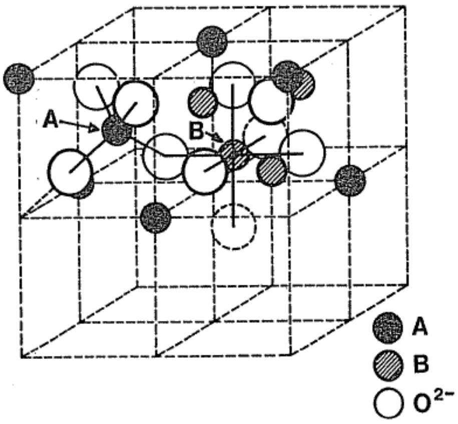

Figure 1.5. Arrangements of ions, showing tetrahedral (A site) and octahedral (B site) coordinated sites. Figure taken from McCurrie [36].

$ZnFe_2O_4$ is known as a normal spinel, while Fe_3O_4 is an inverted spinel. The distinction between normal and inverted is not rigid, and there are cases where ions from the same material can be found in both sites A and B. The occupation depends on factors such as composition, preparation method, and treatment temperature.

One way to tune the magnetic properties of magnetite is to modify the antiferromagnetic interactions between sites A and B. In the normal ferrite $ZnFe_2O_4$, the non-magnetic divalent cations Zn^{2+} preferentially choose the tetrahedral site, resulting in a dipolar moment of 0, and the material behaves as a paramagnet. This suggests that the Fe^{3+} cations in the octahedral site are randomly oriented, showed in Figure 1.6 b. The magnetic moment of any inverted spinel ferrite increases with the addition of $ZnFe_2O_4$, reaching a maximum value of 50%. This phenomenon has been employed in numerous commercial applications, especially in mixtures of Mn-Zn, Ni-Zn, and Mg-Zn.

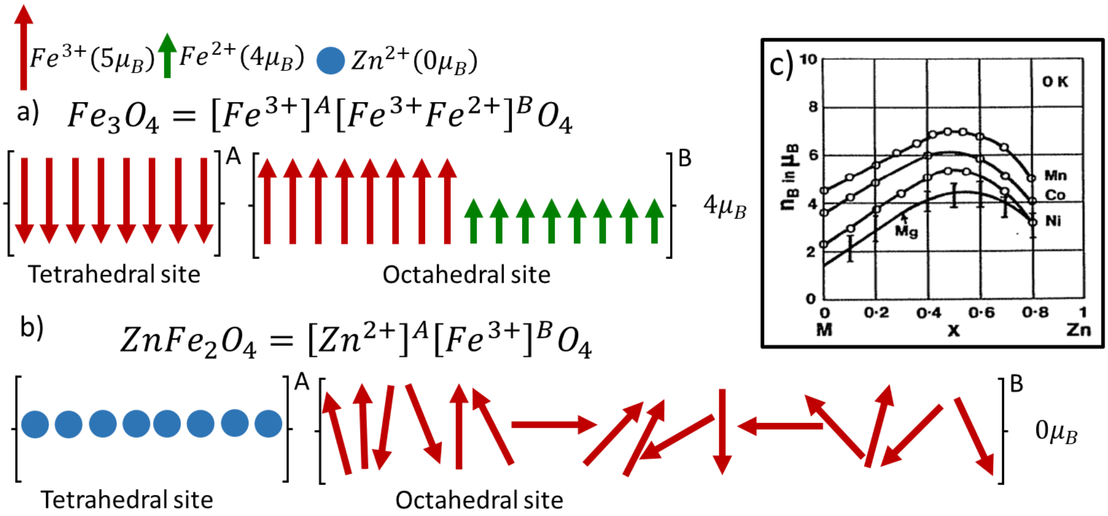

Figure 1.6. Magnetic structure of a) magnetite in the inverse spinel state, and b) zinc ferrite in normal spinel state. c) Saturation magnetization at 0K for various mixed ferrites, M=Mn, Co, Ni and Mg. From ref. [36].

In $Zn_xFe_{3-x}O_4$ (0<x<1), Zn^{2+} cations preferentially occupy the tetrahedral site, removing a spin that interacted antiferromagnetically with site B. This leads to an increase in the saturation magnetization of the material for low Zn substitutions. Theoretical studies report a partially inverted spinel structure in the Zn-doping of $Zn_xFe_{3-x}O_4$ [38]. A more in-depth interpretation of magnetic phenomena for MNPs continues in Chapter 4.

1.4. Magnetoliposomes

Magnetoliposomes (ML) are aliphatic nanocarriers composed of liposomes and MNPs. Since their description by pioneers Kiwada et al. in 1986 [39] and Cuyper and Joniau in 1988 [40], ML has been under study and development by various research groups. These nanocarriers find applications in drug delivery, magnetic hyperthermia, magnetic resonance image contrast agents, and even diverse applications such as cell sorting and gene delivery.

The morphological structure of ML depends on the desired application, determined by factors such as lipid composition, MNP size, and synthesis method. Depending on their size and coating, MNPs can be situated between the hydrophobic tails of phospholipids in the bilipidic membrane (Figure 1.7 a), within the hydrophilic core (lumen) (Figure 1.7 b), or adhered to the hydrophilic surface formed by the hydrophilic heads of the phospholipids (Figure 1.7 c). Garnier et al. [41], present representative images of a system of spherical vesicles with high or low efficiency in maghemite encapsulation in the lumen of LB (Figure 1.7 e). Bonnaud et al. [42]deformed the bilipidic membrane by encapsulating clusters of 60 nm formed by 6 nm superparamagnetic iron oxide nanoparticles (Figure 0.2b). On the other hand, Floris et al. presented a colloid with a high superparamagnetic iron oxide nanoparticles density located on the external surface of the vesicles [43] (Figure 1.7 f).

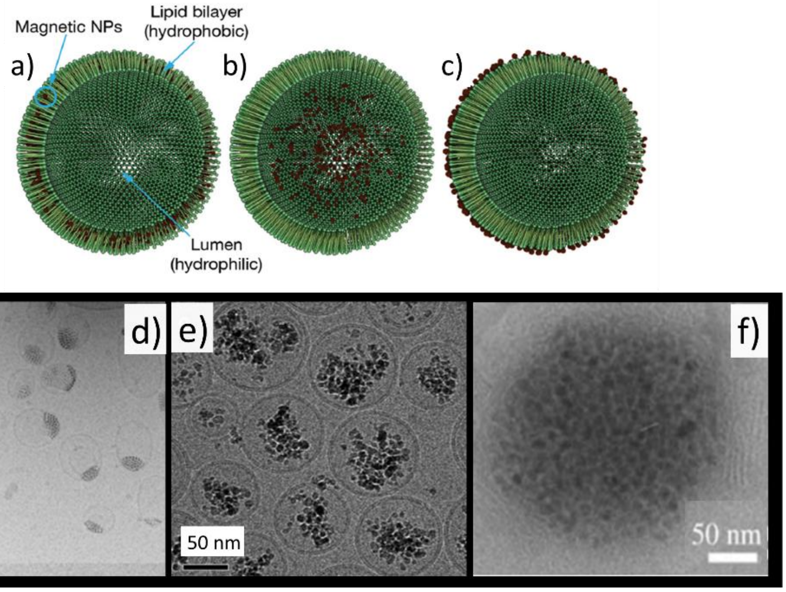

Figure 1.7. Schematic representation of magnetoliposomes. MNPs localized in the bilipidic membrane (a), in the hydrophilic core (lumen) (b) or attached to the surface (c) [44]. Magnetosomes found in literature. Cryo-TEM images of MNPs encapsulated in the bilayer d) [42], in the hydrophilic core e) [41] , and attached on the lipidic surface f) [43].

As nanocarriers, ML also offer the possibility of being accumulated through external magnetic fields. In 2006, Fortin-Ripoche et al. confirmed, through magnetic resonance images, that the accumulation of ML was 7-8 times greater when magnets were applied to prostate cancer in mice compared to when no field was applied [45].

Another notable advantage of ML is their capability to release the encapsulated drug in a controlled manner by applying an external alternate magnetic field. During the magnetic hyperthermia process, the increase in temperature produced by MNPs leads to the reversible phase transition of the lipid membrane. This enables a combined therapy approach involving hyperthermia and chemotherapy. Synergistic effects between thermal therapy and chemotherapy have been reported. [46] [47] [48]

1.5.The chemotherapy of Cisplatin

Chemotherapy (CT) is a systemic cancer treatment that utilizes one or more drugs to either kill or inhibit malignant cell growth. Its application aims to control tumor growth as neoadjuvant therapy or act as a palliative method. Being a systemic therapy, the administered drug disseminates throughout the body with the consequent undesired impact on healthy tissues, which constitutes one of its most significant adverse effects. In this thesis, we will focus our work on one of the most widely used cytotoxic agent, i.e., cis-diamminedichloroplatinum (II), commonly known as cis-platinum or cisplatin (cisPt).

CisPt is widely used to treat neoplasms of the head and neck, lungs, urinary tract, esophagus, breast, ovary, testicles, and brain [49]. This compound is poorly soluble in water and is typically administered intravenously. Its molecular structure consists of a central platinum atom linked to two amino groups and two chlorides arranged in the cis position (Figure 1.8). In its inert form, once administered, one or two chlorine atoms are displaced and replaced by water molecules due to the low intracellular concentration of chlorine, giving rise to the active compound (Figure 1.8). [50]

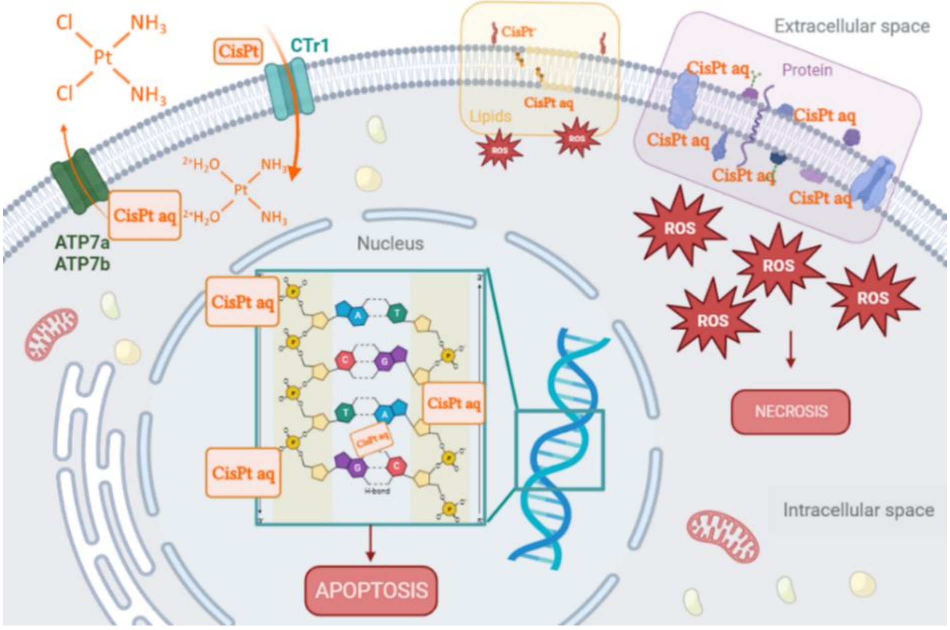

Figure 1.8. Representative scheme of internalization and efflux of cisPt with cell. CisPt molecule and it´s active formulation, hydrolyzed cisPt (cisPt aq). Main mechanisms of action, interaction with DNA, membrane proteins and phospholipids.

Given the low concentration of chlorine in the cell cytoplasm, cisPt enters the cell passively. Studies by Kuo et al. have demonstrated that cisPt utilizes copper transporters, CTr1, to traverse the cell membrane, and its excretion is regulated by the ATP7a and ATP 7b channels (Figure 1.8)[51].

The mechanism of cell death induced by cisPt is still not entirely clear; however, its primary mode of action involves the formation of mono, inter, and intra adducts between DNA and cisPt. This process inhibits cellular replication and transcription, thereby halting cellular proliferation and inducing apoptosis [52]. Hydrolyzed cisPt molecule have affinity with proteins, phospholipids and pyruvate groups present in the bases of adenine and guanine [53]. Due to its radical nature, the aqueous compound interacts with the proteins and phospholipids in the cell membrane, generating reactive oxygen species that can trigger necrosis. With a preferential interaction with membrane proteins, Pt-protein binding constants fall within the range of 10^4 and 10^6, while Pt-lipid binding is around 10^2. [49]

1.6. Primary Goals of the Thesis

Throughout this PhD Thesis, the primary goal was to develop an innovative nanomaterial designed for a dual therapeutic approach, combining chemotherapy and thermal therapy. This strategy was driven by the aim to achieve a synergistic effect through a single, integrated nanosystem capable of delivering simultaneous chemotherapy and magnetic hyperthermia. To this end, we engineered a novel type of nanosystem composed of a magnetically-responsive, lipid-based nanocarrier for chemotherapeutic cisPt, which we refer to as **synthetic magnetosomes**. The complete process along this work included:

- Synthesizing and characterizing synthetic magnetosomes with optimized magnetic responsiveness and drug loading capacity.
- Evaluating the heating efficiency of these magnetosomes under magnetic fields and their drug-loading capabilities.
- Conducting a systematic investigation into magnetosome-cell interactions, focusing on cytotoxicity and cellular uptake.
- Performing *in vitro* tests to assess the effects of chemotherapy and magnetic fluid hyperthermia using these magnetosomes, aiming to establish their synergistic potential.

Throughout these years, all efforts, encompassing theoretical approaches, experimental design, and instrumental developments, were consistently directed towards producing and testing this novel nanovector, potentially able to integrate chemotherapy and magnetic hyperthermia applications using one single nanoplatform.

CHAPTER 2

Materials and methods: synthesis and characterization

"…I'm learning from the past, I'm learning.
You've always been the one but I'm learning.
Toda la vida soñando, en este mundo hecho de papel
Tengo los pies en el cielo.El corazón vuela alto también
Still making mistakes, I keep learning.
I'm making myself."

Fuel Fandango

2.1. Introduction

During the development of this doctoral thesis, many adaptations and improvements had to be made before the successful and reproducible production of the cisPt-loaded synthetic magnetosomes. Reproducibility and data availability are two cornerstones of good scientific deontology by ensuring that the scientific body of knowledge remains verifiable, reproducible, and accountable. The great amount of time and effort spent in this experimental work led us to value the importance of reporting the complete set of data that is actually required for the system to be reproduced in any other laboratory. This chapter is aimed to provide those key protocols, the step-by-step experimental for a) the synthesis of magnetic nanoparticles (MNPs), b) synthesis of liposomes (LB), c) preparation of synthetic magnetosomes (LN), and d) the obtention of the final drug-loaded (cisPt) magnetosomes (LNC). We provide the details of sample preparation for the different techniques used, aimed to the psychochemical characterization of these nanosystems and, when required, the specific modifications applied in experimental setups and quantification protocols. We also included the generalities of the cell culture preparation and the different techniques used to evaluate the cell viability and the toxicity of nanosystems.

2.2. Synthesis and functionalization of MNPs

Zinc-doped magnetite particles, $Zn_xFe_{3-x}O_4$ were synthesized by thermal decomposition of iron acetylacetonate 3 $(acac)_3$ and zinc $acac_2$ in organic solvents and in the presence of oleic acid and oleylamine as surfactants [54] [55] [56]. Once the particle size was defined, it was decided to modify its magneto crystalline anisotropy by varying the stoichiometric composition of the particle $Zn_xFe_{3-x}O_4$ with 0,1<x<0,5. For a typical preparation, 12 mmol of acac, we change the ratio between $Fe(acac)_3$ and of $Zn(acac)_2$, and dissolved in 8 mmol of Oleic Acid (OA), 12 mmol of Oleylamine, 4 mmol of 1,2 Octanediol and 40 ml of benzylether with a fix and characteristic boiling temperatures. A heating mantle for spherical flask with power control was used. Particularly, a three mouths glass flask reactor of 250 mL was employed for the synthesis. In each mouth of the balloon complete the setup, a glass stirring with anchor shape connected to a mechanical controlled stirrer, a bulb reflux condenser, a temperature sensor and a nitrogen flow hose, Figure 2.1 show the setup arrangement.

Figure 2.1. a) Schematic representation of the experimental set up used for MNPs synthesis. b) Picture of the experimental set up during the cooling fast process. In both figures, we have detailed the instrumentation used.

First, to evaporate all the possible water, the mixture was heated up to 100 °C with at $(\Delta T/\Delta t)_1$ for 20 minutes under mechanical stirring (50 rpm) and in a flow of nitrogen gas(0,4ml/min). Secondly, the reaction was heat up until the stabilization temperature (T_{St}) 200°C with at $(\Delta T/\Delta t)_2$ for 20 minutes, in this process the acac reactive mixed with OA. Then, the solution was heated up until the boiling temperature of benzylether, 300 °C, called final synthesis temperature (T_{FST}) at rate of $(\Delta T/\Delta t)_3$. The iron- and zinc- oleic complexes decompose with this raise of temperatures, from T_{St} to $T_{FST.}$ The final particle size is clearly related to the time during the synthesis product is maintained at T_{FST}. Figure 2.2 shows the experimental temperature profile followed during the synthesis process for the five MNPs samples and Table 2.1 summarized the experimental conditions. After synthesis, the MNPs were cleaned by sonicating the synthesis product with ethanol and collecting them with a strong neodymium magnet. Finally, the precipitate was resuspended in toluene and kept in a water bath at 40°C overnight.

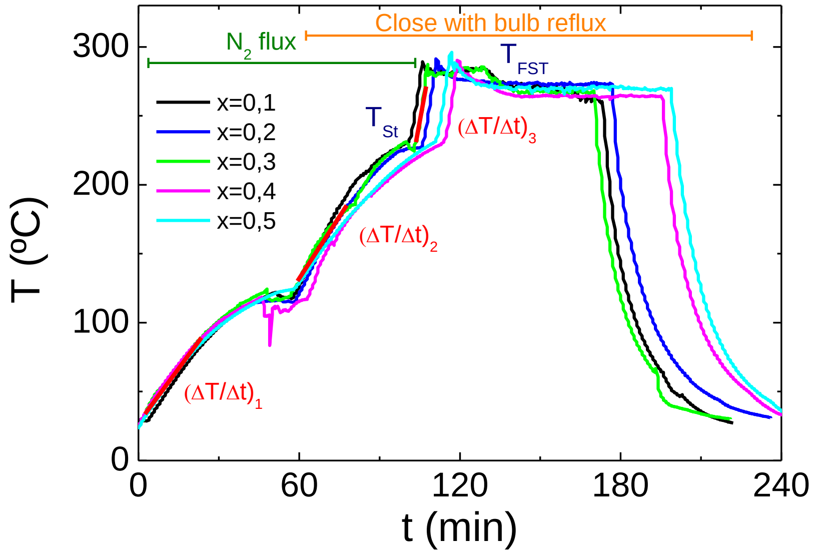

Figure 2.2. Temperature profile during the synthesis of the series of $Zn_xFe_{3-x}O_4$ MNPs.

Table 2.1. Experimental condition obtained during the synthesis of $Zn_xFe_{3-x}O_4$ MNPs.

$Zn_xFe_{3-x}O_4$ $x =$	$m_{Zn(acac)3}$ (mM)	$m_{Fe(acac)2}$ (mM)	$(\Delta T/\Delta t)_1$ (°C/min)	$(\Delta T/\Delta t)_2$ (°C/min)	$(\Delta T/\Delta t)_3$ (°C/min)	$T_{MÁX}$ (°C)	$\langle T\rangle_{FST}$ (°C)	Δt_3 (min)
0,1	0,4	11,6	2,6	3,8	11,7	289	274±8	66
0,2	0,8	11,2	2,6	3,6	12,0	291	274±3	65
0,3	1,2	10,8	2,6	3,1	12,9	287	274±7	62
0,4	1,6	10,4	2,6	3,3	10,7	290	267±5	76
0,5	2,0	10,0	2,5	2,6	11,1	296	271±4	82

Thermal decomposition method using acetyl acetonate as liquid medium will provide a final colloid that is organic based, with MNPs coated by a shell of oleic acid. Since this type of material cannot be directly applied to *in vitro* or *in vivo* experiments, we have used a protocol for the exchange of oleic acid to a citrate shell on the MNPs to be dispersed in water, as described for Hatekayama et al. in [57] with a few adaptations. In a 250mL glass bottle put 540 mg of MNPs and add 3mmol of trimethylamine (TMA) dissolved in 12mL of dimethyl sulfoxide (DMSO), previously prepared, this solution will act as a temporary coating agent. Sonicate for 4 hours, checking that the temperature does not exceed 40°C. Clean with 40 mL of 70% ethanol and collect with a magnet, repeat this process three times, dry with nitrogen. Resuspend in 20 mL of an aqueous solution of 0,1 M sodium citrate with pH=7.0. Sonicate the mixture overnight. 70 ml of 1,4 dioxane were added and the MNPs were precipitated with a magnet and dried with nitrogen. Precipitated MNPs were resuspended in deionized water and dialyzed for 4 hours to remove excess citrate. Details of the procedure are described in Figure 2.3.

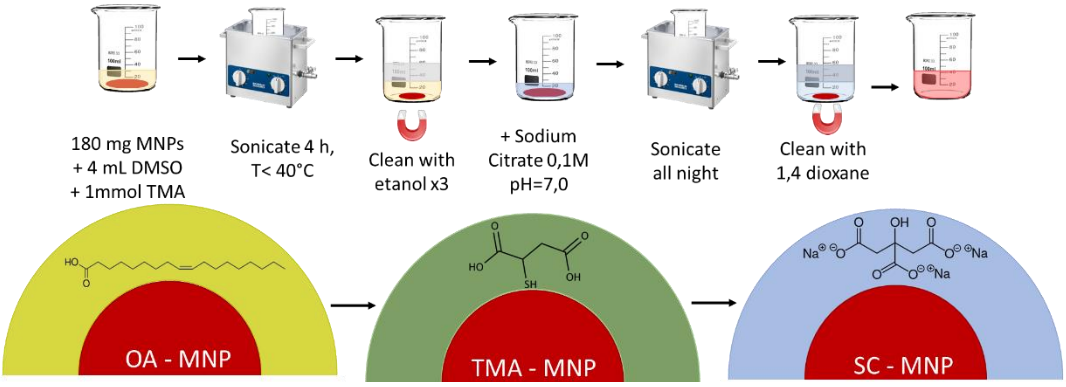

Figure 2.3. Details of Hatekayama et al. process for exchange of oleic acid recover to citrate-shell.

2.3. Manufacturing of synthetic magnetosomes

The liposome synthesis process has two fundamental parts, first the formation of multilamellar vesicles (MLV) and their subsequent extrusion for the formation of unilamellar vesicles or liposomes (LB). All the LB and LN in this work were synthetized by reverse phase evaporation method (RPE). The RPE method consists of mixing the organic phase (Figure 2.4 1), where the lipids are dispersed, with the aqueous phase (Figure 2.4 2), a solution of drug and MNPs, creating a meta-stable water-in-oil emulsion (Figure 2.4 3). Controlled evaporation of the organic phase (Figure 2.4 4) to form a gel (Figure 2.4 5), to finally collapse into an aqueous system (Figure 2.4 6), with MLV.

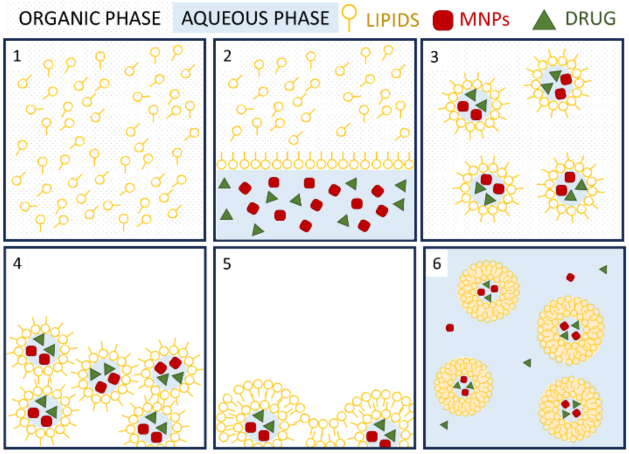

Figure 2.4. Explanatory diagram of the main steps in the RPE method for the synthesis of LN. (1) lipids dissolved in solvent. (2) organic phase + aqueous phase with MNPs and drug. (3) water-oil emulsion. (4) solvent evaporation processes. (5) gel-like state. (6) MLV loaded with drug and MNPs, dispersed in water.

To prepare 10mL of liposome at 10mM lipids concentration. We use a 1:3 ratio of aqueous phase: organic phase in a round flask of 100 mL. The aqueous phase consists of buffer citrate, and if required MNPs and cisPt. 45% 1,2-dipalmitoyl-sn-glycero-3-phosphocholine (DPPC),20% dimethyldioctadecylammonium bromide salt (DODAB), 30% of cholesterol and 5% of 1,2-distearoyl-sn-glycero-3-phosphoethanolamine-N- [methoxy(polyethylene glycol)-2000] (ammonium salt) (PEG), dissolved in chloroform and dispersed in diethyl ether form the organic phase. In a water bath at 55 °C and using an Ultrasonic Vibra-cell VCX 130 processor with Ti−6Al−4V (6 mm) tip sonicator inside a flask, at 70% power, transmitting energy to merge the two-phase system. This semi-stable solution is placed, in a rotary evaporator at 200 rpm, in a water bath at 55 °C at a gentle and controlled vacuum of 0.2 mmHg. The organic phase evaporated and continuously condensed by the cold coil accumulates in the collector balloon. Once all the organic phase has evaporated, a " slime " sticks to the bottom of the round flask. Gradually raise the vacuum and hold at 0.5 mmHg until the system collapses and becomes a homogeneous liquid emulsion. Increase the vacuum to 0.8 mmHg and maintain the pressure for 10 min. Remove the emulsion from the rotary evaporator and leave it overnight in a dissector. Figure 2.5 show a picture of the setup during the formation of MLV for the RPE method.

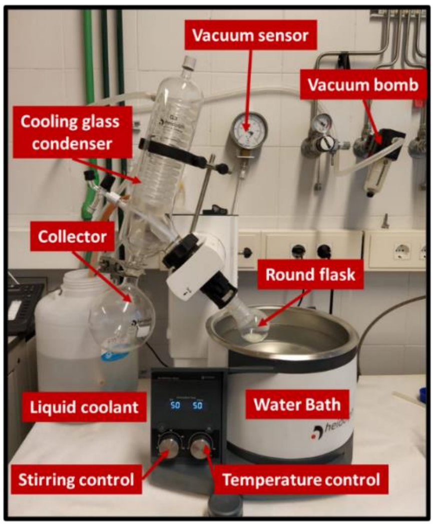

Figure 2.5. Rotavapor used during the MLV synthesis by the RPE method.

Finally, the liposome was obtained by the extrusion process. For large volume of liposome, we use the commercial Lipofast L-50 extruder (Figure 2.6 b)) from avestin®. Figure 2.6 a) was taking from the Avestin Inc. handbook and detail the interior of the extruder. Hot water is circulated in the jacked cylinder to provide an internal temperature of 55°C, the MLV is added to the reservoir and the nut is closed. In the extruder filter holder, we place an upper and lower drain disc, between them a polycarbonate membrane of defined pore size, and hydrate with water.

When the temperature inside the reservoir is reached, we increase the pressure inside using nitrogen gas, forcing the MLV emulsion pass through the membrane. The extrusion process is repeated 5 times with each membrane before moving to a smaller pore size membrane. The final volume is collected in a sterile falcon. Retention of MNPs and lipids on the membrane was observed.

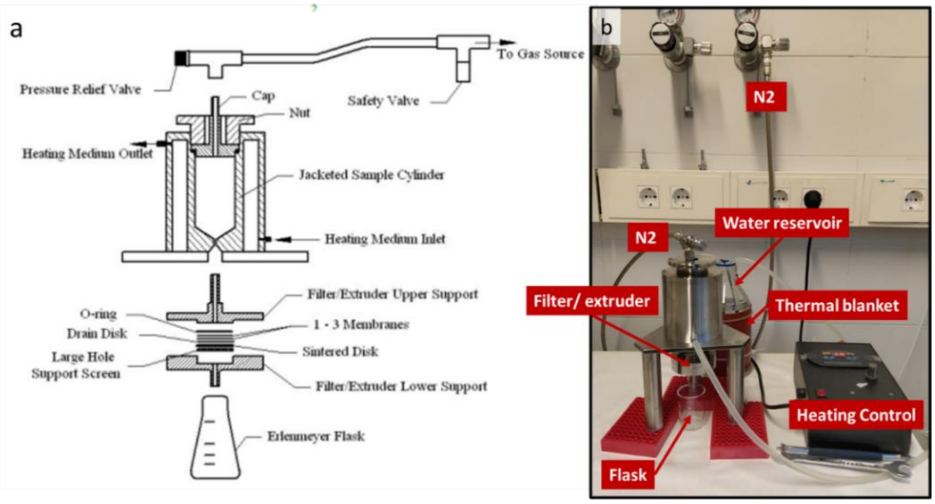

Figure 2.6a) Extracted from the Avestin® handbook: a detailed diagram of the Lipofast L-50 extruder system. b) Image showcasing the setup of the extruder developed in our laboratory, including a custom-built temperature control mechanism for the jacket cylinder.

2.4. Physicochemical characterization

The physicochemical characterization of the nanosystem, i.e. MNPs, LB, LN, LC and LNC, was carried out by different techniques:

a) Transmission electron microscopy (TEM) was used to characterize the morphology and distribution of the samples. A FEI Tecnai T20 microscope at 200kV was employed to collect TEM image, from LMA service of Zaragoza University. The high resolution (HR)-TEM image was obtained with a FEI Tecnai F30 microscope, and an image corrected Titan from FEI Tecnai with an objective aberration corrector of CEOS company, from LMA service of Zaragoza University. Samples for TEM were prepared from a dilute suspension of these in a respective media, like toluene or water. One drop was placed on a carbon-coated copper grid and allowing the solvent to evaporate at room temperature. The average particle size was evaluated by measuring the largest internal dimension of 600 particles with the free commercial J image program. The respective histogram was collected following the norm $N^{\underline{o}}\ of\ \ rows = 1 + \ln{(N^{\underline{o}}\ particles)}$. The respective distribution, Gaussian, was fitted to obtain the media size ($\langle d \rangle$) and the statistical distribution (σ_d).

b) Tinction technique and cryogenic electron microscopy (cryo-TEM) were used to observe the distribution and morphology of lipid samples like LB, LC, LN and LNC. In the tinction technique, a diluted sample drop was placed on a carbon-coated copper grid and wait until the water evaporate. In a clean surface, added one drop of uranyless, our material of tinction, and leave the carbon grill part on the uranyl drop for 60 seconds, softly remove the excess and leave dry. In Cryo-TEM we can observe the original shape of liquid sample of 1µm maximum size, realizing a thin layer of amorphous ice. In the vitrification process, a positively charged grid with a small sample drop is rapidly cooled in liquid ethane. For this procedure we used a Vitrobot (Thermofisher Scientific) for cryo-sample preparation, at the LMA facilities. A cryo-holder was used to obtain the TEM images. The dry ice layer protects the sample from the electron beam and ensures that it does not interfere with the high vacuum of the microscope column.

c) Dynamic light scattering (DLS) measurement were performed in a Zetasizer nano Malvern instrument, to characterize the hydrodynamic size of the nanosystem in water. The evolution of the heating and cooling of LB and LN was studied by programming a temperature ramp. The experiment was performed in 1mL glass cuvette, cover the range between 20°C - 80

°C with a reading every 2°C, with a ramp of 1°C/min, with 5 min of stabilization at each temperature reached and 3 min of a triplicate measurement. The thermodynamic size dependency of lipidic sample was characterized by the correlation function, the count rate, and the polydispersity index (PDI). The parameters at 25°C, used for the lectures in water was $\lambda = 658\ nm$, refractive index real 2,420 and imaginary 0,100.

d) The analysis of characteristic x-rays to provide chemical information is the most widely used microanalytical technique in scanning electron microscopy (SEM), usually called energy dispersive x-ray spectroscopy (EDS). For the element detection and quantification in our MNPs, a FEI INSPECT F equipped with a field emission gun of single crystal tungsten and an INCA PentaFETx3 microanalysis system from Oxford Instruments, from LMA service of Zaragoza University, was used. The sample is fixed to the sample-holder with conducting carbon tape in order to assure that the current flows out of the sample. For the analysis the sample surface should be ideally flat and conductive, therefore, these are coated by carbon to avoid shadows and charging effects. The energy range for spectra acquisition, between 0 and 30 keV, was the double of the energy expected of the elements to identify.

e) Scanning transmission electron microscopy (STEM) combines the principles of TEM and SEM. In STEM, the electron beam is focused on a narrow probe which scans the sample in a bitmap pattern. EDS and electron energy loss spectroscopy (EELS) was performed. An analytical titan FEI with a CEOS company spherical aberration corrector was used with a monochromator and a high brightness source XFEG, from LMA service of Zaragoza University working at 60 kV.

f) The surface charge of the nanosystem was characterized using a ζ-potential Zetasizer nano Malvern instrument and a Brookhaven 90 plus.

g) A Hanna HI2214 pHmeter was used for pH measurement for a controlled temperature with a previous calibration performed with commercial patron.

h) The amount of organic-shell, citric shell and the lipid coated in the MNPs was calculated by the thermogravimetric analysis (TGA), an analytical technique used to determine a material`s thermal stability. The change of mass due to the heating of the sample was measured, this gives information about the chemical composition of the sample. Measurements were performed under inert atmosphere of N_2 following a temperature rate of 10°C/min, ending at 900°C with a stable sample weight. The powdered samples were characterized using a TGA/DSC 1 Mettler Toledo.

i) FT-IR (Fourier transform infrared) spectroscopy was used to analyze and verify the nature of the functional groups of the different Shell that recover the MNPs. The absorbance spectrum was taken from 4000 to 400 cm^{-1} on a Nicolet Impact 410 spectrometer. Powder samples were prepared drying some volume of the colloidal suspension and comparing the results of MNPs shell with the elements recovered during the synthesis process.

j) The Fe and Pt quantification were performed by an Agilent 4210 Microwave Plasma Atomic Emission Spectrometry (MP-AES). An air flow is used for running the sample trough a plasma for a multi element analysis with a detection limit down to ppm. 100µL of sample were attached with a water solution of HNO_3 and HCl, 1:3 ratio, to digest the metals in the sample and dispersed in water. Finally, the sample was filter using a hydrophobic PTFE filter of 0,22 µm, this filter ensures the total pass of these two elements without retain it. For each element to quantify, three wavelengths were selected by prioritizing the highest intensities and no wavelength superposition between the elements.

k) X-Ray Diffraction (XRD) on powder samples was carried out in a PANalytical Empyrean diffractometer by LMA service of Zaragoza University. XRD provides information about the lattice parameters of the crystalline structure of MNPs, the different crystallographic phases present in the sample and other parameters. In our case, XRD spectra were taken in $10° \leq 2\theta \leq 90°$ with a step of 0.01°, in continuous lecture mode. The data was analyzed with the X´Pert High Score PANalytical program.

l) The superficial composition of MNPs and LN samples was characterized by X-ray photoelectron spectroscopy (XPS), performed for LMA service of Zaragoza University with an Axis Ultra DLD (Kratos Tech). For the qualitative and quantitative elemental composition of the powder of the samples, a previous clean of 3 nm with an ion bean was performed to roughen the coating of the samples. The data was analyzed with the software casaXPS.

2.5. Determination of iron, lipids and cisPt contents

Ultraviolet/Visible (UV/vis) spectrometer is employed to quantify the light absorbed and scattered by a sample. A sample with a characteristic UV/vis spectrum was placed in a quartz cuvette between a light source and a photodetector, the intensity of the beam of UV/vis light was measure before and after passing through the sample. Following a specific wavelength was possible to quantify the presence of iron, lipids and cisPt for different systems.

2.5.1. Iron quantification

The Fe quantification protocol was carried out with the iron-thiocyanate complex following the specification resumed for Adams [58] with a few changes. First, the calibration curve (Figure 2.7) was performed with a standard solution of $FeCl_3$ 0,0010 M, in a range between 0 to 0,01 mg/mL.

Using a clean volumetric flask of 10 mL, seed the different concentration of standard concentration for the point in the calibration. Added 500 µL of HNO_3 and 500 µL 6M chlorohydric acid, wait per one hour. This step becomes crucial for the samples measurements for ensure the reduction of the iron to Fe^{3+}. Full up the flask with 6M HCl. In a quartz cell refill with 500 µL of this solution and 500 µL of thiocyanate (SCN). Read in a UV-Spectrometer at λ=478 nm. In the case of sample use a known volume sample, like 50 µl and continued with the same protocol.

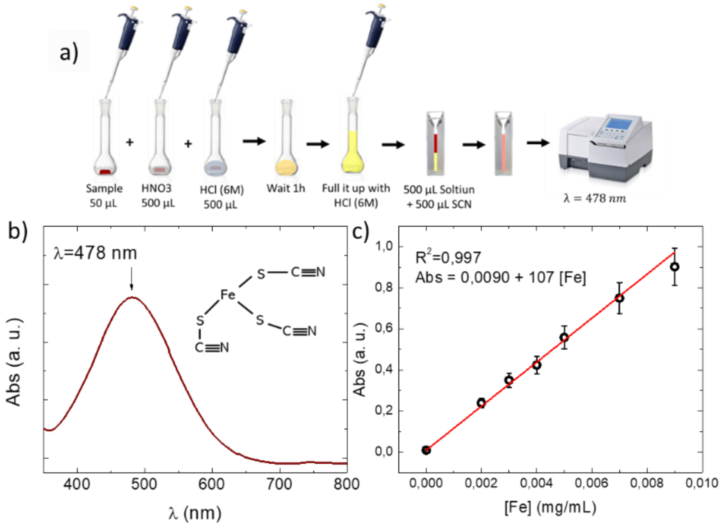

Figure 2.7. a) Details of experimental process for the iron-thiocyanate complex formation and posterior lector in UV spectrometer. b) UV spectrum of the iron-thiocyanate molecule. C) Iron calibration curve with UV spectrometer for λ=478 nm.

This iron calibration technique was utilized in various sections of this thesis, most notably for quantifying the amount of iron absorbed by cells to determine the specific loss power (SLP) in hyperthermia experiments. In every instance, we established calibration curves that included both the gelatin and a blank cell baseline to mitigate any potential extraneous contributions. Additionally, to confirm the reliability of the protocols, we examined the time-dependent reaction between the iron solution (previously oxidized in acid) and the SCN, ensuring that the staining properties remained consistent over time. The experiment was evaluated using two commercial standard Fe and $FeCl_3$. It was found that after 40 min of reaction the absorption values at the λ=478 nm reduced a 6% from the starting value. These results are summarized in Figure 2.8.

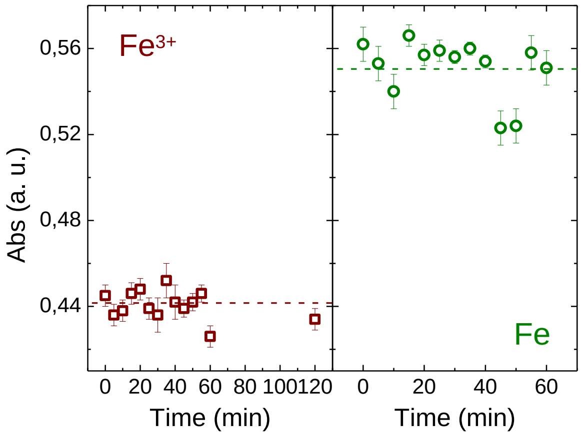

Figure 2.8. Time evolution of Fe-SCN complex, with two commercial iron solution of Fe3+ (brown square) and Fe (green circle). The dotted line indicates the mean value of all points.

An additional series of control experiments were performed to assess the minimum amounts of HNO_3 required to fully oxidize the iron present in the samples to Fe^{+3} species, needed for a correct determination of iron amounts by UV-vis with the SCN stain. We used increasing concentrations of HNO_3 and commercial standard solutions of Fe and $FeCl_3$, adding increasing HNO_3:HCl(6M) ratios of 0:1, 1:1 and 2:1. The results (Figure 2.9) showed that the use of *aqua regia* is necessary to ensure the complete oxidation of the sample, and also that the excess of HNO_3 does not interfere with the spectrophotometric signal.

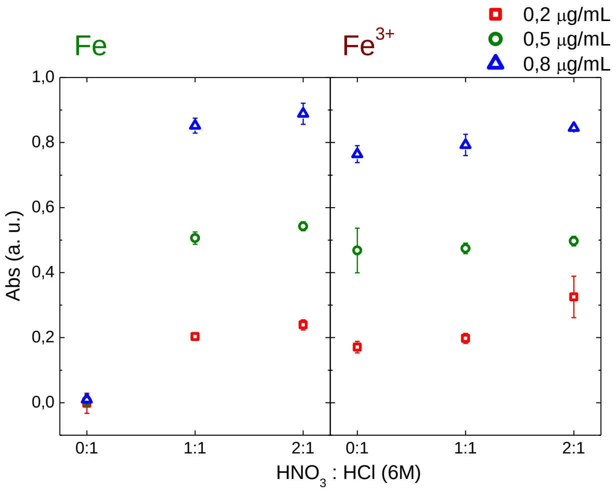

Figure 2.9. Comparison of the influence of nitric- to hydrochloric acid ratio on the reactivity of commercial iron (left) and Fe^{3+} ions (right) for different concentrations.

2.5.2. Lipids quantification

For the quantification of lipids in the nanocarrier we use 1,2-dipalmitoyl-sn-glycero-3-phosphocholine (DPPC) like lipid standard following the steps of Stewart [59]: In 2 mL Eppendorf added the respective volume of stock solution for study values between 0 - 0,1 mg/mL and with chloroform complete until 750 µL. Work in box with ice to avoid different concentration for the evaporation of chloroform. The 750 µL of ammonium thiocyanate (NH_4SCN) were added and mixed vigorously with a vortex to ensure the formation of the complex. Centrifuge the biphasic system at 10000 rpm for 3 minutes, carefully separated the chloroform phase at the bottom and read in a UV- spectrometer (Figure 2.10a) at λ = 488 nm. The calibration curve was fitted in Figure 2.10 c). For the measure of lipidic samples make sure that the approximate value is considered in the range of calibration curve, normally a dilution of 1:10 or 1:100 is needed. Put 20 µL of sample in 2 mL eppendorf and evaporate the aqua part, added 750 µL of Chloroform and the solution of ammonium ferrothiocyanate and follow the same step of the calibration curve.

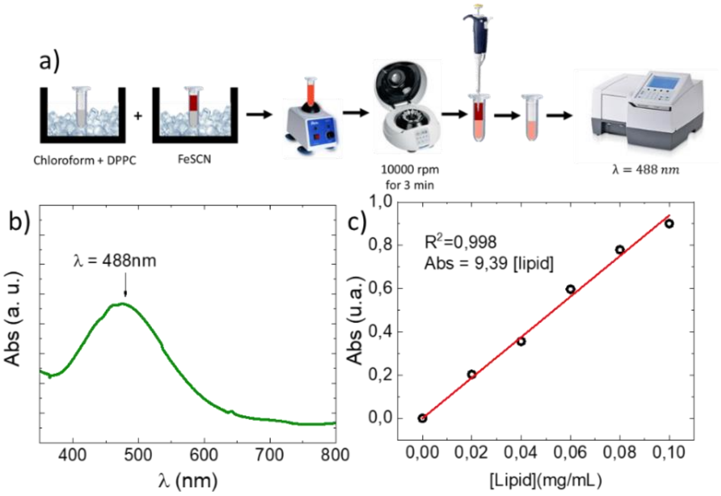

Figure 2.10. a) Step by step of lipid-ferrothiocyanate complex formation and posterior lector in UV spectrometer. b) UV spectrum of liposome- ferrothiocyanate. C) lipid calibration curve with UV spectrometer for λ=488 nm.

2.5.3. CisPt quantification

For the quantification of cisPt encapsulated in liposome we first broke the bilipid bilayer using triton x100 and mixed with a vortex. Then we followed the procedure described for Basotra et. al. [60] to form the complex of cisPt – o phenylenediamine (OPDA). Working in a 1,5 mL eppendorf, we caried the calibration curve between 0 to 1,6 µg/mL, adding 20 µL of a 1:10 dilution of liposome and different solution of cisplatin stock 100 µg/mL. In the case of the samples, use 20 µL of 1:10 dilution. Added 200 µL of 1,4 mg/mL of OPDA diluted in phosphate buffer (pH 6,8). The solution was heated per 10 minutes at 90 °C. Wait until the system cool down at room temperature and refill until 1 mL with dimethylformamide, centrifuge and using a UV spectrometer read in the wavelength 706 nm. Figure 2.11 show the UV spectrum of cisPt-OPDA complex in function of different cisPt concentration, and the respective calibration curve.

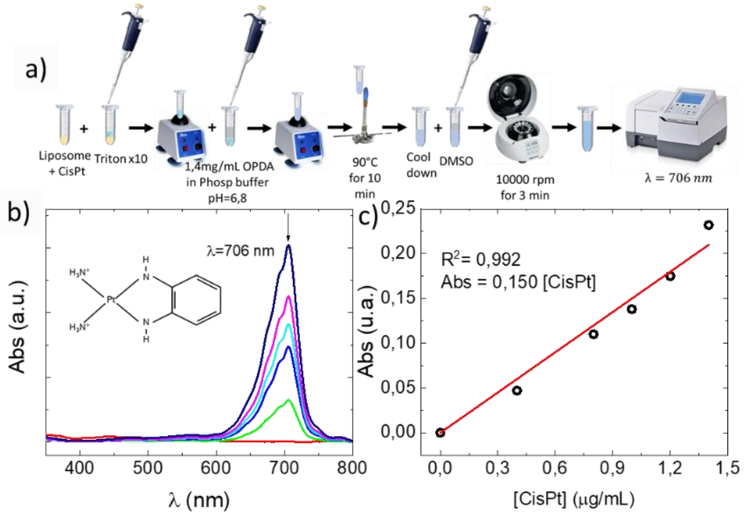

Figure 2.11. a) Step by step of cisPt+o-Phenylenediamine complex formation and posterior lector in UV spectrometer. b) cisPt+o-Phenylenediamine and it is UV spectrum at different cisPt concentration. C) cisPt calibration curve with UV spectrometer for λ=706 nm.

2.6. Study of the power absorption of MNPs and LN

The Specific Loss Power (SLP) is the value of the power loss of magnetic fluid in presence of an alternating magnetic field. The theoretical framework was explained in chapter 1 and 4. The heat power of MNPs and LN under an external alternating field was measured as a function of frequency and amplitude field to find the region of SLP increment for the *in vitro* assay. The experiments were carried out in a commercial magnetic field applicator (G2 D5 nB Nanoscale Biomagnetics S.L.), applying magnetic fields amplitudes in the range $7.96 \le H_0 \le 45.2\ kA/m$ and frequencies $150 \le f \le 765\ kHz$. Calorimetric experiments were performed on 1mL of sample in a chromatography vial coil-centered whit a vacuum insulated Dewar connected to a vacuum pump (10^{-7} mbar), measuring the temperature evolution with an optic fiber placed in the center of the sample.

Homogenous samples were analyzed under various media conditions, as detailed Figure 2.12. The heat capacity (Cp) of gelatin and paraffin were determined by averaging their distribution values (shown in Figure 2.12) over the operational temperature range of $10°C < T < 40\ °C$. The concentration of MNPs in the colloids for all samples was typically ≈1mg/mL. The actual concentration value was verified after each experiment using the SCN complex measurement technique with a UV spectrometer, as described previously in this Chapter.

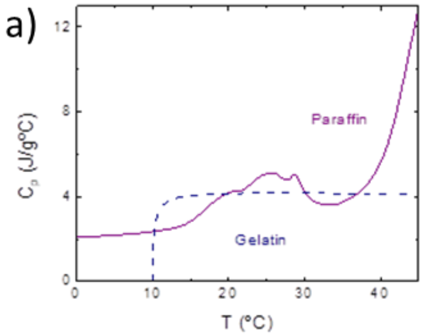

b)

Medium	$\delta_m \left[\frac{kg}{L}\right]$	$C_p \left[\frac{J}{g\ °C}\right]$
Water	1	4.186
Gelatin	0.9	4.186
Toluene	0.867	0.8368
Paraffin	0.9	4.71

Figure 2.12. a) Temperature-dependent Heat Capacity (Cp) for the Gelatin and Paraffin used in SLP experiments. b) Density (δ_m) and specific heat capacity (C_p) of various media employed in Specific Loss Power (SLP) experiments.

The values of Specific Loss Power (SLP) were measured as a function of frequency and field, mapping for each different system the $H - f$ space within the available experimental range. To obtain maximum reproducibility in our data, measurements were done by triplicate, each time in a single gelatin- or paraffin-fixed sample. To achieve this, the magnetic field applicator was programmed to operate at a fixed frequency, increasing the field strength in increments of 1.6 kA/m, starting from 8 kA/m up to the maximum field for each frequency, as depicted in Figure 2.13a. The duration of the field application was determined from consideration of the gelatin's melting point to ensure the sample's integrity throughout the experiment. The collected data, stored in a .txt file, was processed using a Python script designed to calculate the average SLP value and its standard deviation at each field level for a specified frequency. SLP estimation was based on the optimal fit line spanning the entire range where the applied field matched the selected field, which is highlighted in green in Figure 2.13b.

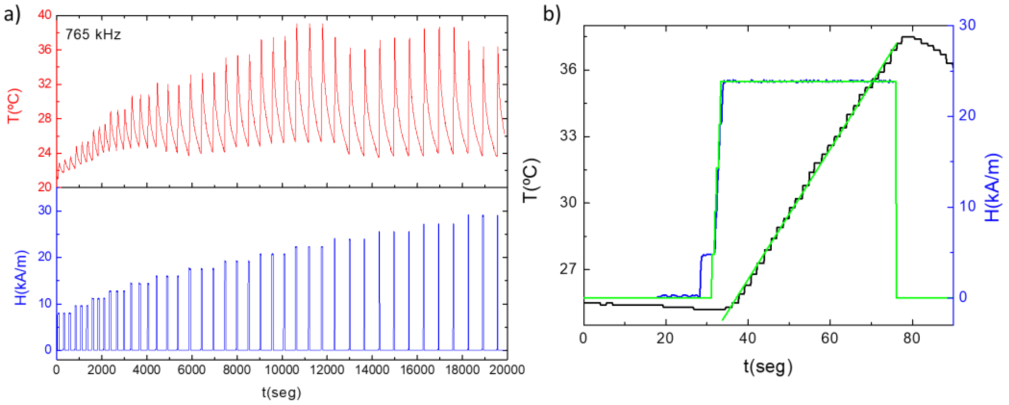

Figure 2.13. a) Typical temperature profile (in red) of an experiment on a single gelatin-fixed sample at a constant frequency, captured during a continuous measurement where the applied magnetic field (H) is varied (shown in blue). b) Displayed in green is the best-fit line, representing the rate of temperature change ($\Delta T/\Delta t$), across the region with a constant magnetic field (H). This line was used to estimate each SLP value.

2.7. Protocols for *in vitro* assays

The *in vitro* experiments performed in this thesis and which results are details in chapter 5, were carried out in two cells line:

a) BV-2 cell line: a type of microglial cell derived from C57/BL6 murine.
b) PAN02 cell line: A ductal adenocarcinoma murine model of *pancreatic* cancer

The BV2 were cultivated in Gibco™ Dulbecco`s modified Eagle`s medium (DMEM) (reference:12491015), while the PAN02 were cultivated in Gibco™ DMEM with high glucose and pyruvate (refence: 41966029). Both media were supplemented with 10% fetal bovine serum, 100 µg/mL penicillin, 100 µg/mL streptomycin and 2mM L-glutamine. The cells were maintained at 37°C in a saturated humidity atmosphere at 5% CO$_2$.

2.7.1. Toxicity and cell viability

The cytotoxicity of the nanosystems (MNPs, LB, LC, LN, LNC and cisPt) on the cell lines was tested at increasing concentrations of 0, 12.5, 25, 50, 100, 200 µg/mL of MNPs and 0, 1, 5, 10 mM cisPt, at different incubation times of 0, 0.5, 2, 4, 6, 24, 48 hours. A starting number of $30x10^3$ cells in the exponential growth phase were seeded into a 6-well plate and incubates overnight at 37°C with 5% CO$_2$. The media was replaced with the increasing MNPs or cisPt concentrations mentioned before, mixed with new medium until fill up the 2mL per well. The volume of treatment added to cells was never greater than 10% of the volume of the well worked, to avoid cellular stress. The cell viability was assessed by three different techniques: Trypan blue (TB), flow cytometry and plate reader using presto blue (PB).

2.7.1.1. Trypan blue

Trypan blue (TB) is a commercial chemical compound used as an exclusion assay to selectively stain cells. In the case of dead cell, the membrane is disrupted, and TB can pass through them; in contrast, the membrane of living cells is intact, so the dye cannot pass across it (Figure 2.14). Finally, in this exclusion method, blue-dyed and unstained cells are counted using a Neubauer chamber. All TB viability assays were performed by taking 10 µL of TB solution mixed with the same amount of a diluted dispersion of cells of known volume. Then, 10 µL of the 1:1 mixture was placed in a Neubauer chamber for observation under a brightfield optical microscope (Figure 2.14).

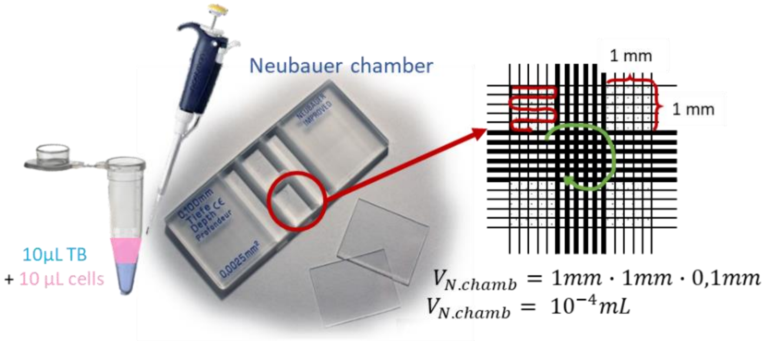

$$\frac{Cell\,number}{mL} = \frac{Total\,cell\,number}{4} \cdot 2 \cdot \frac{1}{V_{N.chamb}}$$

Figure 2.14. TB exclusion method use a Neubauer chamber to count the cell number in 1mL, distinguish between death and live cells.

2.7.1.2. Flow cytometry

Flow cytometry is a technology that is used to analyze the physical and chemical characteristics of particles in a fluid as it passes through one laser reader. Cell components are fluorescently labelled and then excited by the laser to emit light at varying wavelengths. In flow cytometry a vacuum pump circulates the sample to be analyzed in front of a light detector that classifies each event by size and membrane complexity (Figure 2.15a), here we select a region with the cells to work with. During cell death some morphological changes characterize the process such as loss of membrane integrity (asymmetry and attachment), plasma membrane blebbing, condensation of the cytoplasm, apoptotic bodies formation and nucleus/cleavage of DNA. Annexin V and propidium iodide was used as dyes for the selective cell staining. Annexin V could bind to apoptotic cells because it has high affinity for phospholipid phosphatidylserine, a chemical compound externalized onto the membrane by apoptotic cells. Second, the membrane of damage and/or dead cells are permeable to propidium iodide. Therefore, four combinations are possible:

A1- sites stained only by propidium iodide represent cellular traces,
A2- dead cells stained by both compounds,
A3- viable cells that cannot interact with either dye,
A4- only apoptotic starting cells stained with annexin.

Using dead cells, Figure 2.15 shows the cytometric calibration procedure.

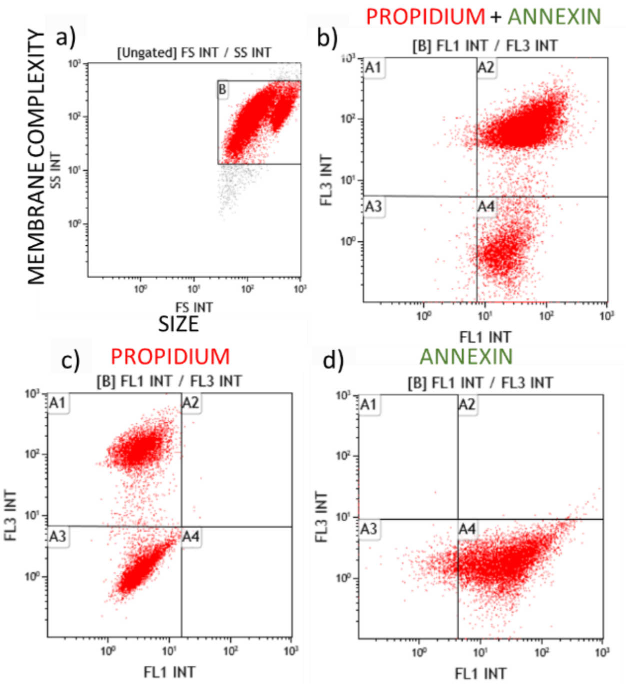

Figure 2.15. Calibration Example for Flow Cytometry data. a) Distribution of events categorized by size and membrane complexity. Staining of dead cells using b) propidium iodide + annexin V, c) propidium iodide alone, and d) annexin V alone.

Flow cytometry assays were performed using annexin V and propidium iodide, fluorescence molecules from commercial kits (Invitrogen™ and Thermo Fisher eBioscience™ Annexin V apoptosis detection kit FITC). PAN02 cells were washed several times with phosphate buffer saline and centrifugation, pre-cleaned with binding buffer, each sample was resuspended in annexin-binding buffer (1,25 µL:100 µL) and incubated for 20 min in the dark at room temperature. After incubation time, excess staining was removed with binding buffer. The sample was stained a second time with a solution 2,5 µL:100 µL solution of propidium iodide - binding buffer. Analyses of all samples were performed using a BD FACS Calibur Cytometer and BD cell quest pro Software.

2.7.1.3. Presto blue

Presto blue (PB) is a commercial cell viability compound formulated from resazurin, a cell permeable blue compound non-toxic and non-fluorescent. Metabolically active cells convert resazurin to resorufin, a red-fluorescent indicator (Figure 2.16). The amount of fluorescence produced is proportional to the number of living cells.

Cell viability experiments were performed in a 96 well plate with10 µL of PB added to each well, incubated for 10 min at 37°C and read on an ELISA microplate photometer HIPo MPP-96. Absorbance can be quantified at 570 nm and fluorescence at 560/590 nm (excitation/emission).

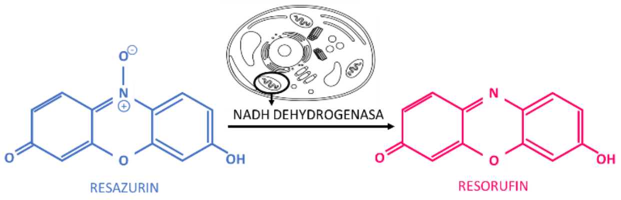

Figure 2.16. Mitochondrial resazurin reduction to resorufin scheme.

2.7.2. Interaction and internalization of nanosystem

TEM image allowed observe the cell structure and distinguish the sample interaction with the cell membrane and their position on the cytoplasm and organelles. Whit this technique it was possible to observe the cell membranes and the internal organelles with a higher spatial resolution than optical microscope following some protocols to magnify the contrast which will be described in this section. Cells ($3x10^4$ cells/well) were seeded in a 6-well-plate in 2 ml of culture media. Next day, the samples to study (LB, LN, MNPs, LNC, LC and cisPt) were added and incubated for 4 hours. After incubation, the cells were washed with phosphate buffer saline, detached, and fixed with 2,5% Glutaraldehyde + 2% Paraformaldehyde in 0,1 M phosphate buffer for 2 h at 4°C. Secondly, the samples were centrifuged at 180 G for 10 minutes and washed three times in phosphate buffer. The samples were treated by the service of Electronic Microscope and Histology of the Investigation center Principe Felipe. There, the samples were stained with uranyl acetate, osmium tetroxide and lead citrate, to finally embedded in EPON® epoxy blocks. Ultrathin 70 nm sections were obtained by ultramicrotomy of epoxy blocks, and then mounted on a formvar and carbon double film supported on copper grid. The samples were observed in a Tecnai T20 (ThermoFisher Scientific) with image resolution of 0,24 nm at 200 kV of LMA service in Zaragoza University.

The MNPs internalized in both cells line was quantificated by UV/vis ferrothiocyanate complex method and by AES technique explained in 2.5. Also, AES technique was used to evaluate the mass of platin internalized on PAN02 cell.

2.7.3. *In vitro* exogenous hyperthermia assay

Exogenous hyperthermia tests were performed in an eppendorf model F1.5 thermomixer, which consists of a dry heat thermoblock with mechanical stirring (Figure 2.17). An electronic control allows setting temperature with high stability, and its possible select the time and percentage of mixed speed. 4 x 10^5 cells were detached and resuspended in 1,5 mL of medium in an eppendorf, whit one sample per time and temperature. The thermoblock was set to one temperature, and the eppendorf was introduced together with a control where the temperature was sensed, the treatment time was counted when the temperature treatment was arrived in the sensor. The set points ranged from 41 to 46 °C and were maintained between 5 to 45 min. Samples were removed at different times, 5 to 45 min, and seeded in triplicate in a 96-well-plate. Cells were incubated for 48 hours at 37 °C in a saturated humidity atmosphere containing 95% air and 5% CO_2. Viability percentage was calculated after 48 hours using the PB assay.

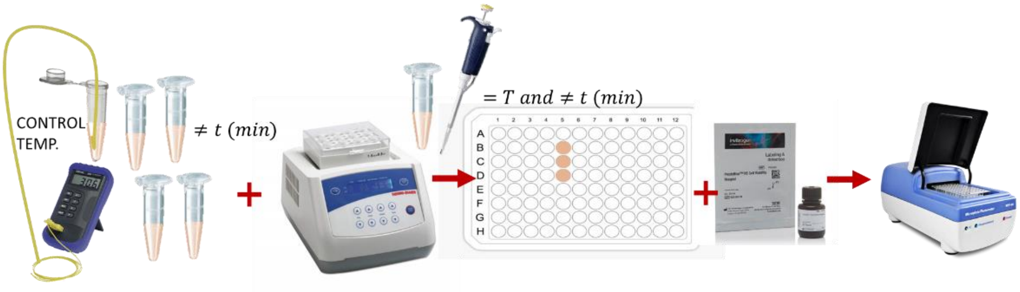

Figure 2.17. Step by step procedure describing the exogenous heating (EH) experiments using a hotplate, followed by assessment of cell viability.

2.7.4. *In vitro* combined treatments experiments: chemotherapy and magnetic fluid hyperthermia

We assessed the LNC nanovector as a potential adjuvant to enhance the efficacy of magnetic fluid hyperthermia (MFH) combined with chemotherapy (CT), aiming to achieve a synergistic effect and consequently reduce the dosage of cisPt. To this end, we conducted a series of experiments, taking into account various factors such as the concentration of internalized MNPs, *in vitro* SLP, cell seeding density, treatment temperature, application duration, etc. The experimental protocols are depicted in Figure 2.18. The first phase includes four control setups: cells alone, PAN02, and the test samples (MNPs, LN, and LNC) at identical concentrations, but without an applied magnetic field. The second phase involves examining the three systems under the influence of an external magnetic field. These tests were performed using a frequency of 568 kHz and a maximum field of 30 kA/m, employing the G2d5 commercial setup, as described in the preceding section.

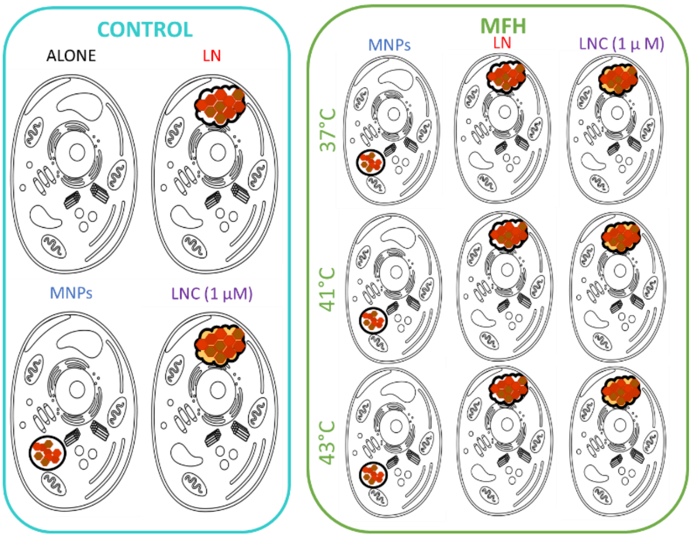

Figure 2.18. Diagram illustrating the synergistic effect assay. On the left in blue: control groups consisting of PAN02 cells alone, and those loaded with MNPs, LN, and LNC, all without an applied magnetic field. On the right in green: PAN02 cells combined with MNPs, LN, and LNC (concentration of 1µM) subjected to MFH treatment at varying temperature levels (39°C, 41°C, and 43°C)

Importantly, the magnetic hyperthermia device featured a capability for target temperature control. Through the selection of an appropriate working frequency and the setting of a desired target temperature for treatment, an integrated Proportional-Integral-Derivative (PID) system in the equipment regulated the applied field amplitude to achieve and sustain the specified treatment temperature.

Cell viability of MFH at different temperatures (39°,41° and 43°C) was studied maintaining the temperature for 10 minutes. For this purpose, $5x10^5$ cells were seeded in a T75 flat in 10 mL of culture media. The next day MNPs, LN and LNC were added at a concentration of 200 µg/mL of MNPs and 1µM of cisPt and incubated overnight in each flat. After incubation, the cells were washed with PBS three times and detached. The pellet was then centrifuged, collected with 200µL of DMEM and placed in chromatography vial (200 µL) with screw cap. A disinfected fiber optic was placed in the center of the sample to check the temperature. After the MFH treatment the samples were seeded in a 6-well-plate. Cells were incubated for 48 hours at 37 °C in a saturated humidity atmosphere containing 95% air and 5% CO_2. The viability percent was calculated after 48 hours by annexin and propidium iodide cytometry assay.

CHAPTER 3

Synthesis and physicochemical characterization of synthetic magnetosomes

"…ir y venir, seguir y guiar, dar y tener.
Entrar y salir de fase.
Amar la trama más que el desenlace.
Amar la trama más que el desenlace…"
J. Drexler

3.1. Introduction

Magnetoliposomes (ML) are novel formulations composed of liposomes and magnetic nanoparticles (MNPs), offering potential applications as carriers for diagnostic and treatment agents. Liposomes enhance the biocompatibility and stability of superparamagnetic particles, an advantage that has been harnessed for their use as contrast agents in magnetic resonance imaging [41]. As drug transport vector systems, ML can focus treatment on the target area using external magnetic fields, resulting in the possibility of on-demand drug release from a physical triggering effect[45]. Moreover, the raise in local temperature generated by ML could offer the possibility of simultaneous application of hyperthermia and chemotherapy.

The synergistic benefits of combining thermal therapy with chemotherapy (CT) or radiotherapy have been recognized for decades [46] and this possibility have been recently explored using ML, due to their capacity of using a single nanosystem for a combined treatment of magnetic fluid hyperthermia (MFH) and CT. Along this line of research, Pradhan et al. have observed synergistic effects in the KB cell line using MLs loaded with doxorubicin, at temperatures of 42,5°C and 43,5°C. In 2010, Yoshida et al. first introduced the combined *in vivo* therapy of MFH and CT using ML loaded with docetaxel in human MKN45 gastric cancer cells implanted in Balb-c/nu/nu mice[61]. In this work the formulation was injected directly into the tumor, and an alternating magnetic field ($f = 478\,kHz$; $H_0 = 6.36\,kA/m$) was applied to reach temperatures 42 < T < 43°C during 30 min. A significant decrease in tumor volume and a survival period of 6 months were observed in tumors treated with ML over 3 weeks compared to the untreated mice.

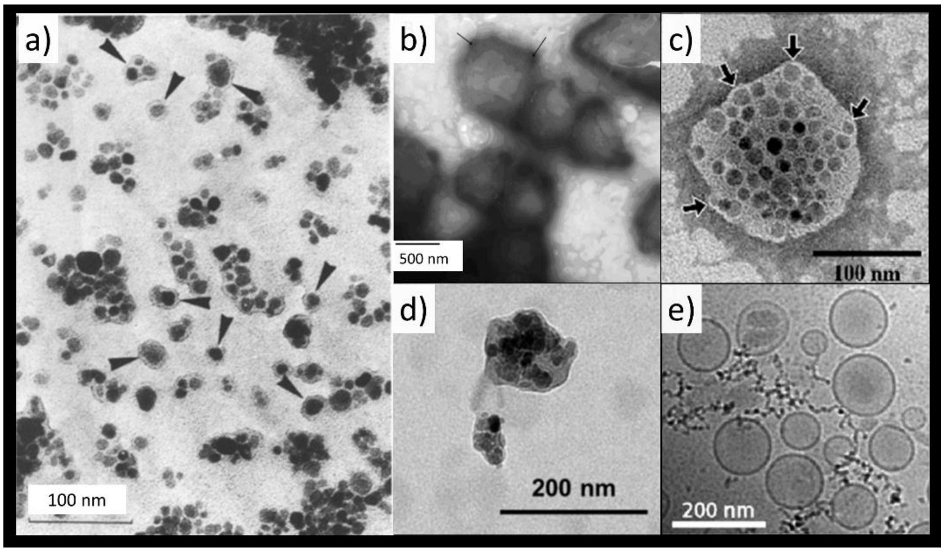

Figure 3.1. Magnetoliposomes founded in literature. Negative stained TEM images a)[40] c) [62] and d) [63]. Cryo-TEM images of ML b) [64] and e) [65] . The black arrows indicate the phospholipid bilayer.

Figure 3.1 show reported images of ML where MNPs coated by a lipid layer are distinguishable. In some cases, the common spherical structure of liposomes is lost in ML. In 1988, De Cuyper et al were the first to take a TEM image of ML, observing these array structures(Figure 3.1 a) [40]. Similarly, Pradhan et al. observed that ML loaded with oxaliplatin form chains (Figure 3.1 e)[65], resembling the arrangements formed by magnetosomes. Some reports of ML loaded with cisPt (Figure 3.1 b and c)[64] [62]and its analog oxaliplatin (Figure 3.1 d) [63] were found. Although synergistic effects between hyperthermia and cisPt have been demonstrated, reporting such effects in ML has been challenging, mainly due to difficulties in achieving therapeutic temperatures and effectively encapsulating MNPs.

Magnetosomes are intracellular structures present in all magnetostatic bacteria (Figure 3.2 a), consisting of an iron inorganic magnetic core surrounded by an organic coating (Figure 3.2 b). The type of iron oxide and the composition of the magnetosome membrane will be defined by the bacteria and their environment. There are different types of magnetosome membrane, primarily composed of a bi-lipidic membrane with proteins. Through the biomineralization process, magnetosomes are synthesized from Fe^{3+} into single domain magnetic particles with defined shape and size. These systems are characterized by particles with a narrow size distribution that interact to form chain-like arrangements. Even though the reasons why magnetostatic bacteria choose to form chains are still unknown, it has been observed that magnetosome membrane plays a crucial role in stabilizing these structures.

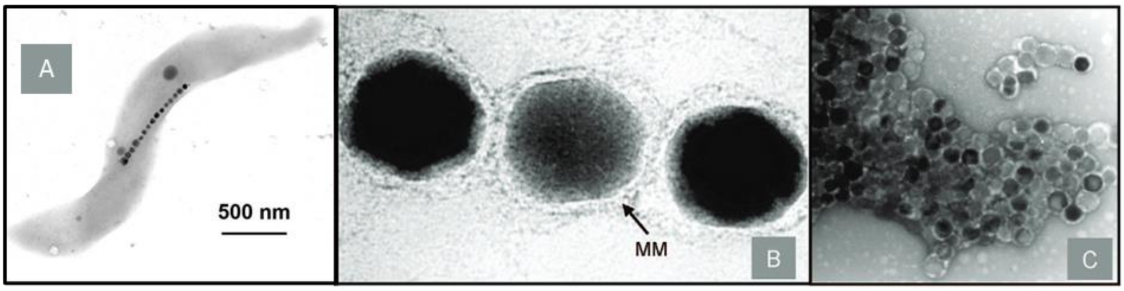

Figure 3.2. A) TEM image of Magnetospirillum gryphiswaldense, revealing the chain of magnetosomes (Extracted from Ref. [66]). B) The magnetosomes membrane (MM) clearly encloses each single MNPs, establishing a gap between them. C) A treatment with SDS to isolated magnetosomes that dissolves the MM yields remarkable clustering of the naked magnetite crystals. (Extracted from Ref [67])

ML are promising systems for nanotechnology with potential applications in magnetic separation, magnetic hyperthermia, magnetic resonance image contrast agents, microtumor detection, drug release and much more. Exploiting the inherent biocompatibility and merging the nanocarrier structure of magnetoliposomes with the strong particle interactions in magnetosomes, we propose the production of ***synthetic magnetosomes*** (LN). This synthetic system possesses distinctive magnetic properties, which will be discussed in Chapter 4, making it an ideal candidate for use as a drug carrier with a thermal response in combined CT and MFH.

This chapter describes and discusses the synthesis process and physicochemical characterization of cisPt-loaded synthetic magnetosomes. We cover the entire process from the synthesis of MNPs optimized for MFH, the synthesis of liposomes (LB), the cisPt-loaded liposomes (LC), the magnetosomes (LN) and ultimately the cisPt-loaded magnetosomes (LNC). The characterization process includes the physicochemical, morphological, compositional, and magnetic properties of all the different nanosystems produced, along with a comparative analysis of these properties where applicable.

3.2. MNPs: Structural and physicochemical characterization

Since our ultimate goal of a combined therapy requires the magnetosomes as efficient heating agents, the MNPs (as the magnetically responsive element of the magnetosomes) were designed for optimal heating efficiency *driven by the magnetosome arrangement*. With this aim, the MNPs were not designed for maximum heating capacity in the colloidal state, but under the magnetically blocked state, as it originated by intra-dipolar magnetic interactions in the magnetosomes. On one hand, the inclusion of MNPs into LN imposed some restrictions on their maximum size because particles larger than ≈20 nm cannot be accommodated into a ≈200 nm vesicles in enough number to be effective. On the other hand, it is well known that MNP size is a critical parameter to optimize heating efficacy, for instance, pure Fe_3O_4 MNPs will show an optimal size value for heating around the 25-35 nm [68, 69], making these values not suitable for our magnetosomes. Therefore, we decided to achieve a more suitable size of ≈ 15 nm optimizing the power absorption by tunning their magnetic anisotropy through doping with a nonmagnetic ion like Zn^{2+}. This strategy was based on the previous experience in our group showing that lowering the magnetic anisotropy of small MNPs also maximizes the Néel relaxation contribution to the value of SLP (specific loss power), a desirable property if LN are to be used in vitro. To this goal, a series of $Zn_xFe_{3-x}O_4$ MNPS was analyzed, and the final composition with maximum SLP was finally selected to fabricate the LN. The zinc-doped magnetite particles were synthesized by the thermal decomposition method of acetylacetonates in presence of surfactants, such as oleic acid and oleamide, detailed in chapter 2.

To search for optimal size and composition, a series of hydrophobic, oleic acid-coated MNPs were synthesized varying the molar concentration of acetylacetonates Zn and Fe, for a nominal concentration $Zn_xFe_{3-x}O_4$ whit $0{,}1 < x < 0{,}5$. TEM images at low resolution (Figure 3.3) showed a predominant rounded morphology of the MNPs. The histograms obtained by counting >600 particles and fitting the data with a gaussian distribution, provided the mean value and the standard deviation. The resulting values were $11 \leq\ d \leq\ 15\, nm$ and $2\ \leq \sigma \leq 5\, nm$, see Figure 3.3. The smaller particles, x=04, and 0,5, are the ones that exhibit a slower second heating ramp, from 100°C to 200°C (See chapter 2). During this interval, the nucleation of the particles takes place, a crucial stage that will determine the size and deviation of the MNPs [70, 71].

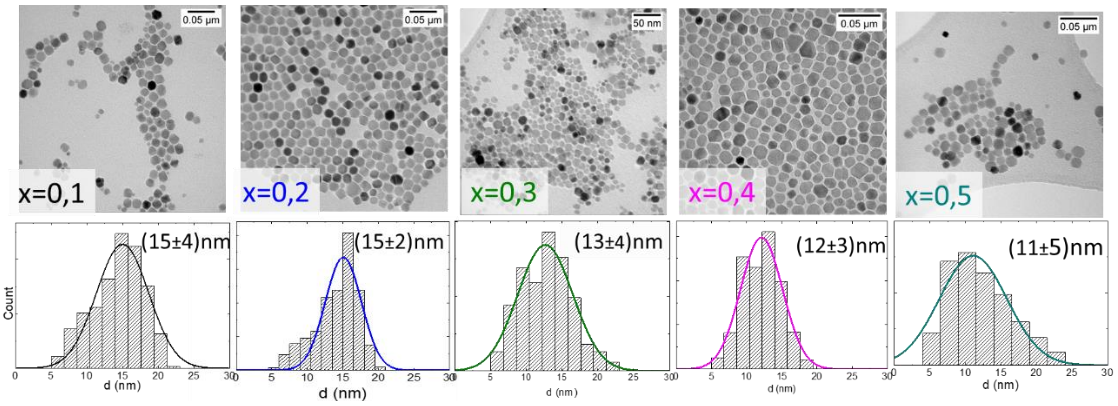

Figure 3.3. TEM images of the $Zn_xFe_{3-x}O_4$ MNPs, and the corresponding size histogram (bottom panel) with their Gaussian distribution.

High-resolution TEM (HRTEM) images (Figure 3.4) revealed a high crystallinity in all samples. Fast Fourier Transform (FFT) analysis of a group of particles produces a diffraction pattern with well-defined concentric rings. Using the ImageJ software, the radial distance of these rings was measured. The Zn-MNPs series exhibits the same spinel structure and can be indexed to the Fd3m space group. This indicates that the MNPs have crystallized in an iron oxide-based spinel structure. The spinel structure corresponds to the ferrites MFe_2O_4 group, where M represents a 3d transition metal, described in chapter 1.

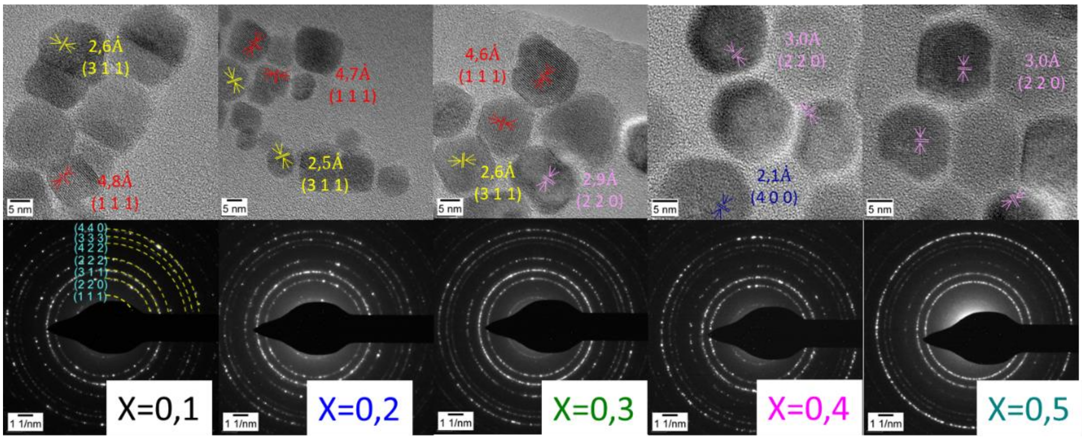

Figure 3.4. HR-TEM image (upper row) with the selected regions for the corresponding FFT analysis. The crystallographic Miller indexes (bottom panel) of MNPs $Zn_xFe_{3-x}O_4$ are indicated.

X-Ray diffraction (XRD) analysis of the powder samples, as shown in Figure 3.5, confirmed the observations made in the HR-TEM and FFT analysis. The positions and relative intensities of the peaks indicate that the sample corresponds to a cubic spinel phase, consistent with the standard pattern of $Fe_{2.897}O_4$ (X'pert analytical reference: 01-086-1343). For samples x=0,1 and 0,4, a small peak at 75° was observed, suggesting a minor amount of a second phase. According to the database, this peak is associated with the $ZnFe_2O_4$ spectrum (00-001-1108), but further information would be needed to confirm this phase.

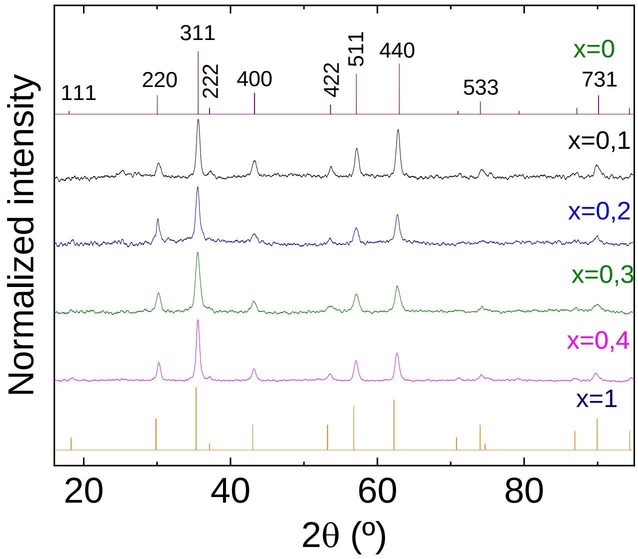

Figure 3.5. XRD patterns of powder samples (MNPs $Zn_xFe_{3-x}O_4$) together with the standard pattern $Fe_{2,897}O_4$(x=0) (01-086-1343) and $ZnFe_2O_4$ (x=1) (00-001-1108).

The crystallite size of the MNPs was determined from the analysis of the full width at half maximum (FWHM) of the main X-ray powder reflections, using the Scherrer formula. The FWHM values were extracted by fitting a Gaussian function to the peaks. The results showed that across all the series, the crystallite sizes (Table 3.1) exceeded the corresponding values obtained from TEM analysis. These differences are usually due to additional broadening of the peaks from crystal strain and/or the inherent instrumental broadening of the diffractometer, independent of the samples. The lattice parameters found for the Zn-MNPs series also in Table 3.1, were found systematically smaller than the corresponding lattice parameter of Fe_3O_4 (a=

0,841 nm), similarly to previous reports on thin films of $Zn_xFe_{3-x}O_4$ [72]. The decrease of the lattice parameter in $Zn_xFe_{3-x}O_4$ compared to bulk Fe_3O_4 (x=0; a = 0,841 nm) is related to ionic sizes and substitution preferences in the crystal structure. In the spinel structure of Fe_3O_4, replacing Fe^{2+} ions with the smaller Zn^{2+} causes the overall lattice to contract. The preference of Zn^{2+} ions for the tetrahedral A sites in the spinel structure (instead of B sites where Fe^{3+} has smaller ionic radius) therefore make the final cation distribution to further contribute to lattice contraction.

The stoichiometric composition of the MNPs was determined by Energy Dispersive X-ray Spectroscopy (EDS) in a Scanning Electron Microscopy (SEM) microscope. The electron beam has a diameter <100 nm and the X-rays are emitted by the sample from a depth of 1-3 µm[73], therefore, this study provides volumetric information of the sample. The presence of Fe and Zn was corroborated by identifying the peaks K_α=6,398 keV and L_α=0,705keV for iron and K_α=8.630 keV and L_α=1.012 keV for zinc (see Table 3.1). In all samples, it was found that the Zn concentration was smaller than the nominal one. A maximum Zn substitution of x=0,24 was observed for the three samples with the highest nominal Zn amount. This may indicate the maximum concentration of Zn that the particles can accept using the thermal decomposition method.

Table 3.1. Table of Average Size Values (<D>) and lattice parameter (a) for $Zn_xFe_{3-x}O_4$ MNPs as determined by TEM and XRD analysis. Also, the atomic compositions of $Zn_xFe_{3-x}O_4$ MNPs extracted from EDS, ICP, and XPS analysis, are tabulated.

$Zn_xFe_{3-x}O_4$	$<D>_{TEM}$	$<D>_{XRD}$	a	Composition		
x	(nm)	(nm)	(nm)	EDS	ICP	XPS
0,1	15±4	18±4	0,8358(3)	$Zn_{0,10}Fe_{2,90}O_4$	Fe_3O_4	$Zn_{0,54}Fe_{2,46}O_4$
0,2	15±2	17±2	0,8374(6)	$Zn_{0,14}Fe_{2,86}O_4$	$Zn_{0,11}Fe_{2,89}O_4$	$Zn_{0,66}Fe_{2,34}O_4$
0,3	13±4	16±3	0,8368(6)	$Zn_{0,23}Fe_{2,77}O_4$	$Zn_{0,18}Fe_{2,82}O_4$	$Zn_{0,63}Fe_{2,37}O_4$
0,4	12±3	17±5	0,8370(9)	$Zn_{0,24}Fe_{2,76}O_4$	$Zn_{0,28}Fe_{2,72}O_4$	$Zn_{0,84}Fe_{2,16}O_4$
0,5	11±5	-	-	$Zn_{0,24}Fe_{2,76}O_4$	$Zn_{0,27}Fe_{2,73}O_4$	$Zn_{0,93}Fe_{2,07}O_4$

The concentrations of Fe and Zn in the series of MNPs were also measured through ICP-OES (Inductively Coupled Plasma - Optical Emission Spectrophotometer), and the results are summarized in Table 3.1. For sample x=0,1 the Zn concentration was below the detection limit of this technique. For $0.2 < x < 0.5$ samples, the values were very close to the corresponding data from EDS, and systematically lower than the nominal values. This Zn deficiency in doped Fe_3O_4 MNPs has been reported for other samples obtained by similar thermal decomposition synthesis route than used in this thesis, while for samples obtained through co-precipitation routes this has not been reported.[74]

We used X-Ray photoelectron spectroscopy (XPS) analysis to assess the surface chemical composition and to analyze the oxidation state of the constituent elements. The XPS spectra of Zn-MNPs series, within the energy range 0-1200 eV (Figure 3.6) confirmed the presence of C, O, Fe and Zn through the corresponding peaks at 284,9eV, 529,9 eV, 710,5 eV and 1020,9 respectively. The binding energy scale was calibrated using the C-C peak at 284,9eV. The stoichiometric quantification of the samples was carried out with the full spectrum (Figure 3.6) and the HR spectra of the samples the results were compiled Table 3.2.

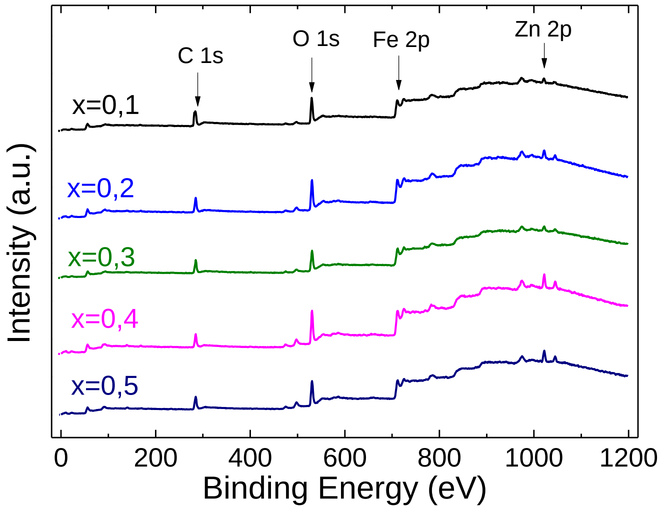

Figure 3.6. Full energy range XPS spectra of Zn$_x$Fe$_{3-x}$O$_4$ MNPs series, highlighting the component peaks from carbon (C), Oxygen (O), Iron (Fe), and Zinc (Zn).

In all the samples, the two main peaks 710,80eV and 724,50eV corresponding to Fe^{3+} at the 2p $_{3/2}$(L3) and 2p $_{1/2}$ (L2) thresholds were observed [75]. The site and state of oxidation of Fe, were obtained by following the evolution of 709,4eV, 710,5eV and 712,5eV peaks corresponding to Fe^{2+} (2p$_{3/2}$) and Fe^{3+} (2p$_{3/2}$) of the octahedral site and Fe^{3+}(2p$_{1/2}$) from the tetrahedral site [76] [77], the results are grouped in Table 3.2. From the analysis of the peak intensity in Figure 3.7, we observe a decreasing in the Fe^{2+}(2p$_{3/2}$) intensity peak and an increase of Zn contribution, except for x=0,1 sample. In the tetrahedral site Fe^{3+} decreases with the increase in Zn concentration, this result agrees with the fact that Zn^{2+} ions occupy the tetrahedral sites. In the samples x=0,4 and 0,5 the presence of two satellites was observed, one at 731,6eV corresponding to Fe2p$_{1/2}$ and another at 716eV and 718eV, for each sample, corresponding to Fe 2p$_{3/2}$ [76] [75] [78]. The absence of satellites was observed in magnetite. The ratio 3Fe^{2+}/(Fe^{2+}+Fe^{3+}) was calculated from the adjustment of the oxidation states for the samples, results summarized in Table 3.2, for Fe$_3$O$_4$, this ratio is approximately 1. Unlike what is observed in the Zn$_x$Fe$_{3-x}$O$_4$ MNPs series, where the ratio is always less than 1, with a maximum value of 0,61 for x=0,2.

Table 3.2. XPS spectral fitting parameter for Fe 2p for Zn$_x$Fe$_{3-x}$O$_4$ MNPs series.

Zn$_x$Fe$_{3-x}$O$_4$ x	Fe 2p 3/2 (eV)	Fe 2p 1/2 (eV)	ΔE (eV)	Fe^{2+} octa (%)	Fe^{3+} octa (%)	Fe^{3+} tetra (%)	Fe 2p$_{1/2}$ (%)	Sat. Fe^{3+} 2p$_{3/2}$	Sat. Fe^{3+} 2p $_{1/2}$	3Fe^{2+}/ (Fe^{2+}+Fe^{3+})
0,1	711,20	724,50	13,30	0,21	36,15	26,24	37,40	-	-	0,010
0,2	710,70	724,50	13,80	12,35	22,59	25,67	39,38	-	-	0,611
0,3	710,80	724,50	13,70	9,16	23,15	26,82	40,87	-	-	0,465
0,4	710,80	724,50	13,70	3,18	30,38	12,18	27,20	9,69	9,69	0,208
0,5	710,80	724,40	13,60	4,14	13,61	15,36	23,42	14,45	29,03	0,375

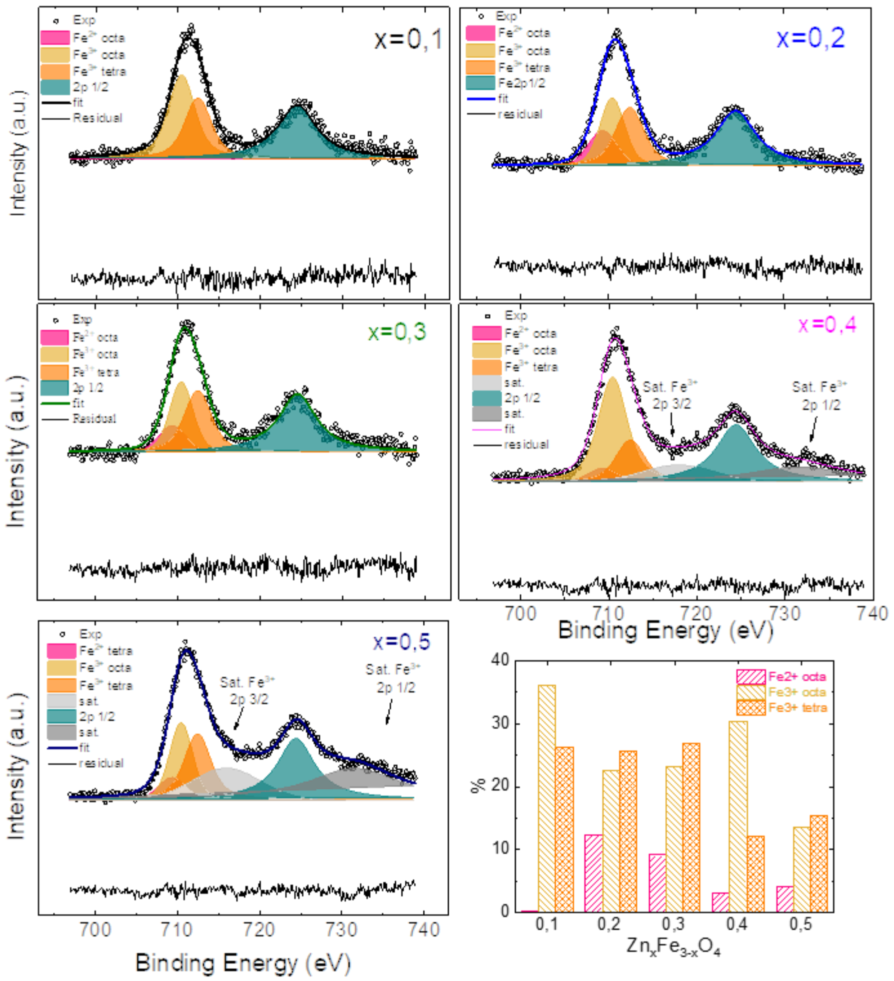

Figure 3.7. XPS spectra in the Fe 2p threshold region for $Zn_xFe_{3-x}O_4$ MNPs series (after background subtraction). Open circles correspond to experimental data, and solid lines in color are the fitted curves. The black lines at the bottom of each fit indicate the residual $= I_{observed} - I_{fitted}$.

The 2p region of Zn^{2+} showed the presence of two peaks at 1022eV and 1045eV, corresponding to the Zn $2p_{3/2}$ and Zn $2p_{1/2}$ states [79] [80]. In the samples x=0,1, 0,2 and 0,3 a splitting is observed in the spectrum of Zn $2p_{3/2}$, according to bibliography this indicates that the Zn is in the metallic state Zn (0) [79] [81]. In summary, for all the $ZnxFe_{3-x}O_4$ MNPs series, the particles present an inhomogeneous composition, with a Zn-rich surface and different oxidation states. These inhomogeneities within the MNP's compositions have an impact on the magnetic properties of the particle, especially on the effective magnetic anisotropy [82], as will be discussed in more detail in Chapter 4.

The magnetic response as function of an applied field was studied on the series $Zn_xFe_{3-x}O_4$ MNPs by vibrating sample magnetometer (VSM) (Figure 3.8). With low values of coercive field (H_c) and magnetic remanence (M_R) (summarized in Table 3.3), the MNPs present a superparamagnetic behavior at room temperature. Saturation magnetization (M_S) values, summarized in Table 3.3, present a maximum of 76 Am^2/kg, corresponding to the smallest particle (x=0,5), and a minimum value of 34 Am^2/kg for the largest particle (x=0,2). The lower values than the typical ones for bulk Fe_3O_4 (M_s=90 - 95Am^2/kg), are consistent with the substitution of Fe ions with nonmagnetic Zn, and has been previously reported in MNPs of similar composition and size [83, 84]. The presence of oleic acid, a diamagnetic coating, may also contribute to the observed decrease in M_s, as observed by Guardia et al. [85]. Additionally, interactions between spins in the tetragonal and octahedral sites within the spinel configuration could be a contributing factor. Zn ferrites exhibit a typical structure, with Zn^{2+} ions of zero moment occupying the tetrahedral sites. The strongest interactions occur between AB, where spins are oriented oppositely, canceling out their contribution. A higher Zn concentration at site A implies fewer moments canceling out at site B, thereby increasing M_S. XPS analysis, as depicted in Figure 3.6, reveals that for samples x=0,2 and 0,3, the contributions of Fe^{3+} at site A and B are approximately equal, in good agreement with the low M_S values obtained in the samples [86].

Table 3.3. Saturation magnetization M_s (Am^2/kg), Remanent magnetization M_R (Am^2/kg), and Coercive field H_C (kA/m)) for the $Zn_xFe_{3-x}O_4$ MNPs series at room temperature. Also shown in the last columns are the SLP values in W/g obtained under H_0 = 24 kA/m and f = 570 kHz in toluene and paraffin.

$Zn_xFe_{3-x}O_4$	M_S	M_R	H_C	SLP (W/g)	
x	(Am^2/kg)	(Am^2/kg)	(kA/m)	Toluene	Paraffin
0,1	57	7,7	4,1	568 ± 73	126 ± 28
0,2	34	4,8	5,0	244 ± 73	247 ± 28
0,3	50	5,3	3,3	411 ± 120	89 ± 8
0,4	61	8,0	4,7	300 ± 97	84 ± 8
0,5	76	8,8	4,2	300 ± 120	105 ± 7

As mentioned in the introduction, these series of MNPs were synthesized to explore the optimal Zn composition that provided maximum heating efficiency (i.e., maximum SLP, see below) for particle sizes of ≈15 nm, a limit imposed by their use in the subsequent production of LN. For single-domain MNPs of ≈15 nm as the ones described in this chapter, there are two main mechanisms responsible for the heat dissipation: 1) Brownian relaxation, where the particle rotates to orient itself with the applied external magnetic field; and 2) Néel relaxation, involving the rotation of the magnetic moment within the MNPs (see chapters 1 and 4).

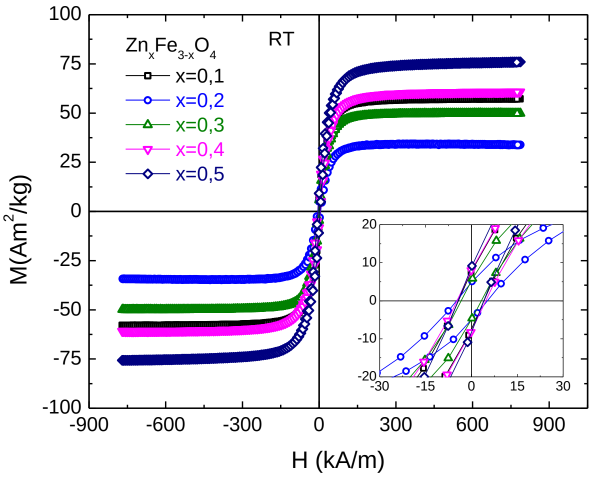

Figure 3.8. M(H) curves at room temperature (RT) of the $Zn_xFe_{3-x}O_4$ MNPs series. Inset: a magnification of the low-field region to observe the constant H_C values.

The Brownian relaxation is influenced by the physicochemical properties, predominantly the viscosity of the liquid carrier, in which the particle is immersed. The Brownian contribution in the Zn-MNPs was evaluated by measuring the SLP in a low viscosity carrier (Toluene; viscosity $\eta = 0{,}63\ mPa.s$ at T=15°C) and a solid matrix at room temperature (paraffin; viscosity $\eta >$

$45\ mPa.s$ at T=15°C). Figure 3.9 and Table 3.3 summarize the SLP measurements data (H_0=24 kA/m; *f*=570kHz). As expected, the SLP values in paraffin were lower than in liquid toluene due to the blocking of the Brown relaxation contribution to the dissipation, with decrements in SLP of 78% for x=0,1 and 0,3, 72% for x=0,4 and 65% for x=0,5. Sample $Zn_{0,2}Fe_{2,8}O_4$ showed constant SLP values maintained in both carriers (244±73 W/g in toluene and 247±28 W/g in paraffin). A decrease in data dispersion and better reproducibility of SLP values was observed for experiments performed on paraffin. We assign this better reproducibility to the fact that the formation of magnetic chains, aggregation and/or precipitation processes, which produce changes in power absorption, does not occur in the solid matrix. Since the final goal in this work require that the LN can efficiently perform *in vitro* experiments*,* the MNPs should maintain their SLP values as heating agents. This required their *absorption power to be mainly due to Néel relaxation*. ***From the above results we decided to select the $Zn_{0,2}Fe_{2,8}O_4$ MNPs, that retained their SLP values in solid matrix, and use them to produce the LN.***

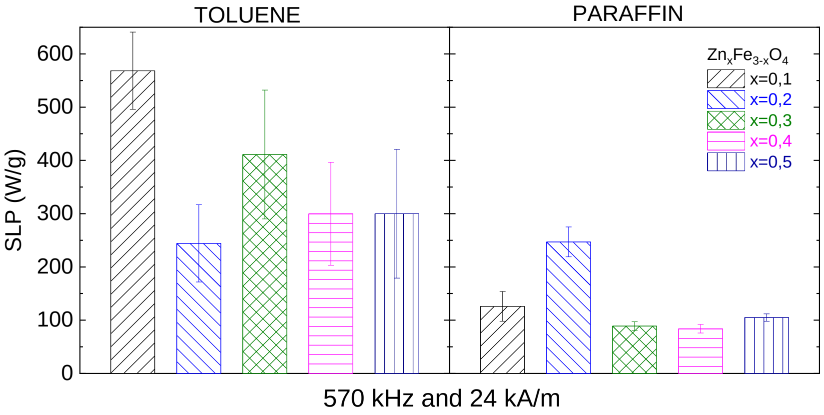

Figure 3.9. SLP values (W/g) for Zn-MNPs series dispersed in toluene (left) and paraffin (right), in presence of an alternate magnetic field of 24kA/m and 570kHz.

For *in vitro* experiments, the MNPs required to be translated to a biocompatible, water based colloidal formulation. A ligand exchange method was implemented to replace the oleic acid (OA) by a sodium citrate (SC) coating. The entire procedure was detailed in Chapter 2. In this way, and taking advantage of the amphiphilic nature of liposomes, we were able to assess the best protocol for encapsulating either hydrophobic or hydrophilic MNPs into the liposomes.

Fourier Transform InfraRed (FT-IR) technique was used to confirm the presence of the coating on MNPs. FTIR spectrum of OA-MNPs present the characteristic peaks of OA (Figure 3.10 a). In both spectra the characteristic bands of the aliphatic compounds (2852 cm^{-1} and 2924cm^{-1}) corresponding to the symmetric and antisymmetric stretching of the HC-CH carbon chain (Figure 3.10 d) are detected. The 3005 cm^{-1} peak corresponding to the alkene group (C=C), is observed shifted to 3028 cm^{-1}, in the case of OA-MNPs (Figure 3.10d). The intense peak at 1707 cm^{-1}, present in the OA corresponding to the carboxylic acid, decreases and moves to 1605 cm^{-1}, in the case of the MNPs, now corresponding to the COO-Fe group (Figure 3.10 c). At low wavenumbers, 723 cm^{-1}, the presence of MNPs increases the signal corresponding to the rocking of methylene $-(CH_2)_n$, n>3. The band at 937cm^{-1} of the C=C group decreases and shifted to 893 cm^{-1} for the case of the MNPs (Figure 3.10 b). For all this, we can confirm that the MNPs are covered by OA, possibly joining through the carboxyl group, and breaking the C=C double bond. [87] [88]

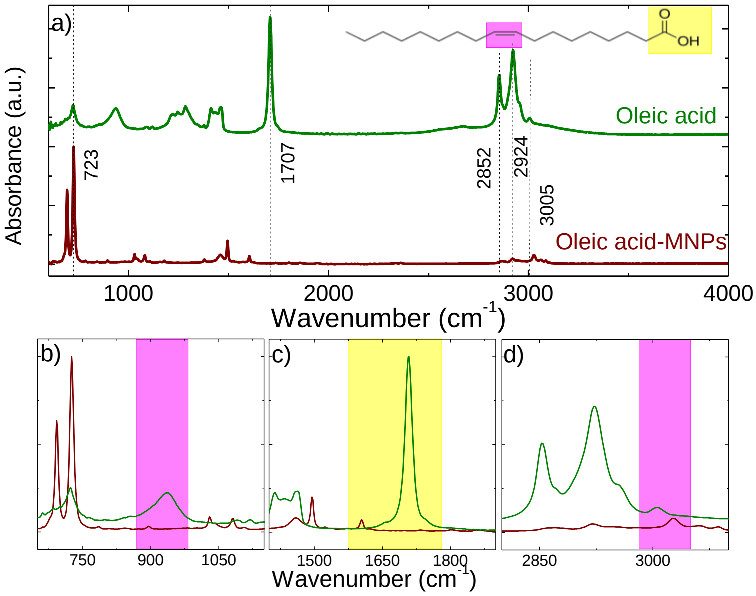

Figure 3.10. FT-IR spectrum of OA (green) and OA-MNPs (brown). Lower panels: expanded peak regions for b) methylene rocking $(CH_2)_n$, n>3 and C=C bonds, c) COOH and COO-Fe bond, and d) HC-CH stretching and C=C bonds.

By comparing the FTIR spectra of sodium citrate (SC) and SC-MNPs(Figure 3.11), the absorption bands, 1389 cm^{-1} and 1581 cm^{-1}, corresponding to the carboxylate group due to its symmetric and asymmetric stretching respectively, are observed in both spectra, broadening for the presence of MNPs (Figure 3.11 c). In addition, the beginning of the characteristic 550 cm^{-1} peak corresponding to the Fe-O group of MNPs can be observed. In this way, the FTIR analysis suggest that the functionalization explained in chapter 2 for the exchange of coatings from OA to SC was successful. Additionally, the carboxyl group of SC is potentially covalently tethered to the surface of the MNPs, establishing a hydrophilic character for the MNPs through this linkage to the Fe element [89] [90].

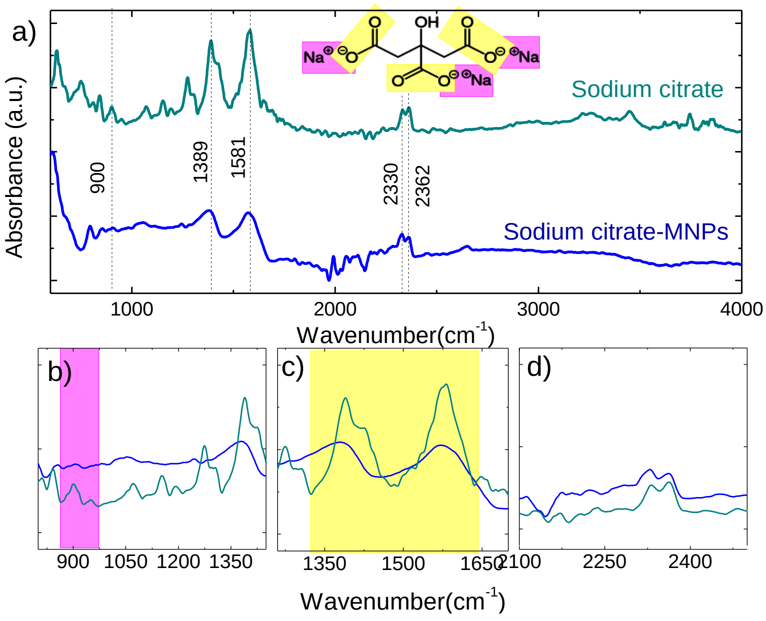

Figure 3.11. FT-IR spectrum of SC (turquoise) and SC-MNPs (blue). Lower panels: expanded peak regions for b) Na^+ion, c) Carboxylate group, and d) doble bound region.

Thermogravimetric analysis (TGA) was performed on dried powder of coated MNPs to confirm and estimate the mass of organic material attached to MNPs surface. Figure 3.12 shows the percentage weight loss as a function of temperature and its first derivative for the a) OA-MNPs and b) SC-MNPs samples. In both cases, a decrease in weight loss rate was observed when the temperature is raised to 200°C, at 158°C with 5,5% of weight loss in the case of OA-MNPs and at 140°C with 2% of weight loss for SC-MNPs, probably due to residual water evaporation of the desorption of water molecules. Also, for both coatings, an increase in weight is detected at high temperatures, 656°C for OA and 616°C for SC, which was attributed to the oxidation of magnetite Fe_3O_4 to maghemite Ɣ-Fe_2O_3 or hematite α-Fe_2O_3.

Although the thermal decomposition of pure OA is known to occur between 200 and 300 °C [91], two derivative peaks in the TGA curves in our samples (Figure 3.12 a), probably due to the decomposition of OA bounded with different strength to the MNPs surface as previously reported[92]. The first peak at 246 °C with the percentage weight loss of 4,7%, refers to the weakly bounded OA-MNPs, corresponding to the Van der Waals type bond between the hydroxyl of the hydrocarbon chain of OA and the surface of MNPs. The second peak at 371 °C, percentage weight loss of 6,7%, indicating the decomposition of the covalent bond (C=C) with the surface of the particle. The coexistence of weakly and strongly bounded OA on the MNPs surface was also supported by FT-IR analysis.

In the case of SC-MNP, three regions were distinguished for weight loss in the temperature ranges of 30–180 °C, 180–455 °C and 455–600 °C as presented in Figure 3.12 b. The second stage, with a percentage weight loss of 6,7%, could be associated with the combustion or decomposition of the citrate absorbed on the particle surface[93, 94]. Comparing the TGA results, we can deduce that the OA coverage (15%) was thicker than the SC coverage (10%).

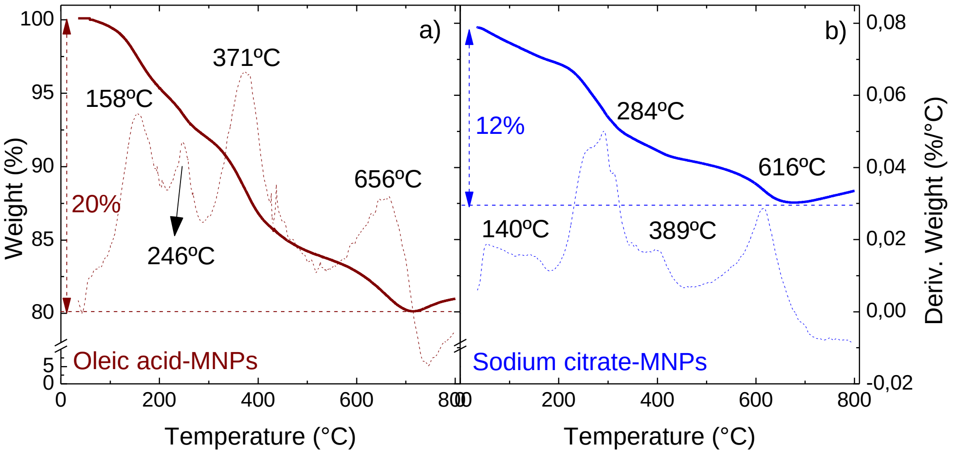

Figure 3.12. TGA rate for a) OA-MNPs (left - brown) and b) SC-MNPs (right - blue), and derivative weight (%/°C) in function of temperature (°C) (dashed line).

3.3. Liposomes and magnetosomes: synthesis and characterization

Along this thesis, different liposomes (LB) synthesis methods have been applied to produce synthetic magnetosomes (LN). These LN were used as cisPt carriers, in the preparation of cisPt-loaded thermosensitive liposomes (LC) and LNC (liposomes+ MNPs+ cisPt). Different factors influenced the synthesis method election such as: purpose, the type of drug that we want to encapsulate, the size of the liposomes, among others. In this thesis we study: the lipid rehydration method, solvent injection, and the reverse phase evaporation (RPE) method, Table 3.4 summarizes the advantages and disadvantages of each method.

Table 3.4. Advantages and disadvantages of the different liposome preparation methods most commonly reported, information compiled from Maherani et al. [95].

Method	Advantage	Disadvantage
Film hydration	Simple process	Use of organic solvent, production of large particles with no control on size, poor encapsulation efficiencies of hydrophilic materials, time consuming, sterilization issue
Solvent injection	Simple process, requires less equipment	Trace of organic solvent as residue, time consuming, sterilization issue
Reverse Phase evaporation (RPE)	Suitable encapsulation efficiency	Use of large amount of organic solvent, time consuming, sterilization issue

With the three methods, liposomes loaded with water-soluble compounds are easily obtained, but they do not present the same behavior when working with MNPs. For the three methods we make probes changing the mixtures and compositions of lipids, testing with MNPs with OA and SC coating. **Good results for the synthesis of LN were obtained by the reverse phase evaporation method, with the lipid composition summarized in Table 3.5, using the MNPs coated with sodium citrate.** The lipid composition to produce the nanocarriers LB, LN, LC and LNC, was selected for different reasons. Ionic molecules such as DODAB ensure the physical stability of the formulation by preventing fusion and aggregates between liposomes. Polymer-loaded liposomes such as PEG, increase biological stability by reducing interactions with blood proteins. Cholesterol, with its easy-to-fit structure, provides stability and rigidity to the bilipid membrane. The step-by-step synthesis procedure was detailed in chapter 2. In Table 3.5 we also report the order/disorder mean transition temperature (T_m), pH, molecular size and ζ potential.

Table 3.5. Lipids characteristic: Percentage (%) of lipid used in LB and LN synthesis, mean transition temperature (Tm)(°C), pH and ζ Potential for DPPC (1,2-dipalmitoyl-sn-glycero-3-phosphocholine), DODAB (didodecyldimethylammonium bromide), CHOL (Cholesterol) and PEG (1,2-distearoyl-sn-glycero-3-phosphoethanolamine-N-[methoxy(polyethylene glycol)-2000] (ammonium salt)).

Name	Type	Percentage (%)	Size (Da)	T_m(°C)	pH	ζ Pot
DPPC	phospholipid	45	734	41.3	8.0	4±16
DODAB	surfactant	20	630	43.0	8.6	1±11
CHOL	steroid	30	386	-	8.1	29±17
PEG	Phospholipid	5	2805	-	5.8	0±6

Cryo-TEM is an ideal technique to observe liposomes, in their original state since the vesicles are not dehydrated. Cryo-TEM images of LB, Figure 3.13 (a, c, d) show unilamellar spherical vesicles with a gaussian distribution (Figure 3.13 b) with an average diameter of (166±60) nm. This value coincides with the value obtained by dynamic light scattering (DLS) at room temperature for LB dispersed in water of (165±20) nm. Expected value since the extrusion of the LB was carried out with filters of 100 nm pore size. HRTEM images, Figure 3.13, show a defined bilipid membrane. We performed a statistical analysis to assess the thickness of the observed lipidic membranes (Figure 3.13 e). Using a graphics software (ImageJ), we analyze the grays scale profile for a line crossing the bilipid membrane. Figure 3.13 f, show a typical profile where the two peaks on the border of the gray scale valley represent the limits of the bilipidic membrane, an average value of (8,1±0,3) nm, consistent with (but slightly above than) the values found in the literature of 4,5 nm – 7,1 nm. [96, 97].

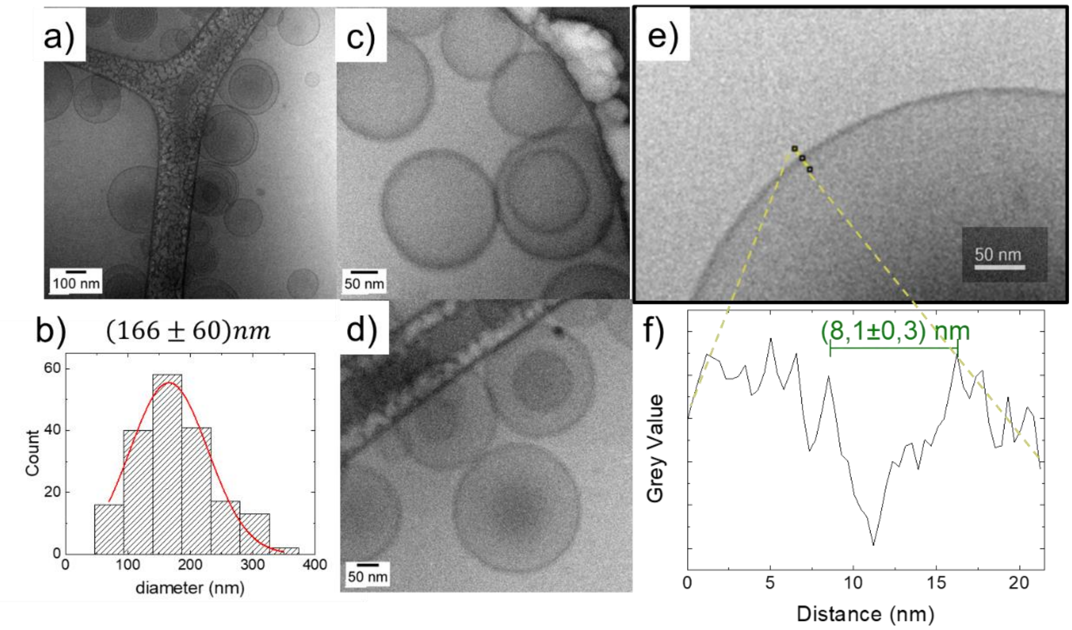

Figure 3.13. a) Cryo-TEM image of liposomes (LB). b) LB histogram with its respective Gaussian distribution, average size of (166± 60) nm. c) and d) HR cryo-TEM images of LB. e) HR cryo-TEM image of the bilipid membrane of a liposome, with an area marked in yellow where a f) analyzed of the gray scale in the image was performed to know the size of the bilipid membrane (8,1±0,3) nm.

The low-magnification cryo-TEM images (Figure 3.14 a,b,c) of the LN showed a quasi-circular clusters of MNPs as the major population, with coexisting less-stacked smaller cluster particles, while isolated particles were not observed. The histogram showed a Gaussian distribution (Figure 3.14 f) with a mean size <d>= (281±60) nm, which was consistent with the extrusion performed during the last step of the LN system using a filter with a pore size of 200 nm. The extrusion step with this small pore size yielded a great loss of material on the filters, as consequence, it was decided to use a larger pore size (1000 nm). Larger agglomerates of several microns with holes were also appreciated. These formations are reminiscent of the gel-like state during the manufacturing process prior to the collapse of the system in multilamellar vesicles, being possible that during the synthesis process the proximity between the MNPs has played a more important role than the formation of liposomes.

Figure 3.14 presents a selection of the most representative images of LN, include samples in their *as-prepared* state as well as those fixed and embedded in EPON® blocks. Many features could be established but, as a general outcome from the analysis, it was possible to distinguish three types of morphologies:

1. A curly and spiral arrangements of MNPs chains,
2. Ordered packing of particles chains
3. Liposomes without or with very few particles in their hydrophilic cores.

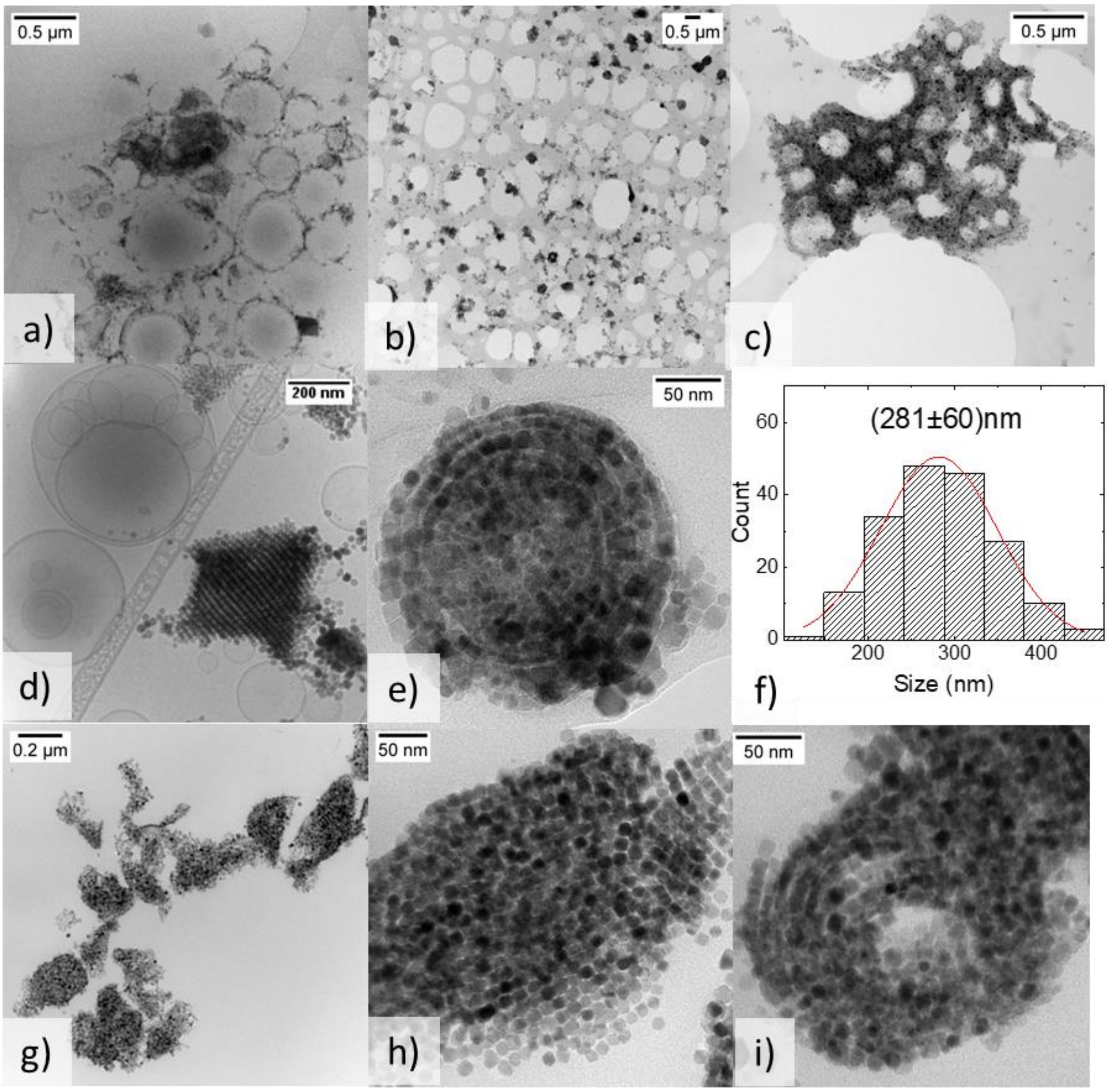

Figure 3.14. Cryo-TEM images of LN: a), b), c) display the system's landscape with spherical LNs and some agglomerations showing holes surrounded by MNPs; d) reveals a grid-like arrangement of MNPs and liposomes without particles; e) shows LNs with a curved arrangement of MNP chains; f) presents a histogram of LN size with Gaussian distribution; g), h), and i) are TEM images of contrasted resin blocks of LN.

Analysis of the images showed a clear separation between each neighboring particle and between each chain of particles (Figure 3.14). Also, an organic layer seems to cover the LN. The discrimination between the organic part and MNPs was difficult to be observed with this technique due to the high contrast of the particles compared to the lipids, and because focusing the electron beam for a long time, damages the integrity of the sample. In order to avoid this problem, the morphology of the LN was also characterized from TEM images using embedded LN on resin blocks contrasted with osmium, uranyl, and lead. TEM images, Figure 3.14 g, h and i, confirm the separation between particles and chains, but the contrast used in the sample was not enough to stain and distinguish the lipid layer. Figure 3.14 i shows the oval formations of spiral arrangements of MNPs. Also, Figure 3.14 h reveals MNPs in a grid's formation by chains of MNPs separated by gaps. In this case, it was possible to observe holes inside the LN. A more detailed study of the shape and structure of the LN will be carried out in sections 3.3.2 and 3.3.3.

FT-IR technique was used to study the composition of the lipidic membrane and to confirm the presence of the different lipids (DPPC, DODAB, cholesterol and PEG) on our samples. The FT-IR spectrum of the powder of lipidic component and LB (Figure 3.16) present the characteristic bands of the aliphatic compounds (2850 cm^{-1} and 2916cm^{-1}) corresponding to the symmetric and antisymmetric stretching of the -C-C- of carbon chain (Figure 3.16 c). In all the spectra, the peaks corresponding to the asymmetric (1483cm^{-1}) and symmetric (1468cm $^{-1}$) bending of the C-C group are also observed, although with differences due to the carbon chain lengths (Figure 3.15). Comparing the spectrum of LB and DPPC, a band is found at 3315 cm^{-1} (3647-3093cm^{-1}) corresponding to the ammonium group ($N^+(CH_3)_3$), with low intensity in LB at 1732 cm^{-1} and 970 cm^{-1} the peaks corresponding to the ester group and the bending of a methyl group, were identified. The two lines at 1057 cm^{-1} and 1049 cm^{-1} band (Figure 3.16 b) corresponding to the P=O stretching mode are absent, and the 848-829 cm^{-1} lines corresponding to asymmetric and symmetric P-O-C stretching, respectively, are modified in the spectrum of LB. These features are consistent with a modification in the hydrophilic head of the LB. It was possible to distinguish in LB, with a low intensity and deformed the DODAB fingerprint, peaks at 891 cm^{-1} and 721 cm^{-1} corresponding to the nitrate and boron ion. The presence of the band at high wavenumbers (3425 cm^{-1}) in the LB is due to the hydroxyl group (-OH) of cholesterol. Finally, comparing the pegylated lipid with the LB we saw with less intensity the peak corresponding to the P-O-C stretching at 841 cm^{-1} and at 1147 cm^{-1} the C-O stretching peak. A double peak at 1564 cm^{-1} and 1603 cm^{-1} present in LB does not coincide with any of the lipids used, this probably may be due to crossing contamination. From this analysis it can be inferred that the four lipids used as reactants are effectively present in the LB membranes.

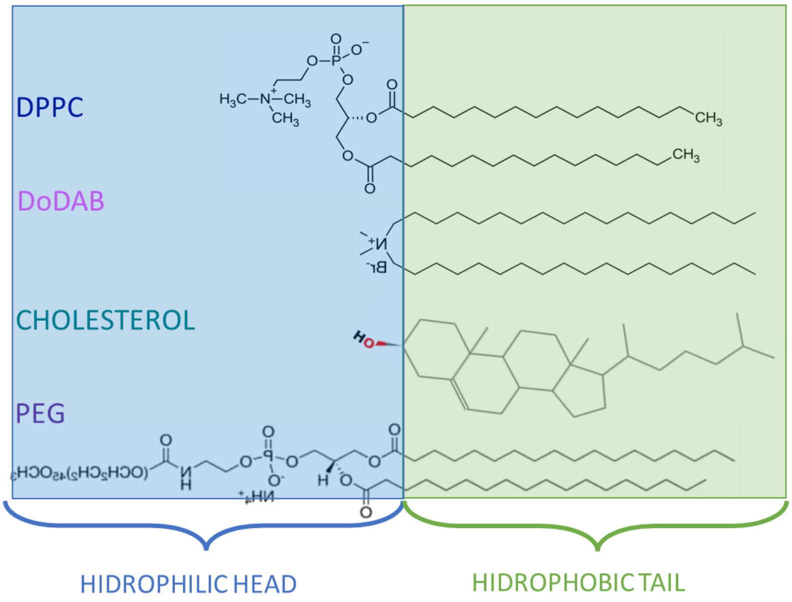

Figure 3.15. Chemical structure of the lipids used in the synthesis of LB, LN, LC and LNC. From up to down: DPPC, DODAB, CHOL and PEG.

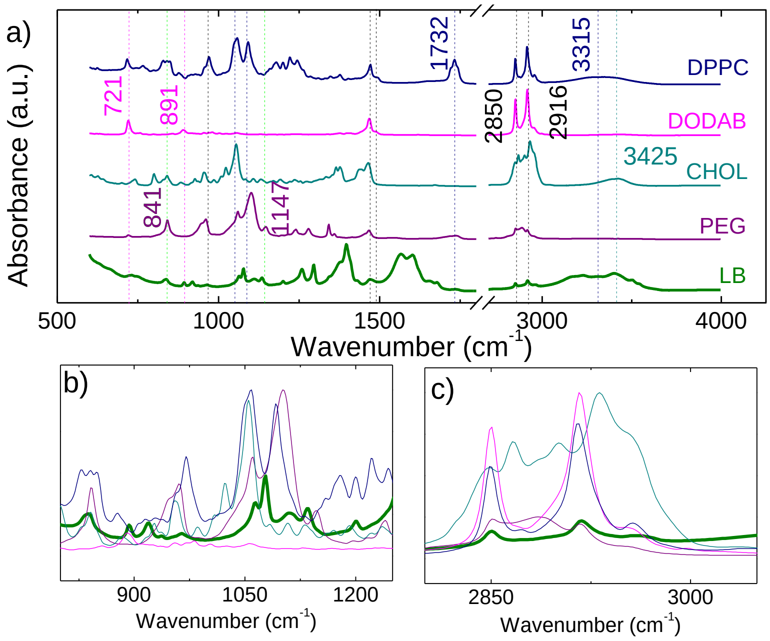

Figure 3.16. FT-IR spectrum of lipids powder: DPPC (navy), DODAB (magenta), Cholesterol (dark cyan), 18:0 PEG 2000(purple) and LB (olive green). Lower panels: expanded peak regions of b) methylene rocking ($(CH_2)_n$, n>3 and C=C bonds, c)- H_2C-CH_2- stretching.

In the case of the LN, the peaks corresponding to the stretching (2850 cm^{-1} and 2916 cm^{-1}) (Figure 3.17 c) and doubling (1483 cm^{-1} and 1468 cm^{-1}) (Figure 3.17 b) of the aliphatic chains -C-C- were also found. At high wavenumbers the band of the ammonium group corresponding to DPPC appears but not that of the OH group in cholesterol. At 1732 cm^{-1}, the peak of the DPPC ester group is weakly present. In the case of the DODAB and the PEG the same behavior is observed as with the LB.

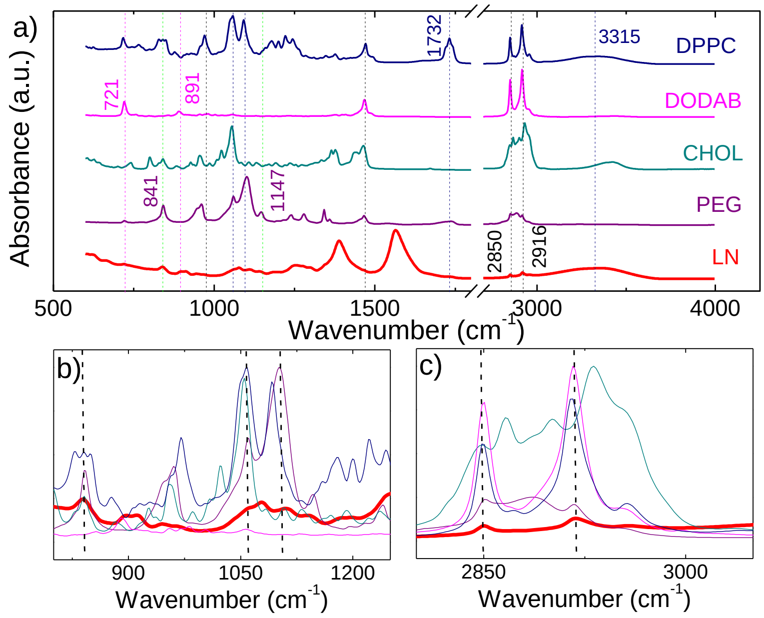

Figure 3.17. FT-IR spectrum of lipids powder: DPPC (navy), DODAB (magenta), Cholesterol (dark cyan), 18:0 PEG 2000(purple) and LN (red). Lower panels: expanded peak region of b) methylene rocking ((CH_2) n, n>3 and C=C bonds, c) -C-C- stretching.

FT-IR spectroscopy also confirmed the presence of cisPt in the LC and LNC (Figure 3.18). Although the mass concentration in the pure cisPt sample was an order of magnitude lower than that of the liposomes, it is possible to detect the peaks 1291 cm^{-1} and 1311 cm^{-1}(Figure 3.18 b), relative to the symmetrical bending of the N-H group and at 3277 cm^{-1} (Figure 3.18 d) the antisymmetric stretching of the N-H group. The use of citrate buffer during the synthesis of LC and LNC to increase the solubility of cisPt, modifies the spectrum by running the peaks [98, 99]. In the LC and LNC spectra it is also possible to detect the most important peaks corresponding to lipids: 2850cm^{-1} and 2916 cm^{-1} C-C stretching, 1062cm^{-1} and 1109 cm^{-1} C-C bending, 721 cm^{-1} corresponding to DODAB, 841 cm^{-1} of the PEG, among others.

In all the spectra (Figure 3.18 c) the presence of the 1389 cm^{-1} and 1581cm^{-1} peaks corresponding to the symmetrical and asymmetrical stretching of the carboxyl group of the sodium citrate used as coating on the MNPs was observed, indicating the presence of MNPs in all liposomes. This means that the systems, LB, and LC, may have been contaminated during the extrusion process, being able to separate them magnetically or by centrifugation.

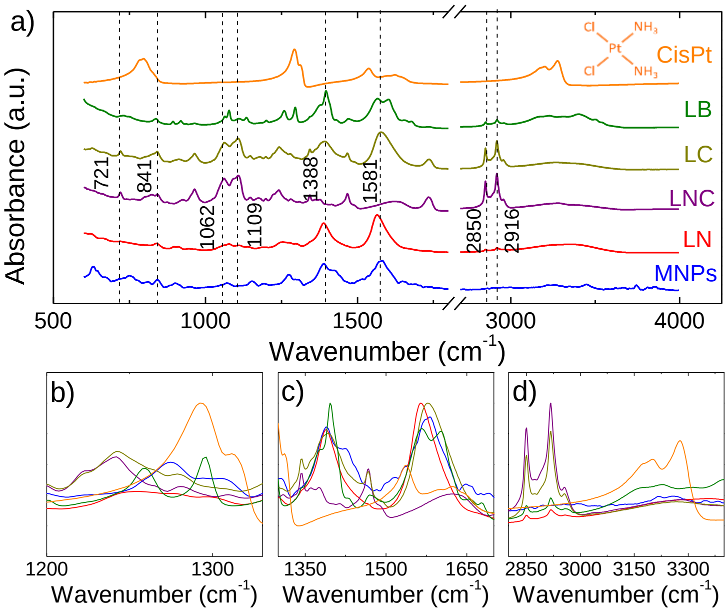

Figure 3.18. FT-IR Spectral Analysis: Powdered CisPt (Orange), LB (Olive Green), LC (Brown), LNC (Purple), LN (Red), and MNPs (Blue). Insets: Detailed Views of Lower Wavenumber Peaks (b), Carboxylate Group Region (c), and -H_2C-CH_2-, N-H Stretching Bands (d).

3.3.1. Temperature effects on the lipidic membranes

Phospholipids are the functional units of liposomes. As amphiphilic entities, they exhibit various forms or polymorphisms that are influenced by factors like concentration, temperature, pH, and the surrounding environment. Modifying any of these elements leads to a structural modification that offer insights into the membrane's fluidity and permeability. At room temperature, the lamellar membrane in the gel phase ($L_{\beta'}$) is characterized by reduced tilt of the carbon chains and the presence of hydrated spaces. When the temperature rises, the system transitions into a liquid crystalline phase (L_α). This reversible transition, called the main order/disorder transition (T_m), can be detected as a peak in differential scanning calorimetry (DSC).[100] In a unilamellar vesicle composed of a single lipid, such as DPPC, there is an intermediate phase known as the pretransition (T_p). During this phase, the system shifts from the $L_{\beta`}$ phase to the rippled gel phase ($P_{\beta`}$). This transition involves relatively smaller energy changes and thus need better sensitivity to be detected experimentally. The movement of the lamella during this phase transition influences the Van der Waals interactions among the hydrocarbon chains.

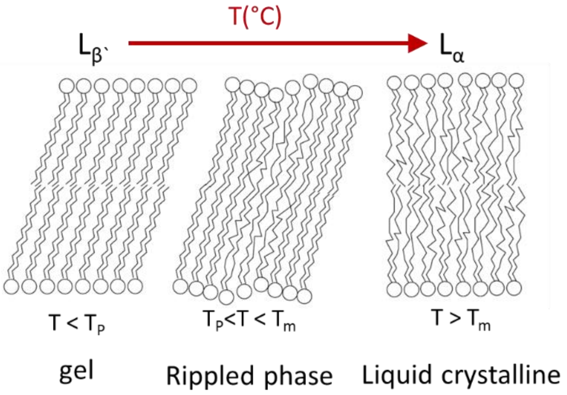

Figure 3.19. Schematic depiction of carbon chain alignment in the bilayer lipid structure across various states during temperature increase, adapted from Demetzos' work [101].

We have undertaken a thorough characterization of the lipid structures in our nanosystems because the effectiveness of our targeted drug delivery depends on how these components react to physical stimuli, such as magnetic fields or heat in our case. Temperature variations can induce transitions in lipid membranes, resulting in a more fluid and permeable state, which in turn influences the drug release process. For this reason, it is important to evaluate whether the inclusion of MNPs and the drug in the LNC samples has modified these inherent properties.

DSC scans of LB and LN, Figure 3.20, confirmed that the presence of the MNPs almost did not vary the main transition T_m, from 52,7°C for LB to 52,9°C in the case of LN. Although the full width at half maximum (FWHM) decreased from 13,1°C in LB to 5,4°C for LN. The sharper peak in the LN could be associated with high cooperative Van der Waals interactions between hydrocarbon chains [101].

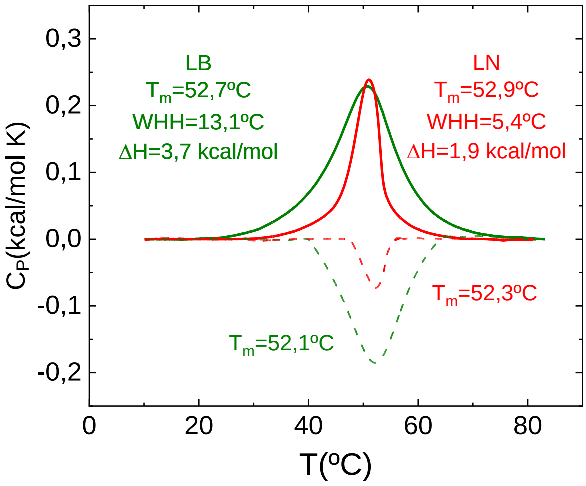

Figure 3.20. Heating (solid lines) and Cooling (dashed lines) DSC Scans for LB (Green) and LN (Red), Displaying Average Transition Temperatures from Lβ` State to Lα.

The cooling curves in the lipid systems demonstrate a reversible behavior, with a temperature reduction of $\Delta T = 0{,}6°C$ observed in both cases. The enthalpy values calculated for LB, 3,7 kcal/mol, are higher than those for LN, 1,9 kcal/mol, indicating a more rigid bilayer in LB compared to LN. The T_m of our bilayer vesicles is higher than for each individual phospholipid, as detailed in Table 3.5. This finding aligns with previous reported observations [18] [16] suggesting that the increase in main temperature relative to the T_m of DPPC phospholipid can be attributed to the presence of carbon chains longer than 16C, like those in DODAB and PEG, which have an 18C chain. Variations in T_m from 41°C to 57°C have been reported in vesicles by altering the DPPC/DODAB phospholipid concentration, with a peak at a 50%:50% DODAB:DPPC ratio. At a 20% DODAB concentration, the T_m was recorded at 46°C, and at 30%, the Tm reached 54°C. These values fall within the temperature range of our LB and LN, which use a 20% DODAB concentration in our studies [48]. This indicates that Tm is influenced by the molecular composition of the lamella.

The study of the role of cholesterol in LB and LN was carried out by decreasing the concentration of cholesterol (30%, 20%, 10%) and increasing the concentration of DPPC (45%, 55%, 65%). From the temperature scans of specific heat capacity (C_p) in Figure 3.21 , it was observed that the percentage of cholesterol affects the transition temperature of both systems. The T_m increase when the concentration of cholesterol decreases from 30 to 10%, from 52,7°C to 54,7°C for LB and from 52,9°C to 55,5°C for LN. In the case of the cooling scans, a decrease of the transition temperature of 0,6°C is observed, except for the 10% cholesterol case, where ΔT = 0,3°C for LB and LN. Cooling curves are not shown in the figure so as not to overload the image. The decrement of cholesterol produces narrower and better-defined peaks, analyzed by the wave half height (WHH) in Figure 3.21 c) LB and d) LN. These results are consistent with a previous report by Matsinguo and Demetzos [102] on the impact of cholesterol molecules on DPPC bilayers. They reported that, with the decrease of cholesterol-rich domains within the membrane, the cooperative Van der Waals interactions increase yielding an increase of the system enthalpy ΔH.

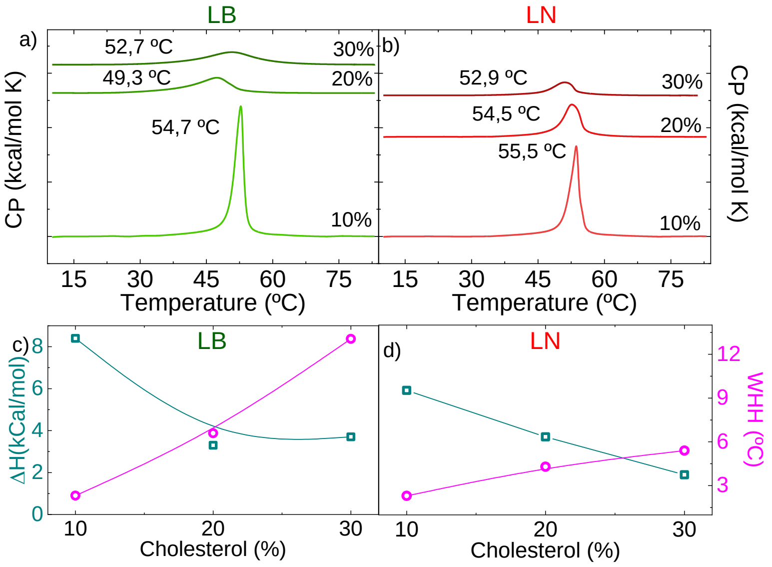

Figure 3.21. DSC heating scans of a) LB and b) LN with varying cholesterol concentrations (10%, 20%, 30%). Plots of ΔH variation (Cyan) and WHH (Magenta) relative to cholesterol content for c) LB and d) LN.

An independent evaluation of the Tm and how it affects the cisPt encapsulation was made using TGA measurements in the range 30 ⍰ T ⍰ 100 °C on dried powder of lipidic samples. The weight loss as a function of temperature and its first derivative for LB, LC, LN and LNC samples (Figure 3.22) showed a similar behavior in all cases, with a smooth loss along the whole temperature range. The loss ranges from 7% for the LB systems 5% for LC, up to a 3% loss for the magnetic systems LN and LNC. However, the derivative of these curves showed a combination of two broad peaks. Comparing with the DSC data, the low temperature peak could be assigned to the transition from Lβ` to Lα phase of the lamella. The second unresolved peak can be related to solvent evaporation/decomposition. The presence of cisPt, seems to lower transition temperature from 57°C for cisPt-free systems (LB and LN) to ≈53,55°C for cisPt-containing systems LC and LNC, respectively. The presence of some drugs is known to modify the Tm or ΔH of the transition gel to the liquid crystalline phase, as reported for cisPt [103], vinblastine [104], doxorubicin [105], and fisetin [106], among others.

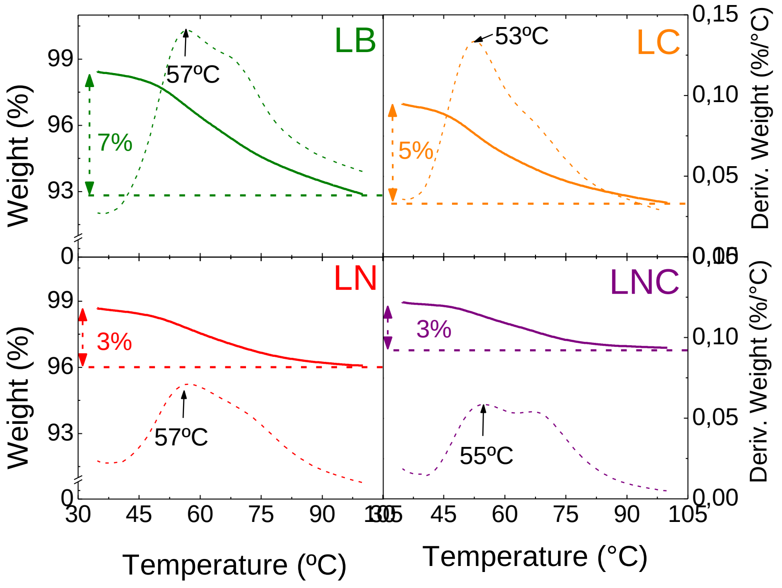

Figure 3.22. TGA Analysis: rate of Weight Loss (%, left axis) and derivative weight (%/°C, right axis) over Temperature for LB (Green), LC (Orange), LN (Red), and LNC (Purple).

The temperature transition of the bilipid membrane to a more permeable state is dependent on the lipid composition, acting as the trigger responsible for the rate of drug release. Through DLS analysis, we aim to discern measurables alterations in liposome size and the response of the system to environmental changes. The DLS examination of the thermal behavior of both LB and LN samples was conducted within the temperature range of 20°C to 80°C. For LB, during the heating process, the initial stages of the experiment (Figure 3.23 a,f) revealed a growth in size from 164 nm to 220 nm, stabilizing until reaching 62°C. Subsequently, a reduction in peak intensity was noted, succeeded by a size increase to 255 nm. This behavior was repeated in the cooling curve (Figure 3.23 b), but with the transition occurring at 70°C. Finally, LB maintained a size of 220 nm. The abrupt size increase was also evident in the count rate (Figure 3.23 c), measuring the number of events counted, which, during the heating curve, shifted from 120 kcps (kilo counts per second) at 62°C to 494 kcps. In the cooling curve, the transition was observed at 60°C. Notably, the analysis of the count rate confirmed that liposomes did not precipitate during the measurement. With Polydispersity Index (PDI) values consistently below 0,25 (Figure 3.23 e), the system exhibited a homogenous behavior, indicating the absence of agglomerations. These results show similarities with the works reported in bibliography [107] [108] [109].

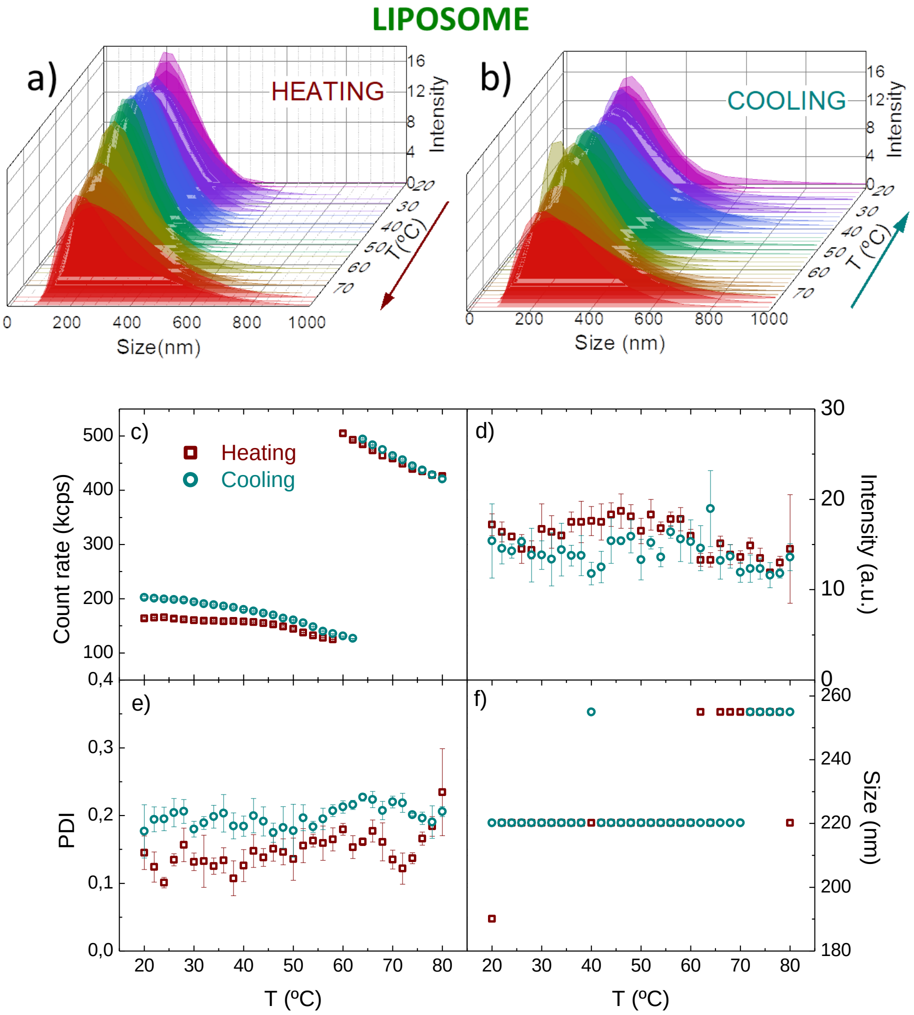

Figure 3.23. DLS analysis for LB. Behavior of size as a function of temperature. a) heating and b) cooling ramp. c) Count rate, d) intensity, e) PDI and f) size vs temperature.

In the case of LNs, the observed behavior is notably more intricate due to their larger sizes and broader size distributions, spanning from ≈50 nm to >2000 nm. This is consistent with the composite nature of the LN and LNC samples (see Table 3.6 below) containing both liposomes and LN. Yet, it was possible to discern a transition from disorder to order. At low temperatures (Figure 3.24 a,f), the sizes values span from 458 nm to 955 nm with the data showing double peaks with minimums of 190 nm and maximums at 1400 nm, indicating the possibility of a mixed system. Above 60°C a more homogeneous behavior is observed with an average size of 530 nm. Down to 48°C, the count rate (Figure 3.24 c) presents an erratic behavior accompanied by large deviations, after 50°C the count number stabilizes at 150 kcps. The same behavior is detected in the cooling curve with a change at 32°C. With PDI values greater than 0,4, LN present a heterogeneous behavior, probably with some aggregate formations (Figure 3.24 d).

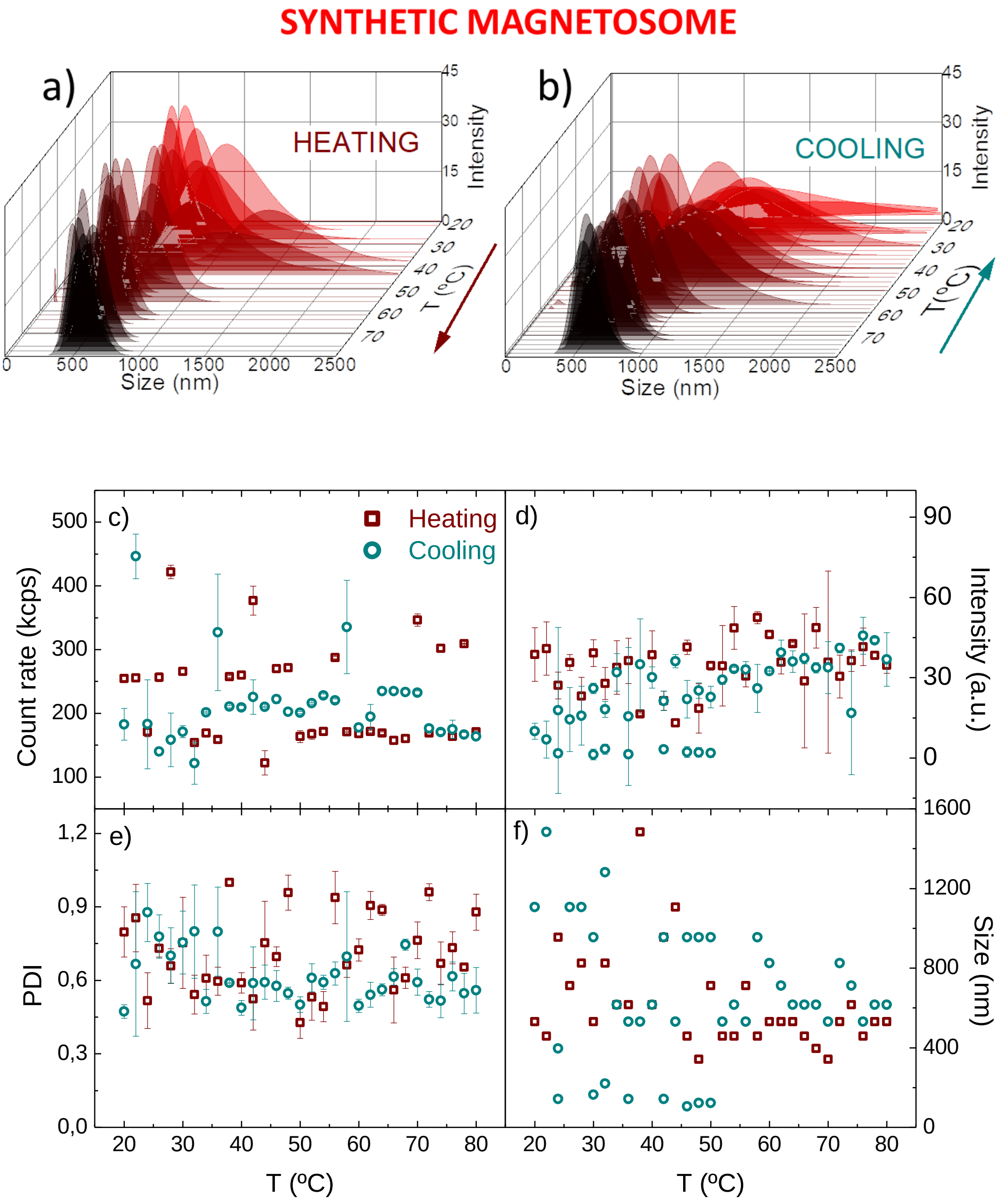

Figure 3.24. DLS analysis for LN. Behavior of size as a function of temperature. a) heating and b) cooling ramp. c) Count rate, d) intensity, e) PDI and f) size vs temperature.

Using three techniques, DSC, TGA and DLS, the T_m from the gel state to the liquid crystalline state of the lipid bilayer of LB and LN was measured. The LB constitutes a rigid system, with a marked change in size above 60°C. The MNPs in the LN enhance the Van der Waals interaction between the hydrophobic tails, which decreases the size distribution above 60°C. The fact that the T_m values found with respect to the size change and in the count rate break, present similarities to those found by DSC, are promising results since, despite being a technique less used and reported for this analysis, the DLS It is a more economical and common equipment in laboratories.

3.3.2. The cisPt-containing magnetosome LNC samples

As previously mentioned, TEM images of LN samples (Figure 3.14) revealed the concurrent presence of empty liposomes (i.e., with no MNPs trapped) and synthetic magnetosomes. This coexistence of some empty liposomes in the LNC samples is consistent with the double peaked size distribution observed from the DLS analysis as a function of temperature, indicating two populations of different sizes. These data triggered the question on the actual composition of the cisPt nanosystem (i.e., the LNC samples), to evaluate whether the cisPt could be encapsulated. To respond to these questions, we performed the following experiment: an aliquot of LNC sample was magnetically separated using strong neodymium magnets into a magnetic precipitated and a supernatant. The precipitate was collected and resuspended in the same volume of medium (Figure 3.25) the size of the LNC samples was analyzed by DLS. The composition of the system regarding lipids, MNPs and CisPt, were carried out as explained in chapter 2. The results of the experiment are compiled in Table 3.6.

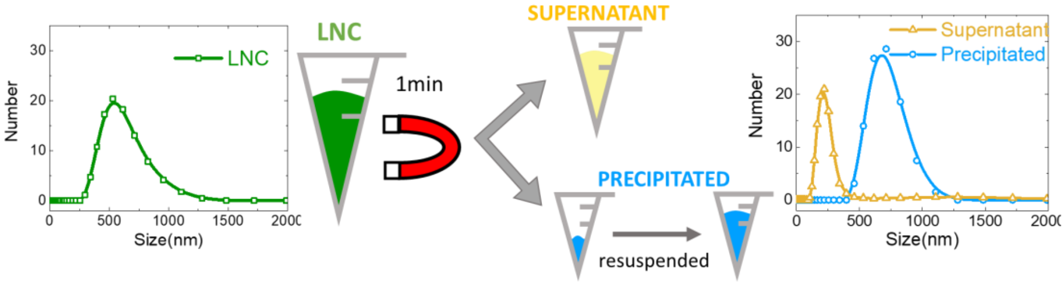

Figure 3.25. Magnetic separation of the LNC nanocarrier in two phases: supernatant and precipitate, together with the respective DLS scan.

The DLS data after the separation experiments showed that in the two samples nanocarriers had different average sizes. For the magnetically separated precipitate we found an average size of <D>= (786±106) nm, whereas the supernatant showed two different, well resolved peaks with average values of (249±83) nm and (1250±548) nm. These values in turn differ from the value in the as prepared LNC with an average size of <D>= (651±182) nm. Additionally, a higher lipid and cisPt concentration was observed in the supernatant, as shown in Table 3.6, together with a remaining (not separated) 20% wt. of MNPs. The magnetic precipitate was composed of a remaining 80% wt. of MNPs, with less than 10% of the cisPt of the original LNC sample. These data suggest that the as prepared LNC system is composed of a mixture of ≈200 nm size nonmagnetic liposomes carrying 90% wt. of the total cisPt (i.e., without MNPs encapsulated) resembling the LC samples, and magnetosomes carrying a ≈10% wt. of the total cisPt load.

Table 3.6. Results of the LNC magnetic separation experiment in supernatant and precipitate. Lipid concentration (mg/mL), MNPs (mg/mL) and encapsulated cisPt (µg/mL). Size (nm) and PDI values obtained by DLS at room temperature.

Sample	[Lip] (mg/mL)	[MNP] (mg/ml)	[cisPt] (µg/ml)	$\langle D\rangle_{DLS}$ (nm)
LNC	8,2±0,4	1,9±0,4	500±20	651±182
Supernatant	7,0±0,3	0,37±0,02	467±21	249±83 1250±548
Precipitate	1,34±0,04	0,9±0,4	33±6	786 ± 106

As mentioned previously, it is evident from cryo-TEM images of LN (Figure 3.14) that the arrays of MNPs, arranged in curved chains, exhibit noticeable gaps between them that are likely originated from lipid bilayer covering each individual particle. The mean size $d = (15 \pm 2)\,nm$ obtained from the HRTEM analysis of the liposomes showed that the lipid bilayer has a thickness of $e = (8{,}1 \pm 0{,}3)\,nm$. Assuming that the particle is a sphere (Figure 3.26 a), with volume $V =$

$1767\,nm^3$ and considering a magnetite density of $\delta = 5260\,kg/m^3$, the mass per particle would be $m_{MNP} = 9295\,10^{-24}\,kg$. A bilipid shell with $V = 4687\,nm^3$ and density of $1000\,kg/m^3$ would yield a value for total mass of the lipid shell $4687\,10^{-24}kg$ 10^{-21} g. In other words, to cover each individual MNP with a lipidic shell would require a MNP:lipid mass ratio of 2:1. Considering the values in Table 3.6, we can see that this condition is fulfilled and that the mass of lipids is much greater than that of the particles. So, we can consider that the lipids not only cover each individual particle, but it is also in excess. We thus concluded that in LNC we have three types of formations: liposomes with cisPt, a curvilinear arrangement of MNPs and an ordered grid of MNPs, with the particles covered by lipids in the last two cases (Figure 3.26 b).

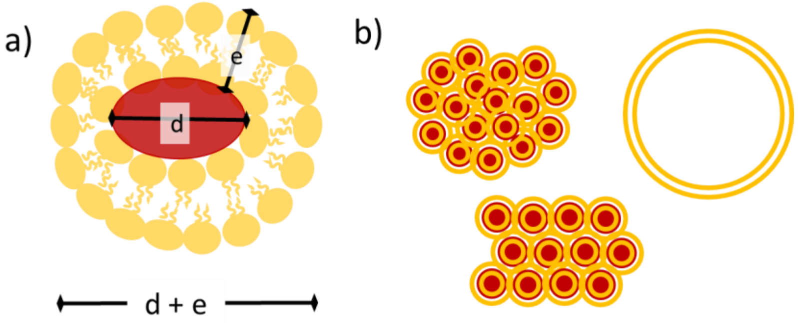

Figure 3.26. Schematic diagram depicting a) the functional unit of LN, and b) the formation of LNC, which likely includes LC and a curly arrangement of MNPs plus a grid of MNPs. In the latter two cases, each particle is enveloped by a lipid bilayer similar to the functional unit shown in a.

If the thickness of the lipid layer of the LB is 8 nm and a layer covers each particle, the separation between particles should be approximately 16 nm, with a particle diameter of 15 nm, that is, between particle-particle we should see a distance equal to another particle. This is not what was observed in the TEM images, the separation between particles being less than 16nm. This may be due to dipolar magnetic interactions between particles, decreasing the space between them. From the DSC analysis it was observed that the Van der Waals interactions in the carbon chains of the LN is greater than that of the LB, confirming the narrowing of the lipid layer. For this reason, we will now study the role played by magnetic interactions in LN.

3.3.3. Nonmagnetic NP-containing Liposomes

The previous results on LN and LNC showed that the final structures of these samples were defined by the synthesis method employed, in this case the reverse phase evaporation (RPE) protocol, as well as the type of lipids used, the size and surface properties of the MNPs, etc. These results led us to hypothesize that along the LN/LNC manufacture two main competing interactions are responsible of the final structure observed: the electrostatic and the magnetic dipolar interactions. While the SC coating the hydrophilic MNPs used for LN synthesis have a negative surface charge with $\zeta = -26\,mV$, the DODAB charged lipids used (to prevent the fusion between lipids during synthesis) yielded a LN positive surface charge with $\zeta = +15\,mV$, greater than the charge of the LB ($\zeta = +4\,mV$). Therefore, a strong lipid-MNP electrostatic interaction can be expected, and therefore the resulting lipid-coated MNPs surface is consistent with these interactions.

A linear chain of MNPs considered as a set of magnetic dipoles is inherently unstable in terms of magnetostatic energy and this structures cannot be maintained unless some type of dynamic equilibrium is involved.[110] It is known that, when isolated, intact magnetosome particles from magnetotactic bacteria naturally tend to keep the chain structures outside the cellular environment, as evidenced by TEM observations.[67] [111] These isolated magnetosomes tend to form lower energy structures like flux-closure rings and folded chains which are more stable for in-plane dipoles. Conversely, when the bacteria are genetically modified to block the expression of the magnetosome membrane (MM) elements, or when they are exposed to detergents like SDS, these structures collapse to agglomerates. This suggests that organic material, providing both spacing and a medium for particle contact, is necessary for chain formation, in agreement with the observed curved configurations in LN and LNC samples, containing MNPs coated with lipids resembling the MM found in bacteria.

As a more direct approach to test whether dipolar interactions are relevant for the chain and curved-chain structures observed in our samples, we decided to synthesize a set of nanoparticle-containing liposomes, but using nonmagnetic silica nanoparticles, with similar size and the same surface coated with citrate groups. We labeled **'silicosomes' ($LSiO_2$)** to these liposomes containing SiO_2 nonmagnetic NPs.

Table 3.7.ζ potential (mV) measured in water for sodium citrate-coated MNPs (SC-MNPs), empty liposomes (LB), magnetosomes (LN), SC-coated silica nanoparticles (SC-SiO_2) and Silicosomes ($LSiO_2$) samples.

Sample	SC-MNPs	LB	LN	SC-SiO_2	$LSiO_2$
ζ Pot (mV)	-26±2	4±1	15,4±0,6	-36±3	4±1

We applied a coating of sodium citrate (SC) to silicon dioxide (SiO_2) particles using the same method employed for the MNPs. This resulted in a size distribution of (42±2) nm for the SC-coated SiO_2, as determined by DLS. Subsequently, we followed the same steps of the Reverse Phase Evaporation protocol to synthesize liposomes containing silica nanoparticles ($LSiO_2$). The zeta potential (ζ) values for this system are listed in Table 3.7 and compared to those from MNPs and LN samples as well as liposomes. These values are consistent with the negative zeta potential observed for SC-coated SiO_2 particles and the positive zeta potential for the $LSiO_2$, similar to that of LB. Room temperature DLS measurements revealed an average size <D>= (350±9) nm for the $LSiO_2$ nanosystem.

FT-IR spectra of the three system (Figure 3.27) showed representative peaks of silicon dioxide: the peak at 806 cm^{-1} corresponding to Si-O bending and the peak at 1064 cm^{-1} assigned to Si-O-Si stretching vibration bond [112]. The presence of the 1394 cm^{-1} and 1575 cm^{-1} peaks in the SC-SiO_2 spectrum due to the symmetric and antisymmetric bending modes of the SC carboxyl group on the surface of the silica particles was corroborated. The asymmetric and symmetric peaks of the stretching of the C-C group, 2850 cm^{-1} and 2918 cm^{-1}, together with the peaks at 1735 cm^{-1}, due to the DPPC ester group, and the peak at 1486 cm^{-1} of the asymmetric C-C bending, confirm the presence of lipids in silicosomes $LSiO_2$.

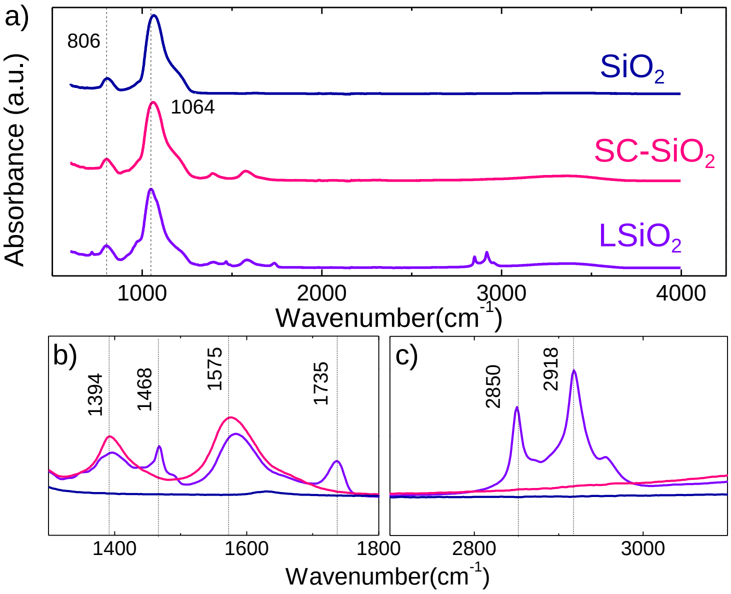

Figure 3.27. FT-IR spectra of powdered samples: SiO_2 nanoparticles (dark blue line), SiO_2 nanoparticles coated with SC shell (pink line), and SiO_2 encapsulated in liposomes (silicosomes, $LSIO_2$, violet line). Lower panels show detailed views of b) C-C bending vibration region and c) regions of Symmetric and Antisymmetric -C-C- Stretching.

TEM images shown in Figure 3.28 exhibit distinctive features in the $LSiO_2$ and LN samples. The $LSiO_2$ samples display particles clustered in agglomerates without any apparent order, a stark contrast to the structured arrangement observed in SC-coated MNPs. On the other hand, the LN samples not only reveal a bilipid layer encasing each individual particle but also demonstrate an organized pattern of MNPs. These results confirm the hypothesis that the orderly chain formation in LN is driven by magnetic interactions and also require the presence of the lipid components which, combined with the SC-functionalized MNP surface, result in the specific lineal structures characteristics of the LN and LNC nanocarriers.

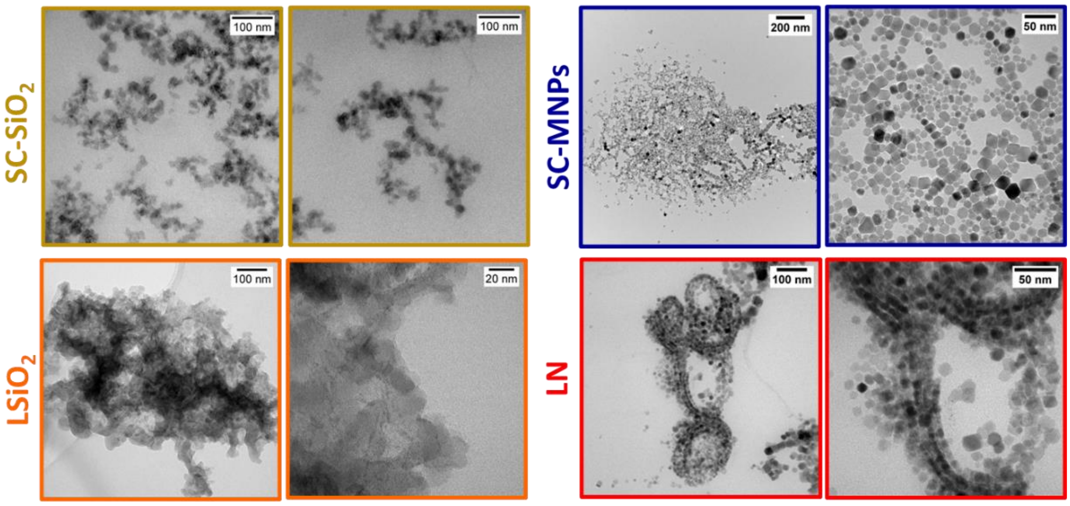

Figure 3.28. TEM images showcasing SC-SiO_2 nanoparticles (upper left -yellow), SiO_2 encapsulated in liposomes ($LSiO_2$, down left- orange), SC- MNPs (upper right -blue) and magnetosomes LN (down right-red). $LSiO_2$ images were obtained using uranyless contrast, LN images were obtained from epoxy resin contrasted with osmium, lead, and platinum.

3.4.Conclusions

As a general conclusion of this chapter, we can say that we have been successful in develop synthetic magnetosomes with the desired properties in terms of composition and properties. The composition observed in these new systems, consisted mainly of liposomes and magnetosomes, both containing cisPt in different proportions. Overall, the nanosystem contains the necessary amount of heating agents (MNPs) to produce high specific loss power (SLP) value, and also contains adequate concentrations of cisPt for their use in chemotherapy, as will be shown in Chapters 5.

We have analyzed in detail the composition of the MNPs chosen for the LN and have observed an excess on the diamagnetic Zn distribution on the surface. This is responsible of the huge contribution to the observed Néel magnetic relaxation, which will be seen in the next chapter. As for the lipid components of the magnetosomes, measurements made by differential scanning calorimetry have shown us that these systems may be suitable for release triggered by magnetic fields at temperatures slightly higher than physiological temperature. The temperature behavior of the LN system measured by dynamic light scattering has shown a complex behavior that requires more systematic studies to determine the evolution of the populations at different temperatures.

Furthermore, we have seen that the use of MNPs coated with this specific functional group (i.e., citrate groups), causes the lipid components in the synthesis of LN to generate a coating over the individual MNPs. This, coupled with the intrinsic dipolar interaction of the single-domain MNPs, generates linear, curved, and spiral structures very similar to those naturally generated by magnetotactic bacteria observed and reported in the literature. The characterization we have carried out and the comparative experiments using non-magnetic silica nanoparticles have confirmed this hypothesis that the co-participation of the magnetic dipolar interaction and the presence of the lipid surface coverage are both necessary to generate these types of structures. As will be seen in the next chapter, these curved chains in magnetosomes have excellent heating properties that also recall the high SLP value found in magnetotactic bacteria [111].

CHAPTER 4

Magnetic properties of synthetic magnetosomes

"…Y tú, conmigo y el gallo a cantar

que hay que empezar un día más.

Tire pa´lante que empujan atrás…"

J. M. Serrat

4.1. Introduction to basic concepts of magnetism

The magnetic properties of a material are shaped by the quantum behavior of the constituent atoms, which are in turn fundamentally rooted in their electronic spin and orbital angular momentum. For this, the magnetization response in magnetic materials arises from the collective behavior of electron spins and their interactions, influenced by the material's atomic structure and external conditions.

The magnetization (M) of a material refers to the degree to which it becomes magnetized in response to an applied magnetic field and is a measure of the magnetic moment per unit volume of the material. When a material is exposed to a magnetic field (H), its magnetization is defined by the magnetic susceptibility (χ), where $M = \chi H$. The best way to introduce the different types of magnetism is to describe how materials respond to magnetic fields. **Diamagnetism** is an intrinsic characteristic of all materials, though it's typically rather weak. Substances exhibiting diamagnetism consist of atoms that lack a net magnetic moment, meaning all their electron orbital shells are complete and there are no unpaired electrons. When subjected to a magnetic field, these materials develop a negative magnetization, leading to a negative susceptibility (Figure 4.1 a). ***Paramagnetism*** is a response from materials in which certain atoms or ions possess a net magnetic moment, due to unpaired electrons in incompletely filled orbitals. These individual magnetic moments do not magnetically interact with each other, and similar to diamagnetism, the magnetization returns to zero once the external field is removed. When a magnetic field is present, there's a partial alignment of these atomic magnetic moments along the field's direction, leading to an overall positive magnetization and a positive susceptibility (Figure 4.1 b).

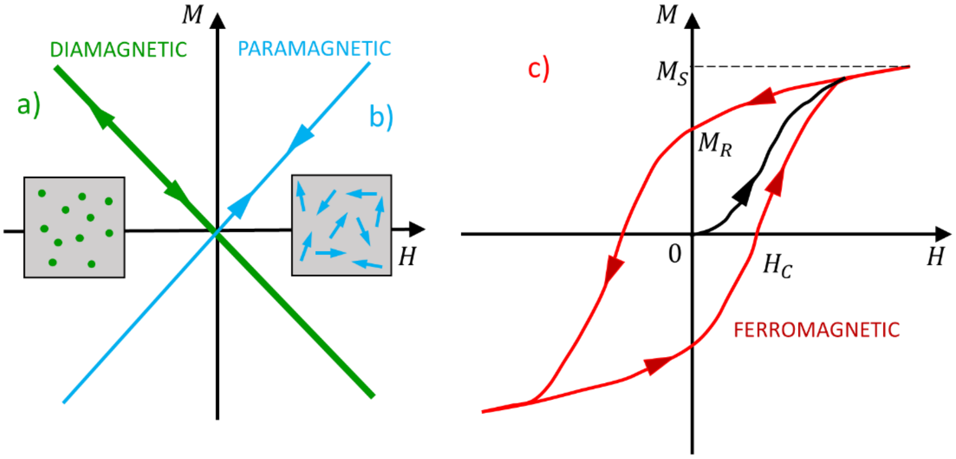

Figure 4.1. Representation of magnetization curves of a) (green) a diamagnetic, b) (blue) a para- and antiferromagnetic, and c) (red)a ferro- and ferrimagnetic.

In **ferromagnetic** substances like iron or magnetite, the most notable effect of magnetism is their spontaneous magnetization, and the associated magnetic hysteresis. This spontaneous long-range order originates in the interactions between atoms in the crystal lattice, known as exchange (or superexchange) interactions. Depending on the magnetic atoms involved their atomic magnetic moments can align either parallel (*ferromagnetic*) or antiparallel (*antiferromagnetic*). In antiferromagnets, antiparallel alignments cancel out magnetic moments, rendering their response to an applied field similar to paramagnets. Conversely, ferromagnetic materials, exhibit spontaneous magnetizations due to strong long-range exchange magnetic interactions, with all magnetic moments aligned in the absence of a magnetic field.

Ferrimagnetic materials have atomic magnetic moments with ferromagnetic and antiferromagnetic interactions, resulting in a net magnetization different from zero. Magnetite (Fe_3O_4) is an example of a natural ferrimagnetic mineral.[113] In the presence of an external magnetic field, ferro and ferrimagnetic materials exhibit a characteristic M(H) curve known as a hysteresis loop, Figure 4.1 c, in this curve saturation magnetization (M_S), represent the maximum induced magnetic moment. Once the magnetic field is removed, these materials present a remanence magnetization (M_r), which to remove the remnant is necessary to apply a field equal to the coercive field (H_C).

4.1.1. Single domain particles

In bulk ferromagnetic material, having all its magnetic moments aligned in the same direction is an unstable state due to the large magnetostatic energy. To reduce this energy, the material breaks into smaller regions called magnetic domains (as shown in Figure 4.2 left). Within each of these domains, the magnetic moments are aligned in parallel. However, the overall direction of these moments is random across different domains, leading to a net cancellation of the total magnetic moment.[114] The boundaries separating two neighboring magnetic domains are called domain walls. Domain walls are essentially two-dimensional areas within the material where the magnetic energy is elevated because, across them, the magnetic moments undergo a forced twist in order to align with the differing orientations of adjacent domains.

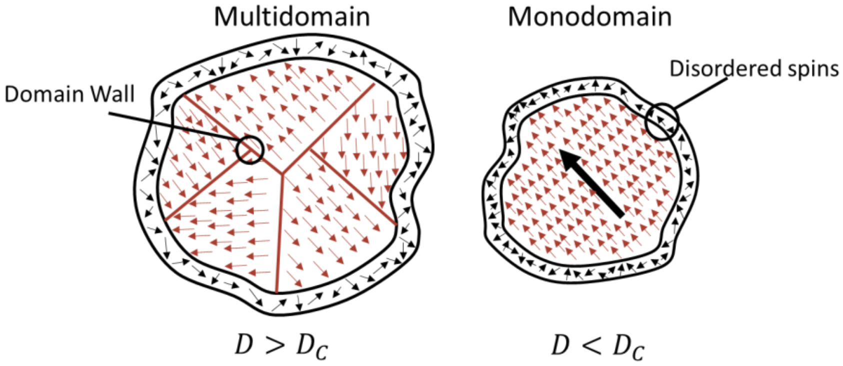

Figure 4.2. Schematic representation of a multidomain and monodomain particle, without magnetic field.

As the size of the material decreases, the proximity between domain walls becomes energetically non favorable. Below a critical size, known as the critical diameter (D_c) for a specific spherical shape, the material adopts a single-domain configuration. In a single magnetic domain, all atomic magnetic moments align in the same direction, effectively acting as a singular, large magnetic moment (Figure 4.2 right). Determining this critical size is not a straightforward task, as it depends on the material's magnetostatic and anisotropic energies. Various authors have proposed different relationships to calculate it [113, 115] [116]. Particularly, for magnetite, a D_C between 80-100 nm has been reported [117] [118].

4.1.2. Blocked and superparamagnetic regimes

For a crystal with uniaxial symmetry the magnetocrystalline anisotropy energy phenomenological expression is given:

$$E_a(\theta) = KV\, sin^2\theta \tag{4.1}$$

here, K is the magnetic anisotropy constant, V is the volume of the particle, and θ is the angle between the easy axis and the magnetization of the particle M. For $K > 0$, the energy exhibits two minima at $\theta = 0$ and $\theta = \pi$, and the product KV is a measure of the energy barrier to overcome for magnetization inversion. These two minima represent two orientations of the magnetic moment of the particle (Figure 4.3a) with equal probability of flipping between these two states, $k_BT > kV$.

When an external magnetic field H is applied, the total energy is given by E_a adding the corresponding Zeeman energy as:

$$E = KV\, sin^2\theta - \mu_0 \vec{H}.\vec{M}_S \tag{4.2}$$

$$E = KV\, sin^2\theta - \mu_0 H M_S\, cos(\alpha - \theta) \tag{4.3}$$

where α is the angle between H and the easy axis (Figure 4.3 b). The presence of the magnetic field reduces the energy barrier by reducing the energy of the minimum at $\theta = 0$ and increasing the one at $\theta = \pi$. Increasing the applied H finally leads to a situation where only the $\theta = 0$ minimum exists. At intermediate situations, the probabilities of the particle being in one of the states are no longer the same and consequently the time associated with transitioning between states.[119] In Figure 4.3 b, shows a simplified case where $\alpha = 0$, and therefore the particle has a higher probability of being at $\theta = 0$. The relaxation time, τ, is the time related to this transition between orientations with minimum energy. In the absence of applied field H the relaxation time for the particle to reach one of the two minima is the same. However, transition between states in opposite directions under applied H is no longer equiprobable, i.e., $\tau_1 < \tau_2$.

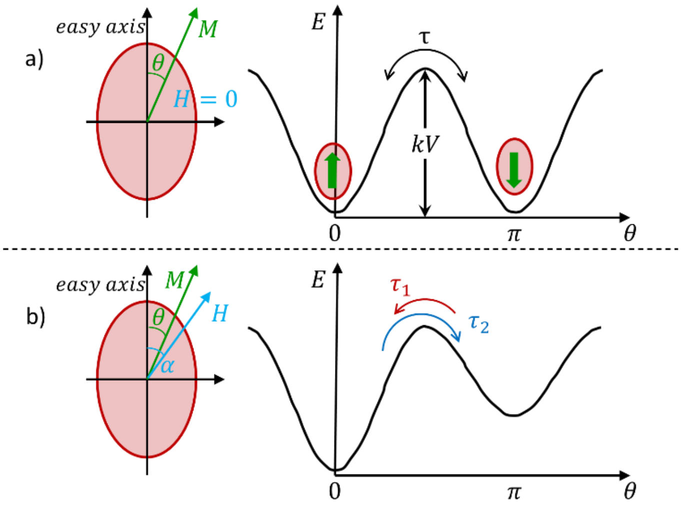

Figure 4.3. a) Depiction of the magnetization M of a single-domain particle and its easy axis. The energy vs. the angle θ in a uniaxial crystalline anisotropy with no magnetic field exhibits two minima, $\theta = 0$ and $\theta = \pi$ with equal transition probabilities between them. b) Same as a) in the presence of an external magnetic field H showing the orientation of M and H with the easy axis. The energy barrier changes due to the presence of H, in the case where $\alpha = 0$. Here, $\tau_1 < \tau_2$ and is more probably to find the particle in the minima where $\theta = 0$.

At finite temperatures $T > 0$, thermal energy can yield spontaneous transition between energy minima. For the case of uniaxial single-domain particles of volume V and uniaxial anisotropy energy KV, this thermally assisted transition between minima will occur if the condition $KV \leq k_BT$ (where k_B is the Boltzmann constant) is fulfilled. This situation defines the superparamagnetic (SPM) state for a given magnetic single-domain nanoparticle. A SPM nanoparticle does not exhibit remanent magnetization or coercive field. Measuring a system of SPM particles requires consideration about the measuring time for each specific experimental technique, specifically the relaxation time τ of the particle and the measuring time for a given technique, τ_m. When $\tau_m \gg \tau$, the system can switch between several states within the measuring time, resulting in an average of states that sums to zero. In this case, we say that the system is in the SPM state. Under this condition, the system has no magnetic memory, and the magnetization is reversible [120]. When $\tau_m \ll \tau$, the magnetic moment takes longer than the measuring time to relax and therefore the system is not in thermodynamic equilibrium. This condition is known as the blocked regime, and the measured data strongly depends on the initial conditions such as field and temperature [120].

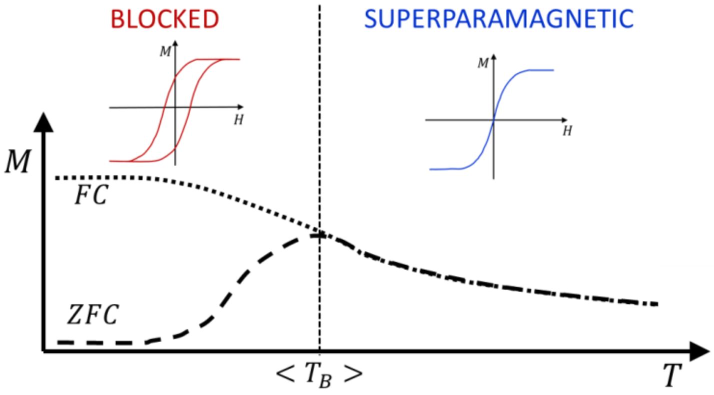

Figure 4.4. Schematic representation of the blocked regime (left) and the superparamagnetic regime (right) of a system of MNPs with a size distribution. Above, hysteresis cycles are plotted for a monodomain particle exhibiting both behaviors. Below, magnetization curves are shown as functions of temperature following the ZFC and FC protocols, highlighting the blocking temperature.

From Equation 4.3 it follows that, for a given particle volume V and effective magnetic anisotropy K, the corresponding product KV defines the transition temperature where the system shifts from blocked to SPM state. This temperature is referred to as the blocking temperature (T_B). In a real system, the sample volume has a size distribution, and therefore T_B refers to the most probable (median) value of the distribution. Zero Field-Cooled (ZFC) and Field-Cooled (FC) measurement protocols are commonly used to determine the $T_B$of the sample. Figure 4.4 schematically illustrates the conditions of the blocked and SPM regimes for the same system.

4.1.3. Relaxation mechanisms in MNPs

Relaxation time, τ, is a measure of the time required for a system to return to its equilibrium state after being disturbed. For MNPs, this involves the process when magnetic moment overcoming the anisotropic energy barrier and reorienting itself. A magnetic field H applied to a system of magnetic particles will perturb the system to align the magnetic moment along the direction of H, provided its magnitude satisfies $\mu_0 H M_S \geq KV$ to overcome the anisotropy energy barrier KV. In 1949, Néel proposed that due to thermal fluctuations the magnetic moments can change their orientation. In the absence of the magnetic field H, and considering the thermal energy to be on the order of the anisotropy energy barrier ($k_B T \approx KV$), the time of a particle transitioning from one minimum energy state to another is determined by the relaxation time (τ) of the system, known as Néel relaxation (τ_N):

$$\tau = \tau_N = \tau_0 e^{\frac{KV}{k_B T}} \qquad 4.4$$

where τ_0 is a characteristic time of the system (usually taken as ≈10^{-9} - 10^{-11} s). This mechanism describes the rotation of the magnetic moment of the particle with the magnetic field and does not involve any physical rotation of the particles. This equation shows that the relaxation time is exponentially dependent on the ratio of the energy barrier to the thermal energy. As temperature increases, or as the energy barrier decreases (either due to a decrease in anisotropy constant K or particle volume V), the relaxation time decreases, leading to faster magnetization fluctuations.

In addition to the Néel mechanism, the Brownian relaxation can also contribute to the effective relaxation of the system. This process implies that the particle physically rotates with its magnetic moment fixed with respect to its crystalline axes. This rotation transfers energy directly to the surrounding fluid in which the system is immersed. The energy barrier to overcome in this case is determined by the frictional force between the particle and the fluid. The Brownian relaxation time τ_B is given by: [121]

$$\tau_B = \frac{3\eta V_h}{k_B T} \qquad 4.5$$

where η is the viscosity of the liquid, and V_h is the hydrodynamic volume of the particle and T is the absolute temperature of the system.

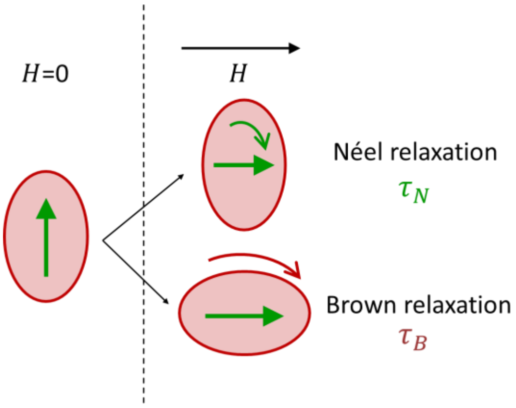

Figure 4.5. Schematic representation of the Néel(up) and Brown (down) relaxation mechanism for a single domain particle in presence of an external magnetic field.

The probability of either the Brownian or Néel mechanism occurring depends on various factors, with particle size and magnetic anisotropy playing particularly crucial roles. Therefore, the total relaxation time of a particle dispersed in a liquid is determined in parallel by both relaxation mechanisms due to the rotation of the particle in the medium, Brown relaxation and the rotation of the magnetic moment of the particle, Néel relaxation (Figure 4.5).

$$\frac{1}{\tau} = \frac{1}{\tau_N} + \frac{1}{\tau_B} \qquad 4.6$$

4.2. Magnetic fluid hyperthermia

MNPs exposed to an alternating magnetic field (AMF) converts magnetic energy into thermal energy. This phenomenon depends on a variety of factors, including intrinsic particle properties, environmental conditions, and the characteristics of the applied magnetic field. In the context of magnetic fluid hyperthermia (MFH), this unique property is harnessed to selectively raise local temperatures, offering a promising therapeutic approach.

To quantify the capacity of a system to convert magnetic energy into thermal energy, the parameter known as Specific Loss Power (SLP) is employed. SLP is defined as the power (P) loss per unit mass (m_{MNPs}) in response to an AMF with a specified frequency (f) and magnetic field strength (H), i.e., $SLP = \frac{P}{m_{MNPs}}$. Various methods for measuring and calculating SLP values are described in the literature. These methods fall into two categories: magnetic determination and calorimetric determination. [122] [123] Magnetic measurement techniques involve detecting induced current in pickup coil, which occurs due to magnetic flux changes when a sample is present. The SLP is then determined by analyzing the area under the $M(H)$ hysteresis curves. Conversely, in calorimetric methods, the progression of temperature is tracked using either contact or non-contact devices, such as alcohol thermometers, thermocouples, ultrasound sensors, infrared cameras, and optical fibers. For these methods, the SLP is calculated using techniques as the initial slope method, the maximum temperature change method, the pulse heating method, or by offsetting the decreasing portion from the increasing part of the $T\ vs.t$ curve [124], and also through the zigzag protocol[125]. Each method has its advantages and disadvantages, but despite differences in data acquisition and handling, SLP values should align within the margin of error.

4.2.1. Initial slope method

From the thermodynamics outlook, the SLP is related to the heat Q lost by the system, through the following expression,

$$SLP = \frac{Q}{m_{MNPS}\,\Delta t} \qquad 4.7$$

stating that SLP is the heat loss per unit of time and mass, in $\left[\frac{J}{kg\ s}\right] = \left[\frac{W}{kg}\right]$ units, where m_{MNPS} is the amount of magnetic material responsible for the temperature increase in the interval Δt. SLP is experimentally measured by the increase in temperature (ΔT) caused by heat dissipation Q from the sample,

$$Q = (m_{MNPs}c_{MNPs} + m_m c_m + m_d c_c)(\Delta T) \qquad 4.8$$

Where m_{MNPs}, m_m and m_d represent the masses of MNPs, the medium in which the particles are dispersed, and the Dewar, and c_{MNPs}, c_m and c_d are their respective specific heats, intrinsic parameters for each material with units $\left[\frac{J}{K\ kg}\right]$. Assuming a homogeneous temperature increase in the suspension and an adiabatic system without heat or mass losses, the contributions of the Dewar were considered negligible. Therefore, by substituting equation 4.8 into equation 4.7, we have,

$$SLP = \frac{(m_{MNPs}c_{MNPs} + m_m c_m)}{m_{MNPs}} \frac{\Delta T}{\Delta t} \tag{4.9}$$

All measurements were conducted in a thermally insulated environment to minimize heat losses. Nevertheless, the system was not adiabatic and therefore the temperature increase was not linear with time due to heat exchange with the medium and the sample holder. A Box-Lucas dependence is a suitable model used as specific approach to account for the heat exchange. Previous work [126] showed a difference of less than 7% between linear and these of fit curve. Additionally, we considered to the approximation $\frac{\Delta T}{\Delta t} \approx \left(\frac{\partial T}{\partial t}\right)_{MAX}$ as valid since the maximum derivative occurs within the first seconds after the magnetic field is turned on, making the heat loss negligible at these short times.

In this thesis, MNPs dispersed in different media such as water, gelatin, paraffin, and toluene were used, and their respective specific heats and densities are detailed in Table 4.1. For all cases, it holds that $c_{MNPs} = 640 \frac{J}{kg\,°C} \ll c_m$. Neglecting the contribution of MNPs in equation 4.9, dividing by the volume of the medium, and rearranging, we get,

$$SLP = \frac{\delta_m c_m}{\varphi_{MNPs}} \left(\frac{\partial T}{\partial t}\right)_{MAX} \tag{4.10}$$

Where $\delta_m \left[\frac{kg}{l}\right]$ is the density of the medium and $\varphi_{MNPs} \left[\frac{kg}{l}\right]$ is the concentration of MNPs.

Table 4.1. Density (δ_m) and specific heat (c_m) values for various media used in specific loss power (SLP) experiments.

Medium	$\delta_m \left[\frac{kg}{l}\right]$	$c_m \left[\frac{J}{kg\,°C}\right]$
Water	1.0	4186
Gelatin	0.9	4186
Toluene	0.87	837
Paraffin	0.9	4710

4.2.2. The Linear Response theory

One of the first equations to describe the power loss in a magnetic colloid subjected to an AMF was provided by R. Rosensweig in 2002,[127] which contained a linear and quadratic SLP dependence on the frequency f and applied field (H_0), respectively:

$$SLP = \mu_0 \pi \chi_0 H_0^2 \frac{2\pi\tau f^2}{1 + (2\pi\tau f)^2} \tag{4.11}$$

where μ_0 is the permeability of vacuum, and χ_0 is the magnetic susceptibility of the material. Reorganizing the SLP (H, f) dependence, we have:

$$SLP = AH_0^2 \frac{Bf^2}{1 + (Bf)^2} \quad 4.12$$

here, A is a field- and frequency-independent parameter that contains the magnetic properties of the MNPs, and $B = 2\pi\tau_{eff}$ is determined by the effective magnetic relaxation time of the system. The relaxation time τ_{eff} is defined by Néel and Brownian relaxation (eq. 4.6). It depends exponentially on the magnetic volume (Néel relaxation) and linearly on the hydrodynamic volume (Brownian mechanical relaxation). Both mechanisms contribute simultaneously to the system, and despite efforts to isolate the contribution of each relaxation, due to the various physicochemical parameters involved, a precise determination is challenging. To predict the main relaxation mechanism of a magnetic fluid, various models have been studied, considering factors such as particle size, anisotropy, and the viscosity of the medium [128].

LRT is a model that assumes magnetization has a linear dependency on the magnetic field ($M = \chi H$), with an effective relaxation time τ. This model has certain limitations [129]. It is most accurate under low magnetic field conditions compared to the material's coercivity ($H_0 < H_c$) [121]. From equations 4.11 and 4.12 it can be inferred that the dependence of SLP on frequency is not linear. Additionally, in the literature, a discrepancy with the quadratic dependence of SLP on the field has been observed, with reported values ranging between 1 and 2 for the exponential dependence [130].

The considerable variability in the experimental parameters for measuring SLP, especially in the amplitude and frequency of applied fields, has led to the proposal of using a parameter known as Intrinsic Loss Power (ILP). This parameter is intended to assess the fundamental capability of the particles, independent of the experimental conditions like amplitude and frequency of the fields. This approach has gained some attraction within the magnetic hyperthermia community. However, as will be elaborated on later, there are limitations to use ILP, as explored in reference [131]. The international standard ISO 19807-1 defines Intrinsic Loss Power (ILP) as follows[132]:

$$ILP = \frac{SLP}{f\,H^2} \quad 4.13$$

where H and f are the frequency and field, respectively, under which the measurement is performed. When the ILP is provided in units of *nH m^2/kg [133]* it gives small numbers, typically between 1 and 4. Despite efforts to render this parameter independent of experimental conditions, it must be noted that ILP will render constant for a given sample only for systems measured under those condition for which the LRT is applies.

4.3. Experimental results and discussion

4.3.1. Temperature and field dependence of the magnetization

Despite the structural difference between LN and MNPs, the 'elemental unit' responsible for the magnetic response is the same in both systems (i.e., the MNPs), and therefore a similar behavior of both systems could be expected. However, when the MNPs are organized within the magnetosomes, the dipolar interactions and lipidic components resulted in chain and curved-chain structures that had an impact on their magnetic parameters. Therefore, a comparative analysis of both types of samples would provide an insight in the magnetic interactions that occur in LN samples, and for this reason we have systematically compared the magnetic properties of LN samples with the MNPs as control samples. The dependence of magnetization on temperature at a constant field, measured using the zero-field cooling (ZFC) and field cooling (FC) protocols, displayed the same general features for MNPs and LN samples (Figure 4.6). The ZFC branch of the data has no clear maximum below the maximum temperature (T) measured, which indicates a broad size distribution of the MNPs in the samples that continuously unblock while increasing T. Both systems exhibited this unblocking process up to the maximum temperature measured $T = 250K$. The FC curves in both systems showed the expected nearly constant behavior along all temperature range, merging with the ZFC curve at $T = 250K$. In a ZFC experiment, since the sample was cooled in $H = 0$, the nanoparticles were randomly oriented when crossing the blocked temperatures. As temperature increased, the smaller particles are the first to realign with the field, and progressively the larger unblock as the temperature increases. This process continued until at $T = 250K$ most of the particles in the system are in a superparamagnetic state. Interestingly, in both systems studied, the unblocking rate as temperature increases were similar. It is worth noting that the absence of a neat maximum in the ZFC curves suggest the average blocking temperature of the systems are located near and above ≈250K, which is an exceptionally high value for particles of $Zn_{0.2}Fe_{2.8}O_4$ with sizes of $< d >$ »$15\ nm$, given that the magnetic anisotropy should be »$10 - 15\ kJ/m^3$. [134]

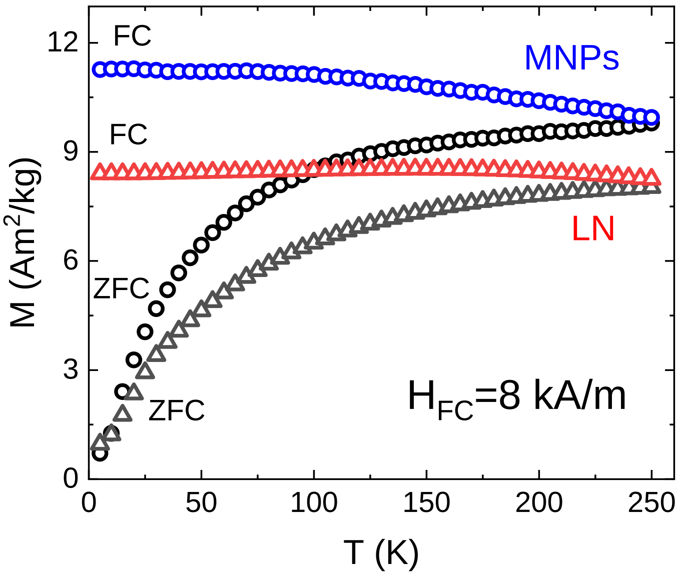

Figure 4.6. M vs. T curves for MNPs (○) and LN (Δ) measured in Zero-Field-Cooled (ZFC) and Field-Cooled (FC) modes. Data acquired under a Field Cooling field $H_{FC} = 8\ kA/m$ *(100 Oe).*

The magnetization measured in the FC process (Figure 4.6) showed an increasing tendency for lower temperatures, indicating a slightly interactive MNPs system. In the LN this effect was much less pronounced, suggesting a larger impact from interparticle interactions.

To analyze the $M\ vs. H$ data we performed the hysteresis cycles by sweeping from H≈ 4 MA.m^{-1} since the M(H) is already saturated for $H \geq 1\frac{MA}{m}$, across temperatures from 4K to 250K. From these results we obtain the thermal dependence of the saturation magnetization $M_S(T)$ and coercive field $H_C(T)$. The observed values of M_S for MNPs, 66 Am^2/kg at 250K (Table 4.2), are lower than the typical values for bulk Fe_3O_4 (92,5 Am^2/kg). However, these values correspond with reports for similarly sized magnetite particles doped with Zn [83, 84, 135]. This reduction in M_S can be attributed to the effect of diamagnetic Zn atoms in the A and B sites of the spinel crystal structure. In a normal spinel configuration, the non-magnetic Zn ions occupy the tetrahedral position (site A), while Fe^{2+} and Fe^{3+} ions align in parallel across the remaining A and B sites. The total system magnetization is defined by the distribution of these magnetic Fe ions [136]. As explored in Chapter 3 and based on XPS analysis, the particle surfaces do not conform to the normal $ZnFe_2O_4$ spinel structure. Instead, the relative Zn and Fe occupancies in the A and B sites present a structural profile that does not fall within the extreme cases of the inverse and normal spinel configurations.

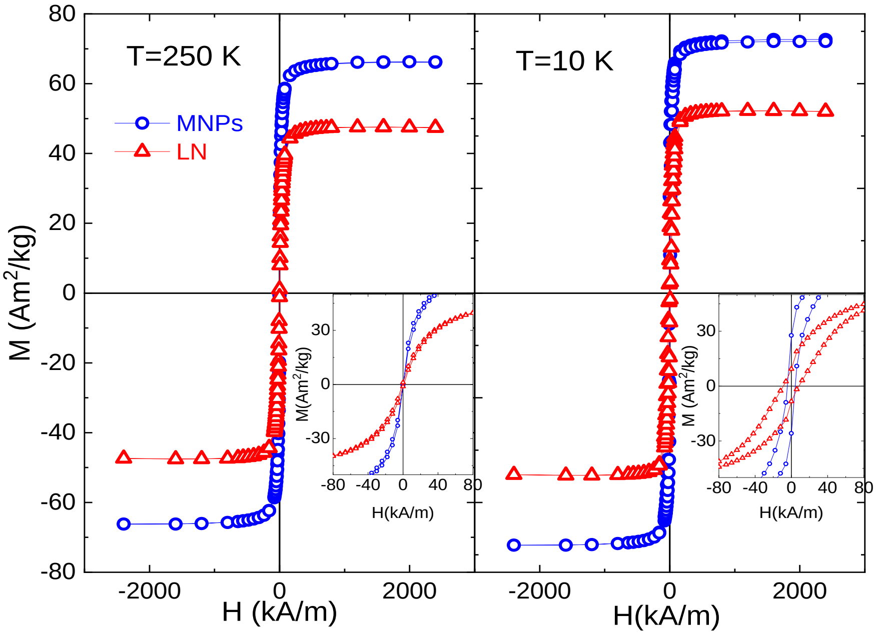

Figure 4.7. M(H) curves at 250K(left) and 5K(right) for MNPs (blue circles) and LN (red triangles). Inset show a zoom around H=0.

We used a simple approximation to calculate the effective anisotropy constant K_{eff} of the MNPs and LN samples, through the relation $K_{eff} = \frac{1}{2}\mu_0 H_C M_S$, and the experimental values of Table 4.2. The values of K_{eff} obtained were 3,1 kJ/m^3 and 2,1 kJ/m^3 for MNPs and LN respectively, coincident and of the same order of magnitude than that of bulk magnetite along the easy [1 1 1] direction of $\sim 11 \times 10^3\ {}^{J}/_{m^3}$[137]. The smaller value of the effective magnetic anisotropy K_{eff} in these samples compared to bulk Fe_3O_4 can be explained from the incorporation of the diamagnetic Zn^{2+} into the crystal lattice. The incorporation of Zn into the Fe_3O_4 crystal lattice is expected to decrease the magnetic anisotropy through changes in superexchange interactions, lattice strain and surface effects in nanoparticles. The Zn^{2+} ions, being diamagnetic, preferentially replace Fe^{2+} ions in the spinel structure, disrupting superexchange pathways between ions and thus modifying the magnetic interaction. Local lattice distortions caused by the size mismatch between Zn^{2+} and Fe^{2+} ions also affect these interactions. In the samples composed by ≈15 nm nanoparticles, surface and interface effects become significant, as Zn^{2+} incorporation modifies surface anisotropy that can dominate the overall magnetic anisotropy of the particle. This is consistent with the non-saturation of the M(H) curves at high fields ($H \gtrsim 10^3\ kA/m$), likely originated from a partial degree of spin canting of the spin alignment within A and B spinel sublattices.

The magnetic softening effect through the inclusion of Zn, clearly evidenced from the H_C values, was deliberately sought to favor Neel relaxation, as mentioned in the introduction of this chapter. The success of this approach is also reflected in the negligible contribution of Brownian relaxation in these systems, as described below in the SLP section. Our measured value of $Keff$ in both MNPs and LN were below the magnetocrystalline anisotropy of bulk Fe_3O_4. Since any contribution from shape or dipolar interparticle interactions should increase the measured K_{eff} values, these can be assumed to be minor compared to the effect from Zn substitution.

The M_S of the LN samples was found to be smaller than that of MNPs at both 250K and 10K temperatures. One reason that could contribute to magnetization decrease is the different coating on the particles' surface. The particles in LN samples self-organize in an ordered structure with the spacing between them not being only the sodium citrate coating but an additional bilayer lipid spacer, as explained in Chapter 3. The presence of both sodium citrate and lipid layers could be a factor in the reduced magnetization of the sample. Incorporated ions on the surface may form a layer that promotes an even oxygen distribution throughout the particle during the synthesis. This could promote an exchange bias effect as reported in some MNPs systems.[138] However, no exchange bias effects were observed in the present MNPs or LN samples following a FC process.

The most likely explanation about this decrease is related to the curved linear structures observed in TEM for the LN samples. Spontaneous tendency to produce closed-loop of magnetic flux would result in decreased magnetization values. [139] Indeed, Molcan et al. [140] noted a similar reduction in M_S in ordered magnetosome arrangements when compared to the same magnetosomes not forming particle arrays. Serantes et al. [141] have proposed that the variations in hysteresis curves might be attributed to different spatial arrangements of magnetic particles, like chains, cubes, and rings. Their focus lies on the distinctions in the Langevin fitting, which typically reduces the hysteresis area. However, in our specific study, differences in the curve shape are not observed; instead, there's only a marginal reduction in H_C and M_R (Table 4.2).

Table 4.2. Saturation magnetization M_S, remanence field M_R and coercive field H_C, at 5K and250K for MNPs and LN.

	MNPs			LN		
T (K)	M_S (Am^2/kg)	M_R (Am^2/kg)	H_C (kA/m)	M_S (Am^2/kg)	M_R (Am^2/kg)	H_C (kA/m)
10	73	27,7	4,4	52	9,0	9,4
250	66	0	0	47	0	0

The dependence of the high-field magnetization with temperature (Figure 4.8) showed that $M_S(T)$ steadily decreases with increasing T, and this thermal decrease could be fitted by the Bloch law,

$$M_S(T) = M_S(0)\left[1 - BT^{3/2}\right] \tag{4.14}$$

$M_S(0)$ is the saturation magnetization at $T = 0$. As shown in the inset of Figure 4.8, M_S of both samples showed a linear relationship between the normalized change in saturation magnetization $[M_S - M_S(T)/M_S]$ vs T³⁄₂ across the entire experimental temperature range (4 K to 250 K). While theoretical models have found a thermal dependence in the form of T^{α} ($3/2 \leq \alpha \leq 3$) for small ferromagnetic clusters, numerous nanostructured systems like α-Fe particles in SiO_2 matrices and γ-Fe_2O_3 nanoparticles have experimentally confirmed a $T^{3/2}$ dependency up to room temperature. For the specific case of MNPs and LN in this study, the fitting procedure yielded a prefactor $B = 2.2 - 2.5 \times 10^{-5} K^{-\frac{3}{2}}$, close to the $B = 3.3 \times 10^{-5} K^{-3/2}$ obtained for spherical magnetite MNPs. The extrapolation of this data to high T yielded a Curie temperature $T_C \approx 1173\ K$ and $1051\ K$ for MNPs and LN samples, respectively. These values are larger than the T_C reported for bulk magnetite ($T_C = 856\ K$) [113], and we associate this deviation to the limitation of the Bloch law at high temperatures.

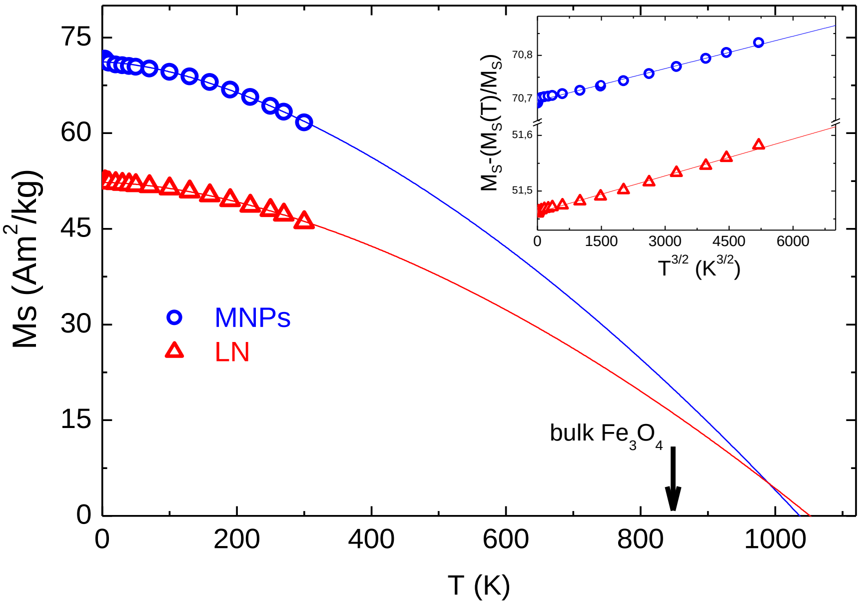

Figure 4.8. High field magnetization temperature dependence for MNPs (blue) and LN (red). Solid lines correspond to the fits of the experimental using equation 4.14 . Inset: lineal dependence of the normalized change in saturation magnetization $M_S - M_S(T)/M_S$] with T³⁄₂.

Figure 4.9 show the thermal dependence of the coercive field with temperature $H_C(T)$, for MNPs, it can be observed that the H_C value remains essentially zero from room temperature down to $T_H \approx 150\ K$ and starts to increase below this value. However, for the LN samples, there is a small but measurable coercive field up to the highest temperature measured. In both cases, below T_H the observed behavior deviates notably from the thermal dependence,

$$H_C(T) = H_{C0}\left[1 - \left(\frac{k_B T}{K_{eff} V}\right)^{\frac{1}{2}}\right] \tag{4.15}$$

expected for thermally activated process in noninteracting, single domain MNPs. [142] Instead, a complex temperature dependence of H_C is observed, not following any simple function of T.

Attempts to fit the $H_C(T)$ data to different temperature dependence using models of incoherent magnetization reversal processes related to interactions such as fanning and curling, [113] which are expected to decrease H_{C0} did not result in acceptable fits. These processes are frequently observed in patterned materials such as MNPs chains and wires.[143] It was not possible to fit the $H_C(T)$ data assuming an oriented assembly within the theoretical model reported by Usov and Grebenshchikov [144], in which the authors proposed a thermal dependence for the coercivity of an oriented MNPs system given by $H_C(T) = A\sqrt{T\ln\left(\frac{T}{C}\right)}$. This dependence is based on a quasistatic magnetization process due to the ratio of energy barrier height (Δ) to thermal energy ($k_B T$) in nanoparticle assemblies. However, none of the above models could fit the $H_C(T)$ measured in our samples.

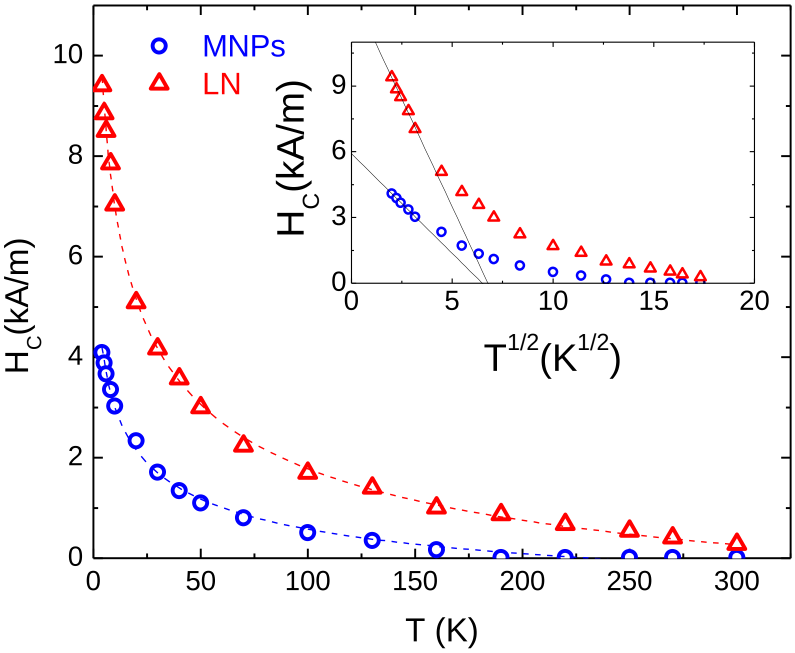

Figure 4.9. Temperature dependence of coercive field for MNPs (blue) and LN (red), dash lines correspond with the fitted curve from eq 4.17 . In inset H_c in function of $T^{1/2}$, the lineal dependence (eq 4.15) was plotted only for low temperatures.

Since the thermally activated regime could be observed only at the lowest temperatures (see inset in Figure 4.9), we aimed to fit the data with a model that consider both superparamagnetic and blocked states of the particles in both samples. Nunes et al. [145] proposed a generalized model that explains this experimental behavior by considering the coexistence of blocked and unblocked particles and introducing a temperature-dependent blocking temperature. We have used the corresponding equation that considers only the contribution from blocked particles (i.e., particles with T_B>T) through their thermally activated dependence of the coercive field, $H_{CB}(T)$ (Eq. 4.16), and the superparamagnetic susceptibility from the unblocked particles χ_S, stated as

$$H_C(T) = \frac{M_r}{\chi_S + \frac{M_r}{H_{CB}(T)}} \tag{4.16}$$

where M_r is the remanence of the particles. Notably, the only thermal dependence in this equation corresponds to the $T^{1/2}$ of the blocked MNPs, that can explicitly be written as

$$H_C(T) = \frac{M_r}{\chi_S + \frac{M_r}{H_{C0}\left[1 - \left(\frac{T}{T_B}\right)^{\frac{1}{2}}\right]}} \tag{4.17}$$

The fits (shown in Figure 4.9) yielded very good fit of the experimental data along the whole temperature range and provided values for H_{C0} of 1,2 kA/m and 2,0 kA/m for MNPs and LN systems, respectively, coincident with the experimental values within error. Also, the values of T_B obtained were 232 K and 382 K for MNPs and LN systems, respectively, suggesting that the larger particles have blocking temperatures close above our experimental measuring limit.

4.4. Specific loss power analysis

As previously mentioned, the purpose of the MNPs synthesized in this work was their application as nanoheaters, for MFH, and thus the first step was to optimize their heating efficiency under alternating magnetic fields. One of the limitations that hinders clinical advancements of MFH as a therapy is the low heating efficiency of the formulations. Some attempts to improve it include increasing the *in situ* particle concentration, using higher frequencies or fields, and extending the treatment time. Based on the previous results of our group, it is not only necessary to modify the magnetic characteristics of the nanoheaters, but also the stability and preparation of the sample, data acquisition, and measurement reproducibility.

In Chapter 3 we discussed the SLP values of a series of $Zn_xFe_{3-x}O_4$ nanoparticles (Zn-MNPs) with increasing x values dispersed in both toluene and paraffin matrices. The results revealed a variation in the SLP values with the contents of Zn. A general trend observed was that, when the MNPs were embedded in the paraffin solid matrix, there was a substantial reduction in the SLP values compared to those from MNPs dispersed in liquid toluene. This decrement is assigned to the absence of Brownian contribution to the SLP in the solid matrix. Although sample with $x = 0{,}1$ showed the larger SLP values in toluene, the sample selected for *in vitro* application in the following work was sample $x = 0{,}2$, since it presented maximum SLP values for solid matrix, which is the best approach to the situation for these MNPs within cells. Also, a higher reproducibility in solid matrix was observed when paraffin was used, which can be ascribed to the enhanced system stability during the experiments due to the immobilization of the nanoparticles. This immobilization mitigates the formation of non-uniform particle assemblies and agglomerates, which could otherwise introduce measurement anomalies. This is of relevance for MFH applications. The MNPs were dispersed in rigid matrices like paraffin and gelatin, ensuring a controlled MNPs distribution, and the analysis focused on the Néel relaxation mechanism for heating, which is the critical component for *in vitro* experimental evaluations.

4.4.1. SLP experiments for different surface coating MNPs

As mentioned in the previous paragraph, the sample selected for this work was $Zn_{0.18}Fe_{2.82}O_4$, i.e., $x = 0.2$. As explained in Chapter 2, the *as obtained* MNPs had an oleic acid (OA) coating, subsequently modified by a sodium citrate (SC) shell through a ligand exchange protocol. The influence of the different coatings on the heating efficiency in presence of an alternate magnetic field was evaluated through the SLP dependence on the applied magnetic field from 14 to 24 kA/m at a fixed frequency of 570 kHz (Figure 4.10).

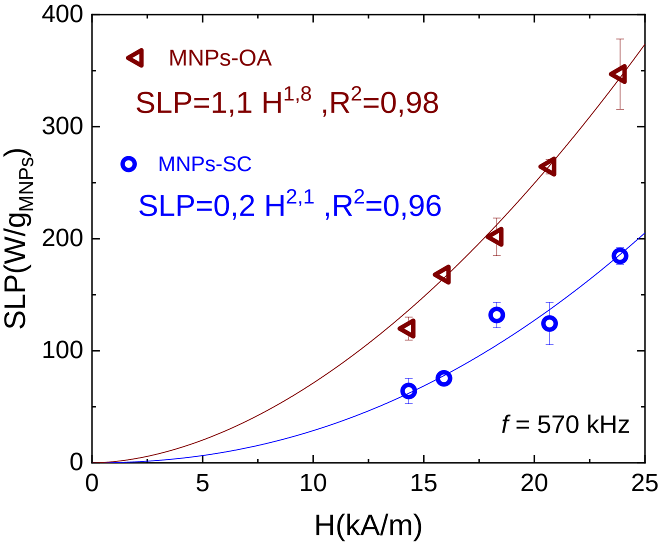

Figure 4.10. SLP dependence with magnetic field H at 570kHz for MNPs-OA (brown triangles) and MNPs-SC (blue circles). The data was fitted by the dependence $SLP = aH^b$.

The MNPs coated with OA, were fixed in paraffin, and MNPs coated with SC, in gelatin. Both showed a dependence with H that followed the law $SLP = aH^b$, with a and b as fitting parameters. In Figure 4.10, it can be observed that the SLP values for MNPs with OA coating are systematically higher than the corresponding SC-coated MNPs. There different SLP values could be explained by the degrees of partial agglomeration, the existing in the previous liquid phase. Agglomeration originates dipolar magnetic interactions that modify the magnetic response, as will be discussed below regarding chain formation. These effects are difficult to predict, and therefore a more complete series of experiments dedicated to disentangling the agglomeration effect on SLP would be necessary. Also, surface effects that could alter the spin alignment could influence the magnetic behavior due to the change of the chemical bonding with the coating molecules. However, for the pristine MNPs with $d = 15\ nm$, surface effects should be small.

The SLP dependence on H was analyzed for both coatings, yielding a H dependence very close to H^2. The quadratic dependence of SLP on H under LRT approximation is expected when the MNPs are small enough, and/or H satisfy the conditions discussed previously in Section 4.2.2. As shown in Figure 4.10, the SLP dependence on the magnetic field H is very close to H^2 as could be expected from the LRT approximation, and therefore the use of the ILP parameter can provide information about possible differences of intrinsic heating mechanisms on the studied samples. The calculated ILP values for *the same* MNPs with OA and SC coatings were consistently independent of H but differ by ≈50% between these samples with different coatings (Figure 4.11).

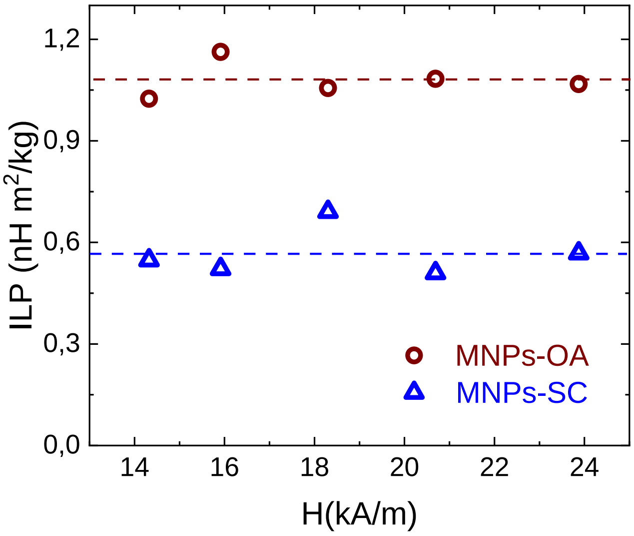

Figure 4.11. ILP dependence with magnetic field (H) at 570kHz for MNPs-OA (brown triangles) and MNPs-SC (blue circles).

Given that the core composition of the MNPs were similar in both experiments, the observed differences can be attributed to multiple factors. These include, the formation of agglomerates, changes in the surface properties of the particles, and the varying dispersion mediums, namely paraffin and gelatin, as outlined in Table 4.1. Previous studies [146] [147] have documented the impact of different coatings on the efficiency of nanoheaters in MFH therapy, through the variation of particle-particle interactions, influencing the stability of the sample, agglomeration degree, and ultimately affecting the heating efficiency of the MNPs.

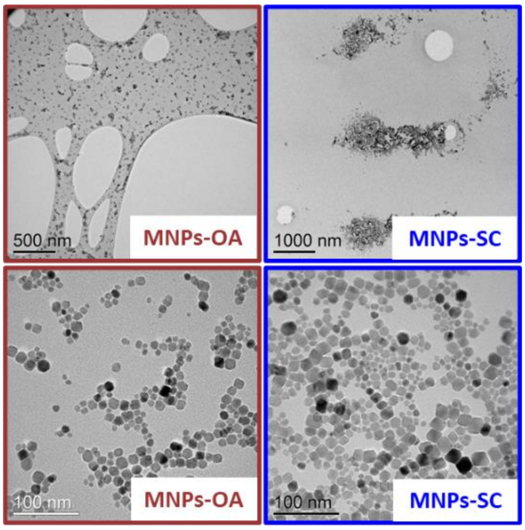

Figure 4.12. TEM image of dispersed MNPs coated with OA (left) and agglomerated MNPs coated with SC (right).

We did observe some increased tendency to agglomeration in particles coated with SC compared to the easier dispersion of MNPs-OA colloids, exemplified in Figure 4.12. Since the effect of agglomeration has been reported to produce both increase and decrease of the SLP values, it is not clear if the different agglomeration degree in our samples could have originated the changes observed in SLP.

4.4.2. SLP in MNPs and synthetic magnetosomes

The heating capability of our nanovector under the influence of an AMF depends, among other factors, on the amplitude H_0 and frequency f of the applied field. In previous sections, we have mentioned that the ILP is a parameter that allows us to normalize the power absorption of the system, independent of the applied f and H_0. This standardization is valid only under the hypothesis of the LRT. Nevertheless, it is important to represent the dependence of power absorption as a function of both field amplitude and frequency to identify the regions where heating is most effective. In Figure 4.13, a 3D map depicts the distribution of power absorption for MNPs and synthetic magnetosomes (LN). This representation reveals that the regions of the field and frequency where the SLP is maximized are closely related in both, but there is a noticeable increase in SLP for LN, reaching levels as high as 1500 W/g. This mapping presented allows us to predict the magnitude of the temperature increase for a given concentration as a function of the fields and frequencies that are experimentally viable for an *in vivo* application.

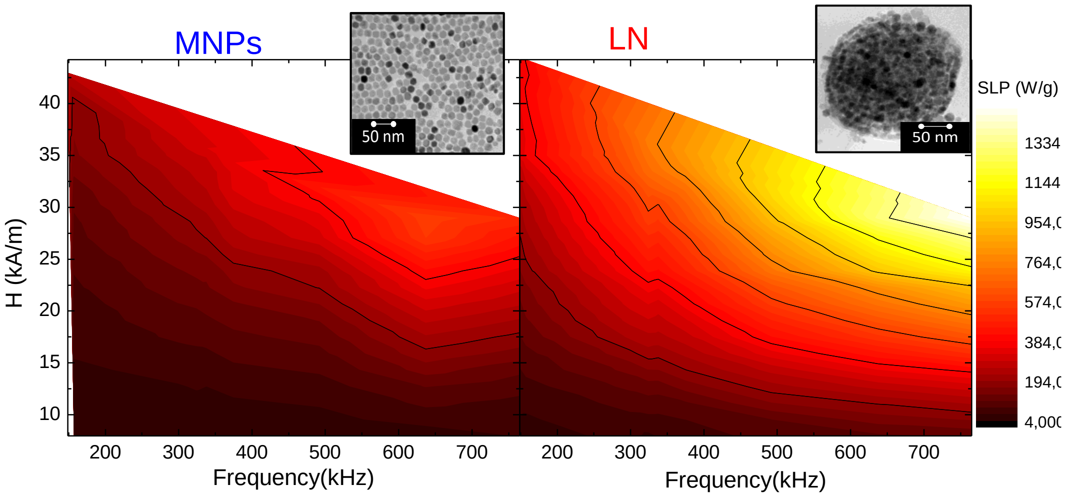

Figure 4.13. Map of the SLP distribution as a function of the field H_0 and frequency f of the AMF applied for MNPs (left) and LN (right), fixed in gelatin. On top panel, TEM image of the MNPs and LN system.

The dependence of SLP on nanovectors has been meticulously investigated within the range of $8 < H < 29$ kA/m and $149 < f < 765$ kHz. Figure 4.14 shows the different results as a function of field amplitude for MNPs and LN, with the corresponding fits using the function $SLP = aH^b$ where the parameter b for the field dependence is expected to be approximately two for the LRT regime. The figure reveals that the fits with the allometric function give good results and the values of b obtained, which are shown in the Table 4.3. Despite some minor variations, these values are consistently close to $b \approx 2$. Notably, for LN, all values are lower than 2 except at 375 kHz. In the case of MNPs, the dispersion is less than 10%.

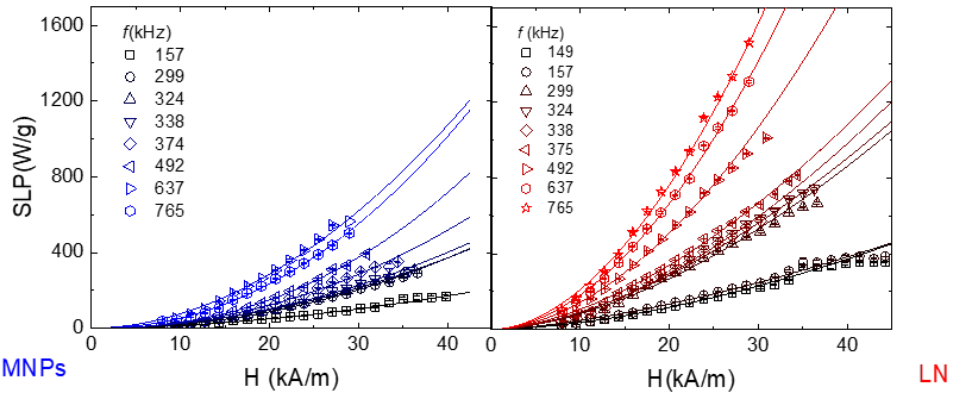

Figure 4.14. SLP dependence with magnetic field H at different frequencies for MNPs(left) and LN (right). The data are fitted by the dependence $SLP = aH^b$.

In addition to the H-dependence of SLP, we explored the change of SLP as a function of frequency. Figure 4.15 reveals the expected "s"-shaped curve as described by the equation 4.11, that can be expressed more simply as

$$SLP = A \frac{Bf^2}{(1 + (Bf)^2)} \tag{4.18}$$

with A and B frequency-independent parameters to fit the data. This equation with only two free parameters A and B provided a good fit in the whole available frequency range.

Table 4.3. Parameters obtained from fitting $SLP = aH^b$ on Figure 4.14 of the dependence of the SLP(H) values for MNPs and LN.

f (kHz)	MNPs a	b	R^2	LN a	b	R^2
149	-	-	-	0,8	1,7	0,998
157	0,2	1,8	0,985	1,5	1,5	0,996
299	0,2	2,1	0,995	1,7	1,7	0,990
324	0,3	1,9	1	2,0	1,7	0,995
338	0,3	2,0	0,995	1,6	1,7	0,991
375	0,2	2,1	0,998	1,7	2,3	0,992
492	0,2	2,2	0,998	2,1	1,8	0,990
637	0,9	1,9	0,99	2,5	1,9	0,994
765	0,4	2,1	0,995	2,9	1,9	1

The sigmodal ‘s-shaped’ increase with frequency was observed at all frequencies (though only discrete data points were available given by capacitor combinations in the LC-tank). We observed different dependencies in the data for the MNPs and LN samples. For the latter, the $SLP(f)$ function showed a stronger dependence, implying that this region of higher frequencies was the most effective even at intermediate fields. This brings into consideration the safety limits formerly suggested for clinical applications by Atkinson and Brezovich ($H \times f = 4.85 \times 10^8 \frac{A}{m \times s}$) [148] to avoid dielectric currents on healthy tissues. Since this limits depends on the radius of the target region[149] and it has been challenged in recent reports, [150] it is worth investing efforts to explore regions of higher $f \times H$ values, as well as in higher-power equipment, as this limit is likely to be further challenge in future clinical situations.

From the fits shown in Figure 4.15 and equations 4.11 and 4.12, the average magnetic relaxation times obtained to be were $\tau = 270\ ns$ and $\tau = 283\ ns$ for MNPs and LN, respectively. Since the samples were dispersed in a solid gelatin matrix, we can approximate that the effective relaxation time is solely due to contributions from the Néel relaxation mechanism, meaning $\tau \approx \tau_N$.

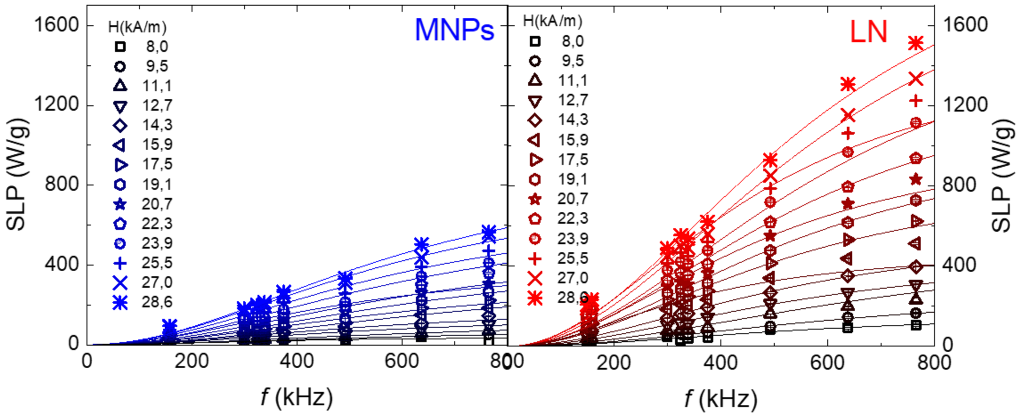

Figure 4.15. SLP dependence with frequency for fields between 8<H<29kA/m for MNPs(left) and LN (right). The data are fitted by the dependence $SLP = A\ \frac{Bf^2}{(1+(Bf)^2)}$.

Given the strong dependence of SLP with f and H yielded large variation in SLP values within the available experimental region, we tried to gain more insight by translating the SLP maps into the corresponding ILP values (defined in Section 4.2.2). The results are shown in Figure 4.16, after collapsing the $H - f$ plane onto the $ILP - H$ plane of the figure. For the MNPs, relatively constant values of $ILP = 0.9 - 0.6\ nH.m^2/kg$ were obtained across the entire H range. In the case of LN, a clear dependence on both f and H was identified, with a maximum value $ILP =$ 2,7 $nH.m^2/kg$ and spanning lower values down to $ILP \approx 1.5\ nH.m^2/kg$ at high fields. For fields greater than 30 kA/m, the ILP value dropped notably. The obtained ILP values align with those reported in the literature [131] [151], where values of up to $7 - 8\ nH\ m^2/kg$ have been recorded for particle systems (such as nanoflowers) at 1 MHz and 7 kA/m [152] [153].

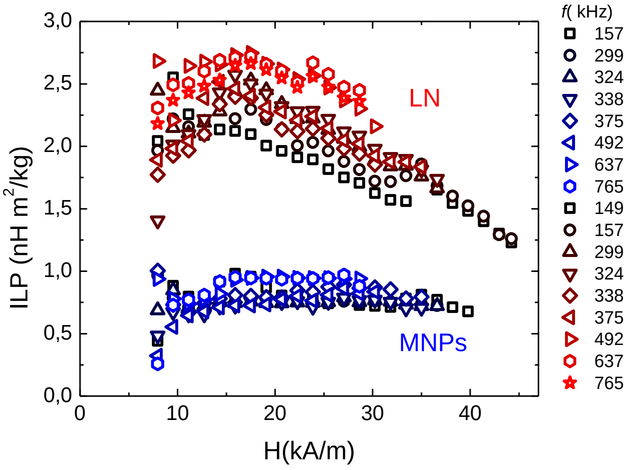

Figure 4.16. ILP dependence with magnetic field (H) *at* $149 < f < 765kHz$ *for MNPs (blue) and LN (red).*

4.4.3. SLP in *“in vitro”* assay

One of the most interesting findings related to the heating capabilities of the synthesized systems was the difference observed between MNPs and LN when comparing results gelatin-fixed form (previously discussed) and the results obtained from *in vitro* experiments. A notable result is the increase of the SLP from MNPs in gelatin to the *in vitro* values, matching those observed for LN samples. In Figure 4.17, it is evident that the higher values of SLP≈ 1600 W/g ($f = 765\ kHz; H = 29\frac{kA}{m}$) obtained only for LN in gelatin were observed only for **both LN and MNP *in vitro***. While LN internalized by cells maintains a similar value than in gelatin, **the MNPs showed an increase by a ≈4 factor when the particles are incorporated into the cells**.

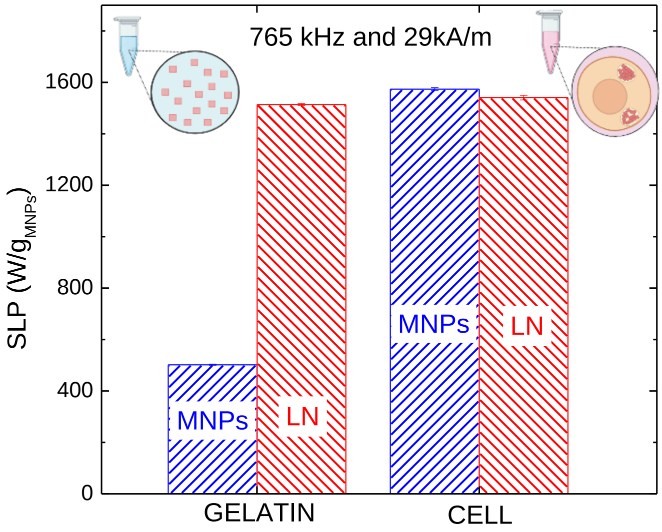

Figure 4.17. A comparison of SLP values of MNPs (blue) and LN (red), fixed in gelatin (left) and internalized in PAN02 cell line (right), at $f = 765\ kHz$ and $H = 29kA/m$.

The explanation for this behaviour is likely to be related to the formation of linear structures of the MNPs in the presence of lipids membranes. In Chapter 3 we discussed the affinity of lipids to the citrate functional groups used to transfer the MNPs to water medium. This affinity results in a lipidic coating of the MNPs in the LN samples. The combined effects of the dipolar interaction among MNPs (promoting agglomeration) and the lipidic component on the surface (favouring curved organization) results in the observed curved linear arrangements when both interactions are at play. While during the synthesis of the LN samples the MNPs are in contact with the lipids to form the magnetosomes, the same type of lipids is abundant when the MNPs are incorporated into the cell cytoplasm. These interactions could explain the similar curved linear structures observed in both LN samples and MNPs within cells. From the TEM images extensively discussed in Chapter 5, it could be observed that MNPs are confined within vesicles with a certain degree of linear arrangement (see also Figure 4.18). In turn, the interactions resulting from the ordering in curved linear structures could explain the significant increase in the SLP of the nanoparticles in the cellular environment. Therefore, these spiral linear structures of MNPs in LN and within the cell cytoplasm would be ultimately responsible for the large $SLP \approx 1600\ W/g_{MNPs}$ values observed in both LN and in vitro.

The impact of the formation of ordered 3D structures on the increase or decrease of SLP is a topic of ongoing debate and has yet to reach scientific consensus[154, 155].[156] It is worth mentioning that the effect of the linear chains of MNPs to increase the value of the absorbed power SLP has already been reported in the literature with values ranging between 2 and 6 times for chains aligned in the direction of the applied field. In our case, both LN and MNPs within the cytoplasmic environment form chain-like arrangements that are initially immobilized and oriented randomly with respect to the applied magnetic field. This suggests that the model of chains as reported in the literature needs further discussion and a deeper analysis to understand the impact of the chain structure on the SLP and not just their orientation in the case of linear chains with respect to the field. Clearly, the situation of the LN and MNPs in our experiments is more complex since we do not have oriented linear chains but, as can be seen in Figure 4.18 the agglomerates consist of interlocking curly chains that form 3D structures.

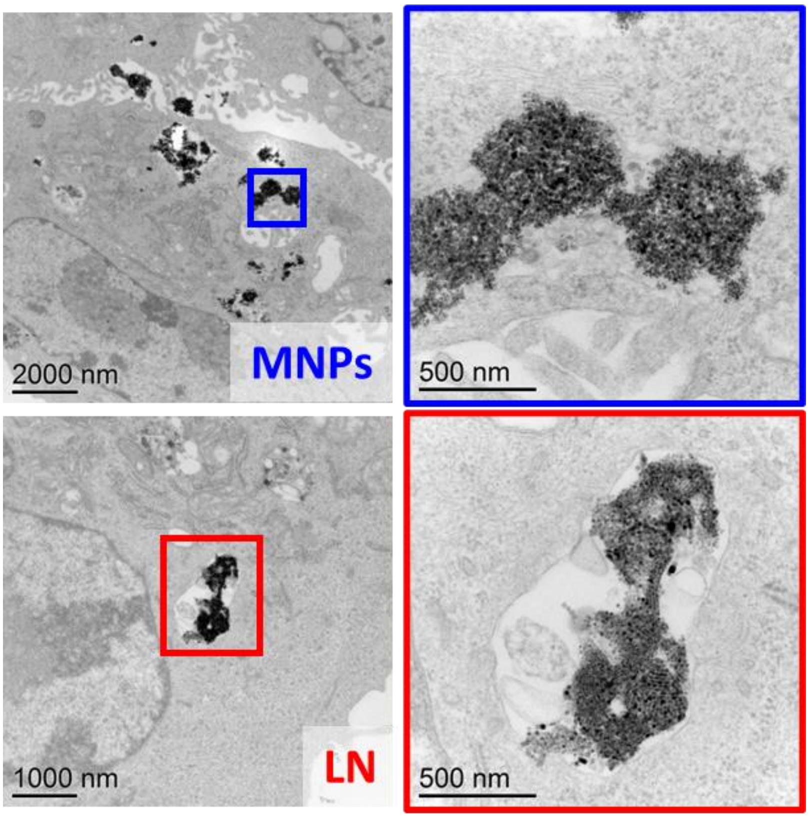

Figure 4.18. In vitro SLP experiments in PAN02 cell line. Above: TEM images of arranged cluster of MNPs in vesicles internalized by the cell. Below: TEM images of the LN inside the cell.

The formation of *curved linear* structures of MNPs within cells or in *synthetic* magnetosomes have not been previously observed in the literature and may be attributed to the specific nature of the SC coating on our particles. As seen in Chapter 3, MNPs-SC have a negative ζ-potential, while LN have a neutral surface charge, making dipole-dipole interactions responsible for chain-like arrangements. The lipid bilayer is similar to the cell membrane, which is why it is possible that the presence of the cellular environment neutralizes the surface charge in MNPs, leading to chain-like structures within the cell vesicles. As shown in Chapter 3, the interaction between SC and liposomes does not result in ordered particle structures. Working exclusively with particles internalized in the cell, which clearly alters the system's arrangement, could be the reason for the increase in SLP in cells compared to the system dispersed in gelatine.

4.5. Conclusions

In this Chapter, we have presented some of the magnetic properties of both the constituent MNPs of magnetosomes and the magnetosome as an entity. We have shown that the formation of MNPs chains within the magnetosome, described in the previous chapter, are the origin of a unique magnetic behavior, as well as a of the very high SLP values of $\approx 1600\ W/g_{MNP}$ $(f = 765\ kHz; H = 28\ kA/m)$ obtained for LN, and MNPs in the cell cytoplasm. The magnetic properties of the synthetic magnetosomes, such as the thermal dependency of M_S and H_C, were very similar to those of the constituent MNPs. Both show dependencies that are unusual for thermally activated single-domain particles. Conversely, the SLP showed by the MNPs, and LN samples were very different: the latter showed a much higher SLP value due to the effect of the curvilinear chains formed during the synthesis of LN. Remarkably, when the MNPs were incorporated by our PAN02 cells, this jump in SLP of a factor of ≈ 3 was reproduced. The explanation is that the lipid membrane and with the dipolar interactions yielded the observed characteristic set of curvilinear chains of MNPs, ultimately responsible for the enormous SLP value of $1600\ W/g_{MNP}$ found in the magnetosomes.

CHAPTER 5

In vitro toxicity, thermal dose and synergistic MFH+CT therapy

"…Tu amor, parábola de un mundo mejor.

Tu amor me enseña a vivir.

Tu amor me enseña a sentir. Tu amor.

Yo tuve el fin y era más,

yo tuve más y era el fin,

yo tuve el mundo a mis pies y no era nada sin tí…"

C. García y P. Aznar

5.1. Introduction

As mentioned in Chapter 1, the rationale behind the use of combined therapies for cancer treatment is to trigger synergistic effects that could improve the therapeutic outcome. In light of cancer being recognized as a complex adaptive system characterized by non-linear dynamics [157], numerous theoretical and empirical investigations have presented convincing findings regarding the interplay among different factors contributing to tumor formation and the ability of cancer to resist therapy [158]. Furthermore, diverse genetic and non-genetic mechanisms have been identified that control the transformation of cancer cells into a drug-resistant state within specific cancer types.[159]

In the context of biomedical applications of MNPs, we are interested in how MNPs can play a role in addressing the multiparametric nature and treatment of cancer. Chemotherapy (CT), radiotherapy, immunotherapy and hyperthermia are used as co-therapies in order to treat heterogeneous tumors, reduce adverse effects and avoid tumor cell resilience. In the case of hyperthermia, the temperature increase is known to mainly contribute to stimulate blood perfusion that irrigate those areas more vascularized, sensitizing and permeabilizing the affected area. Its implications have been studied in radiotherapy [160] [161] and CT[48]. The synergistic effects of magnetic fluid hyperthermia (MFH) together with CT, including cisPt, have also been reported [47]. For instance, pancreatic cancer cells, one of the systems studied in this chapter, are well known to be one of the most aggressive recalcitrant malignancies and portends a high mortality rate.[162] Pancreatic cancer cells commonly exhibit intrinsic resistance to CT, both as an initial response and as resistance that develops over time. This resistance has been a major challenge in achieving good results with conventional approaches. Several potential mechanisms have been proposed to contribute to therapeutic resistance in pancreatic cancer (g.e., against gemcitabine) that include genetic mutations, epigenetic reprogramming, aberrant signaling pathways, and interaction from components of tumor microenvironment.[163]

The concept of synergistic effect (also known as synergy) refers to a phenomenon in which the combined action or interaction of two or more factors, substances, or components produces a result that is greater, more potent, than the sum of their individual effects. In medicine, it is often used to describe situations where the combined effect of multiple drugs/actions leads to a therapeutic result that exceeds the simple additive effects of the individual elements. Although many models have been proposed to predict the interaction between compounds[164], the two most widely used are the Bliss independence model[165] and the Loewe additive model [166],[167]. The Bliss independence describes a scenario where two (or more) drugs act independently but still contribute to a cumulative effect, assuming no direct interaction between them. Drugs A and B act independently if the surviving fraction (S) of cells upon simultaneous administration, denoted S_{AB}, is equal the product of surviving fraction using drug A (S_A) and using drug B (S_B), when drugs are given separately,

$$S_{AB} = S_A \cdot S_B \tag{5.1}$$

It is said that synergy occurs when $S_{AB} < S_A S_B$, and antagonism when $S_{AB} > S_A S_B$. This definition of Bliss independence can be understood as follows: if administering a drug A results in a fraction S_A of surviving cells in the population, subsequent administration of drug B will ***only impact the living cells that survived drug A***. Therefore, if both drugs operate independently, the proportion of cells that remain alive after both drugs are administered simultaneously is represented by the product $S_A S_B$. The probabilistic interpretation of synergy can be made straightforward by associating surviving fractions if S_A and S_B in the cell population with probabilities of death of a single cell due to single-agent administration of either drug A or B, respectively. If the events of survival are denoted as A and B, then their probabilities are $Pr(A) = S_A$ and $Pr(B) = S_B$. Therefore, the probability of survival (see Figure 5.1) after subsequent or simultaneous administration of both drugs is the product of the two (assumed independent) probabilities, the intersection of survival of both treatments (∩)

$$S_{AB} = \Pr(A \cap B) = \Pr(A) \cdot \Pr(B) \tag{5.2}$$

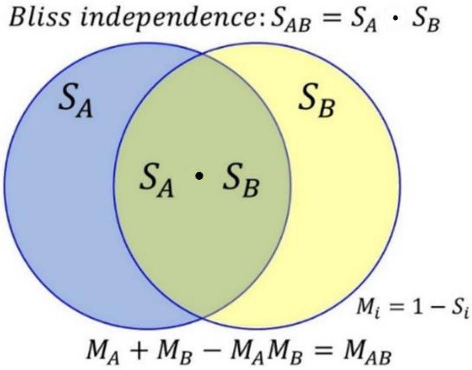

Figure 5.1. Graphical (Venn diagram) representation of Bliss's drug independence. Adapted from Ref. [168]

This model is particularly useful in analyzing drug combinations when the drugs act through different pathways or mechanisms. Since the survival fractions S are related to the corresponding mortality M by $S = 1 - M$, Bliss independence is usually expressed in terms of mortality,

$$M_A + M_B - M_A \cdot M_B = M_{AB} \tag{5.3}$$

The additive model by Loewe states that in the case of no interaction between drugs A and B, the drug combination with doses d_A and d_B leading to the same mortality M must satisfy the so called "median effect" equation[168]

$$\frac{d_A}{D_A} + \frac{d_B}{D_B} = 1 \tag{5.4}$$

where D_A and D_B are the individual doses of each drug iso-effective with the combination dose. In terms of the synergistic effects of these two drugs we can express it by the condition,

$$\frac{d_A}{D_A} + \frac{d_B}{D_B} \begin{cases} < 1 \rightarrow synergy \\ = 1 \rightarrow additivity \\ > 1 \rightarrow antagonistic \end{cases} \tag{5.5}$$

This additive model, based on dose reduction, is the basis for isobolographic plotting, a concept previously introduced by Fraser[169]. The main result of this model is that the combination of two drugs can result in any of the three effects described above, depending on the doses and therefore, it is important to characterize the entire cell viability range of both compounds.

In the context of cisPt and hyperthermia, synergy refers to the enhanced therapeutic effect achieved when these two treatment modalities are used together to combat cancer. When cisPt and hyperthermia are used in combination, a synergistic effect could occur. The rationale behind an expected synergistic effect relays on the fact that rising the local temperature through hyperthermia can increase the permeability of cell membranes, making it easier for cisPt to enter cancer cells. Also, hyperthermia can enhance the effectiveness of cisPt-induced DNA damage within cancer cells by accelerating reaction kinetics at higher temperature, while improving (*in vivo*) blood flow to the tumor to deliver cisPt more efficiently to cancerous tissue. As a result of these combined actions, the therapeutic efficacy of cisPt could be expected to be greater when administered in conjunction with hyperthermia than when used alone. Due to the large number of variables to be considered, only a few works have reached a preclinical stage or even *in vivo* studies. Therefore, as a necessary previous step, *in vitro* experiments are mandatory to shape the correct planning to meet the controls and statistics assay, functioning as a test that filters treatment, without losing the complexity of a living system.

Based on the above hypotheses, we performed *in vitro* experiments working with two types of cell line, BV2, a murine microglial cell, and PAN02, a mouse pancreatic epithelial cell line. **BV2** is a type of microglial cell derived from C57/BL6 murine [170] that are involved in phagocytosis and immune defense processes. This particular line was chosen for our research due to its significant phagocytic activity, which enhances the uptake of nanovector, as previously investigated by our group [171-173] thus providing a solid base for our initial *in vitro* assays. **PAN02** is a ductal adenocarcinoma model induced in the pancreas tissue of C57BL/6 male mice[174]. As the most prevalent form of pancreatic cancer in humans (that originates from the rapid proliferation of exocrine cells), the PAN02 model is particularly relevant in drug development due to its notable resistance to chemotherapy, especially cisPt. Consequently, PAN02 was selected as the ideal cell line to demonstrate the effectiveness of our novel nanovector LNC (synthetic magnetosomes loaded with cisPt) in a combined treatment approach involving MFH and CT.

This chapter will be divided in three parts. The first one dedicated to investigate the toxicity of the nanosystems synthesized: MNPs, synthetic magnetosomes (LN), liposomes (LB), cisPt encapsulated in liposome (LC) and LNC. The experiments were performed in two different cell lines, BV2 and PAN02, and the latter was used as a model for cytotoxic effects of the cisPt, since this is a cell model close to the pancreatic tumor model relevant for clinical applications. In a second part, we will study the MNPs internalization and biodistribution using the previously characterized system of $Zn_{0,2}Fe_{2,8}O_4$ MNPs with a sodium citrate shell and LN. Also, the uptake and biodistribution process of the nanosystems will be analyzed in detail, including commercial cisPt, LC and LNC. Finally, the evaluation of the combined CT-MFH treatment with the nanovector LNC on the PAN02 cell line would be performed.

5.2. Cell growth curve

In a cell culture, survival under specific conditions make possible the cell proliferation to ensure the next generation. A growth curve evaluates the growth rate of a cell culture under certain nutrient and space conditions. Figure 5.2 shows a typical curve that can be divided into four phases. In the first days, the cells are in a lag period (Figure 5.2), in this latency phase the density remain constant. In the next phase the cell will grow in an exponential way as long as the space and nutrients allow it (growth period in Figure 5.2). Finally, the number of cells maintain constant at the stationary stage. When the percentage of the culture flask is covered by around

90-100% of adherent cells some of them will die and for others the cell division will be reduced or even stopped. In this point, if we don't change the medium with new nutrients and the place, the cells will progressively die. Normally, in all our experiment we want to work between 70-90% of confluence in the well. Each cell culture has a characteristic cell grow curve, and doesn`t change if the cells are in good condition. In this curve we obtain a few generations of cell.

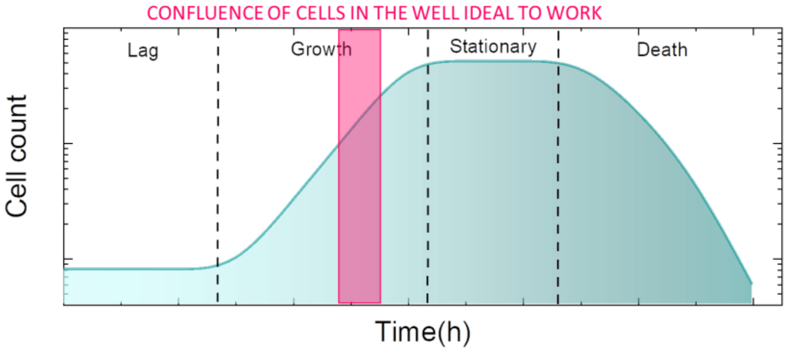

Figure 5.2. Schematic representation of cell culture growth as function of time.

The exponential behavior of the cell, in the growth region, can be described with the equation [175]:

$$N = N_0 2^g \tag{5.6}$$

where g is a time dependency parameter and represents the number of generations of cell. For example, the doubling time t_D is the time required for the cell to produce the next generation, in this case, $g = \frac{t}{t_D}$. The relevance of knowing the t_D value of our cell line is that from this time we can maintain our cell culture, plan experiments and make sure that the cell culture is fine, since this value would not vary in a healthy culture. To calculate the doubling time of our cell, we replace the g value in equation 5.6:

$$\log\frac{N}{N_0} = \frac{t}{t_D}\log 2 \tag{5.7}$$

$$\log\frac{N}{N_0} = k_{10}t \;\rightarrow\; k_{10} = \frac{\log\ 2}{t_D} \tag{5.8}$$

where k_{10} is a characteristic constant experimentally obtained for each cell culture.

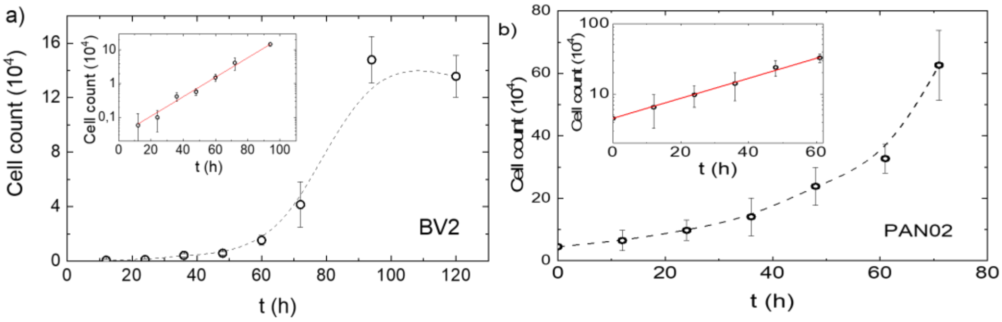

Figure 5.3. a) Cell growth rate for BV2. Inset: the semilogarithmic fitting of the exponential growth cell count yielding a cell doubling time t_D= 10,4 h. b) Cell growth rate for PAN02. Inset: the semilogarithmic fitting of the exponential growth cell count yielding a cell doubling time t_D= 20,1 h.

The doubling time obtained for BV2 cells was 10,4 hours (Figure 5.3 a) and 20,1 hours in the case of PAN02 cells (Figure 5.3 b). Both cell line have a lower doubling time compare with bibliographic results, 24 h BV2 and 61 h PAN02[176]. Some deviation could be introduced due to difference in medium and complements, as well as variation in temperature or percentage of carbon dioxide.

5.3. Toxicity assay

One of the main considerations to perform toxicity experiments with a multi-component system (i.e., lipids, cisPt, MNPs and MFH) is that for different experiments the dose of the studied component must be standardized for each system. For instance, when the toxicity of cisPt concentration was studied, all calculations were referred the cisPt concentration disregarding the amount of lipids or MNPs in the system. In the case of lipids, for the liposome control, the formulation with higher lipidic concentration was used as reference. The concentrations of CisPt encapsulated in our LNC nanovector was high compared to the concentration required to kill 50% of a cell culture (typically referred to as the IC50, half-maximal inhibitory concentration). Therefore, to maintain acceptable values of CisPt compatible with MFH effects, the necessary volumes of LN were added to complete the MNPs concentration. The volume of treatment added to cells was never greater than 10% of the volume of the well worked, to avoid cellular stress.

Cell viability of BV2 and PAN02 cell lines was studied in co-cultures with MNPs and LN with increasing concentration (from 12,5 to 200 µg/mL) at 12 hours of incubation for BV2 and at 48 hours for PAN02. Viability analysis was performed by Tripan Blue (TB) assay for BV2 and flow cytometry for PAN02 (details of these techniques are given in Chapter 2). Figure 5.4 shows the toxicity results where no toxicity effects were observed in any cell line due to the lipid coating. With less than 10% of cell death at the highest concentration 200 µg/mL and the maximum incubation time of 48 hours, no toxicity effects were observed due to MNPs or LN.

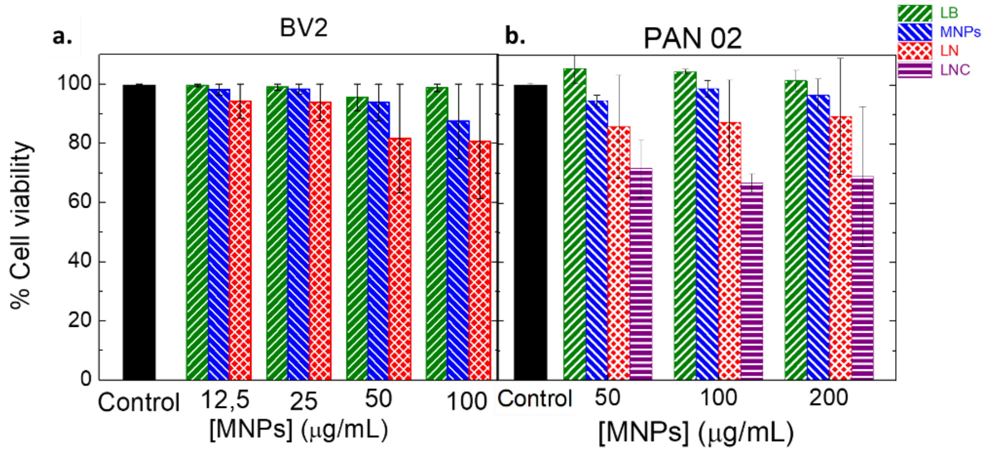

Figure 5.4. a) Cell viability of BV2 carried out by TB exclusion assay. The cells were incubated with LB, MNPs and LN from 12,5 to 100 µg/mL of MNPs, and the respective liposome concentration, for 24 hs. b) Cell viability of PAN02 carried out by Flow cytometry assay. The cells were incubated for 48 hs. with LB, MNPs and LN from 50 to 200 µg/mL of MNPs, the respective liposome concentration and a fixed value of 5uM for CisPt in the case of LNC.

To assess the toxicity of MNPs, cell viability was studied by flow cytometry in the case of LNC nanovector, varying the concentration of MNPs from 50 to 200 µg/mL, incubated for 48 hours with a fixed cisPt concentration of 5 µM. Figure 5.4b shows that there is no detectable variation in cell viability with increasing MNPs, within experimental error. The observed error bars deviation is larger in all cases involving LN and LNC might be due to the agglomeration of the LN nanosystem during co-cultivation that makes very difficult the cell counting protocol. This phenomenon does not occur when working with LB or MNPs.

Regarding the toxicity effects of cisPt, as one widely used chemo drugs for the treatment of different types of cancer, they have been extensively studied [177]. The toxicity levels of cisPt in the pancreatic cell line PAN02 was evaluated by flow cytometry 48 hours after the application of: the drug alone (commercial cisPt), the LC nanosystem (with their respective lipid concentration) and LNC (with a constant value of 50 µg/mL MNPs), for the range of 1 to 10 µM cisPt. As expected, an increase in cisPt concentration enhanced the cell death in all three treatments (Figure 5.5)). The toxicity of the nanosystems showed a similar trend but more effective cytotoxic action with respect to the free cisPt. The LN and LNC system showed similar toxicity values, confirming the low level of toxicity of MNPs. With these results, we decided to establish a concentration of 1µM of cisPt for the subsequent synergy evaluation of the cisPt and MFH.

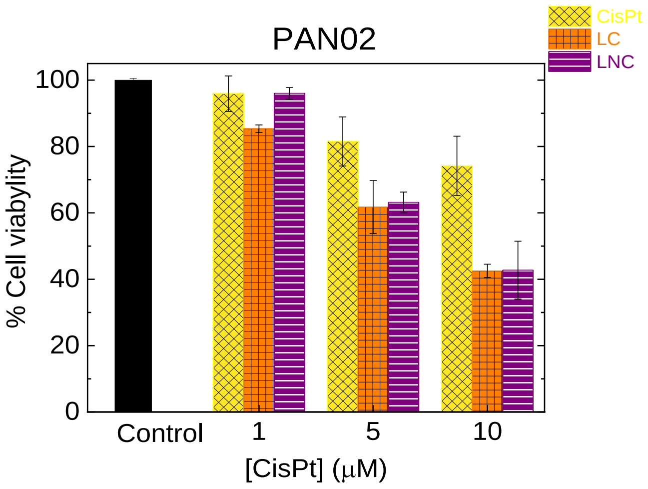

Figure 5.5. PAN02 viability, performed by flow cytometry after 48 hours of co-cultivate with different CisPt concentration from 1 to 10 µM for commercial CisPt (yellow and black dots), LC (orange with dark square) and LNC (violet with black straight) with a fixed value of 50 µg/mL of MNPs. In black the negative control.

5.4.Cell uptake: time evolution and intracellular distribution of nanovectors

Previous work carried out in our group [178] has shown greater efficiency in cell death by intracellular temperature increase of MFH, compared to water bath(exogenous heating). For this reason, it has been decided to carry out MFH experiments only with internalized systems and those that interact with the cell membrane. The temporal evolution of the internalization of the nanocarriers has been evaluated for a fixed concentration of 200 µg/mL of MNPs for 2 to 6 hours. Different techniques were used for quantification of the uptake, based on the determination of intracellular iron contents, explained in chapter 2. In the case of BV2 we used UV-vis spectroscopy to measure the formation of the Fe-ammonium thiocyanate complex. For PAN02 cells, atomic emission spectroscopy was used. For both techniques, calibration curves were performed using cells without MNPs as control to remove the basal iron from the cells. Nevertheless, this contribution was negligible.

The amount of MNPs and LN internalized in both cell lines, in units of pg/cell, showed remarkable differences, as shown in Figure 5.6, with higher internalization efficiency observed for the LN nanovector. The maximum internalization rate was 72 pg/cell reached by BV2, in contrast to PAN02, which internalized a maximum of 35 pg/cell, this difference may correspond to the different phagocytic function of each cell line. For the naked MNPs, a maximum internalization of ≈30 pg/cell was reached in both cell lines. A saturation of the internalized amount of nanosystems was observed after 2 h and 4 h of co-culture in BV2 and PAN02, respectively.

As a general result from all uptake experiments, it was observed that lipid-containing systems (LN and LNC) improved cell uptake, notably in BV2 cell line. This can be explained by the interaction of the nanosystems with cell membranes, since lipid coatings on nanoparticles or the use of liposomes create structures that closely resemble the natural lipid bilayer of cell membranes. This similarity makes it easier for these nanoparticles to interact with and fuse into the cell membrane and can undergo lipid-lipid interactions with the cell membrane. This camouflage with the cellular environment allows the LN and LNC vectors to merge with the cell membrane, facilitating their incorporation into the cell. In the case of the more phagocytic BV2 cell line, where the largest difference was observed, it is well known that lipid coatings can enhance the endocytic pathways, leading to the internalization of both the liposomes and any cargo they may carry, including MNPs. A stabilizing effect by the lipids on the colloidal systems cannot be ruled out when explaining this difference, since as we observed in Chapter 3 lipid coatings provided more stability to the nanoparticles. This stability could have a size-related impact during the interaction with the cell membrane.

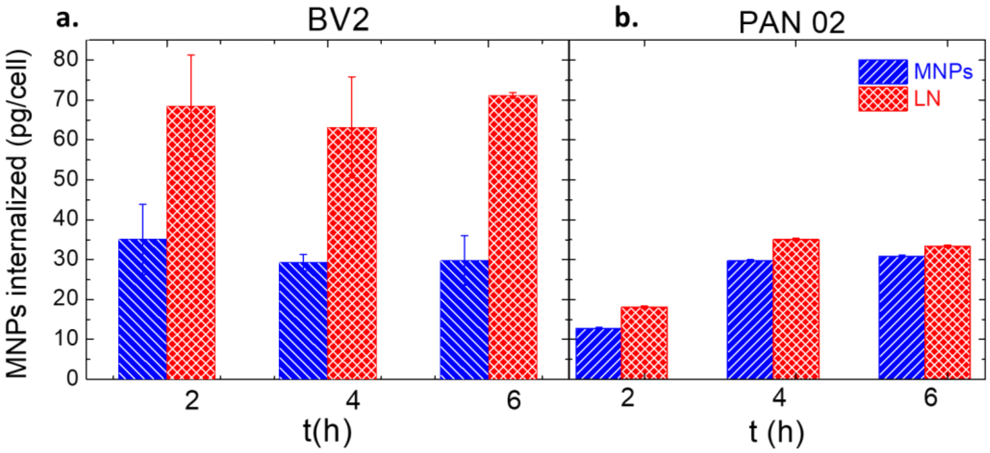

Figure 5.6. Time evolution of the amount of internalized MNPs (blue bars) and LN (red bars) in BV2 cell line (left panel) and the PAN02 cell line (right panel).

Additional investigation into the interactions between nanocarriers and cells, as well as the subsequent distribution of these nanosystems within the cells, was conducted using transmission electron microscopy (TEM). To achieve this, a meticulous sample preparation protocol was tailored to accommodate the diverse properties of the various nanosystems. In a general procedure, cells were co-incubated for a duration of 6 hours, followed by fixing, staining, and embedding the samples in EPON® epoxy blocks, as detailed in Chapter 2, to facilitate electron microscopy analysis.

In general, after nanovectors uptake, both cell lines exhibit the presence of viable cells that maintain their typical morphology. Specifically, BV2 cells retain their rounded shape, while PAN02 cells assume an oval configuration. The nanovectors were predominantly located within the cytoplasm or at the extracellular space, with no evident interaction observed with the cell nucleus. To initiate the examination of nanosystem uptake outcomes, the TEM images subsequent to the co-incubation of BV2 cells with LB were subjected to TEM analysis (Figure 5.7.b and c). In the case of LB samples, a clear hallmark was the presence of bright vesicles along the cell cytoplasm, filled with dark spots. The assessment of the average size of the dark spots within the vesicles was carried out by analyzing the histogram plot and fitting it with a Gaussian distribution (Figure 5.7.d.). This analysis yielded an average diameter of approximately $d = (174 \pm 11)\ nm$, consistent with the hydrodynamic diameter of ($d = 165 \pm 20$) nm previously determined for blank liposomes in the as-prepared LB sample. This similarity suggests that the lipid layer of the liposomes did not undergo fusion with the cell membrane during the process of cellular uptake.

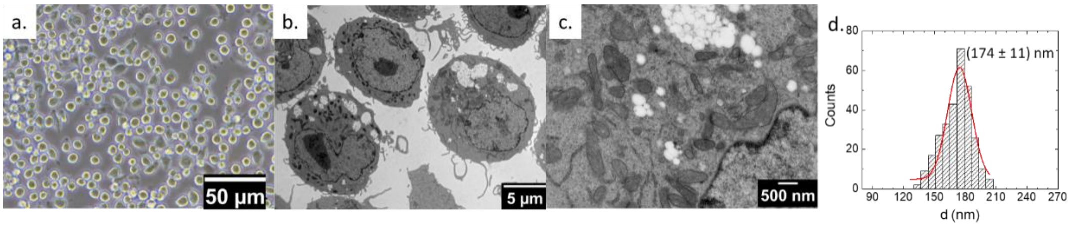

Figure 5.7.BV2 cell with liposome after 6h of seed. a) Image of optic macroscope of BV2 cell with 6h co-cultivated liposome. b) TEM image of contrasted BV2 cell in resin block. c). A Higher magnification TEM image of internalized liposome. d). Size distribution of the liposome internalized with a Gaussian distribution d= (174 ± 11) nm.

From optical microscopy images, Figure 5.8 and Figure 5.9, we observed a divergence upon the co-culturing of cells with various treatments. When considering the case of MNPs, a clear presence of numerous particles within the cellular cytoplasm becomes apparent. Interestingly, despite the intracellular presence of MNPs, the cellular morphology and distribution remains remarkably akin to that of the control group. This observation suggests that while MNPs are effectively internalized by the cells, they do not significantly disrupt or alter the overall cellular functionality. In contrast, in the case of LN, within the cellular interior LN entities are readily observable. However, the notable aspect is the visual clustering of cells themselves, resulting in an uneven or inhomogeneous distribution. This clustering phenomenon suggests that the presence of LN within the cells may be influencing their spatial arrangement or intercellular interactions, potentially leading to alterations in cell behavior or organization. The contrast between MNPs and LN in terms of their impact on cellular behavior and distribution underscores the importance of considering the specific effects of different nanosystems on cellular dynamics.

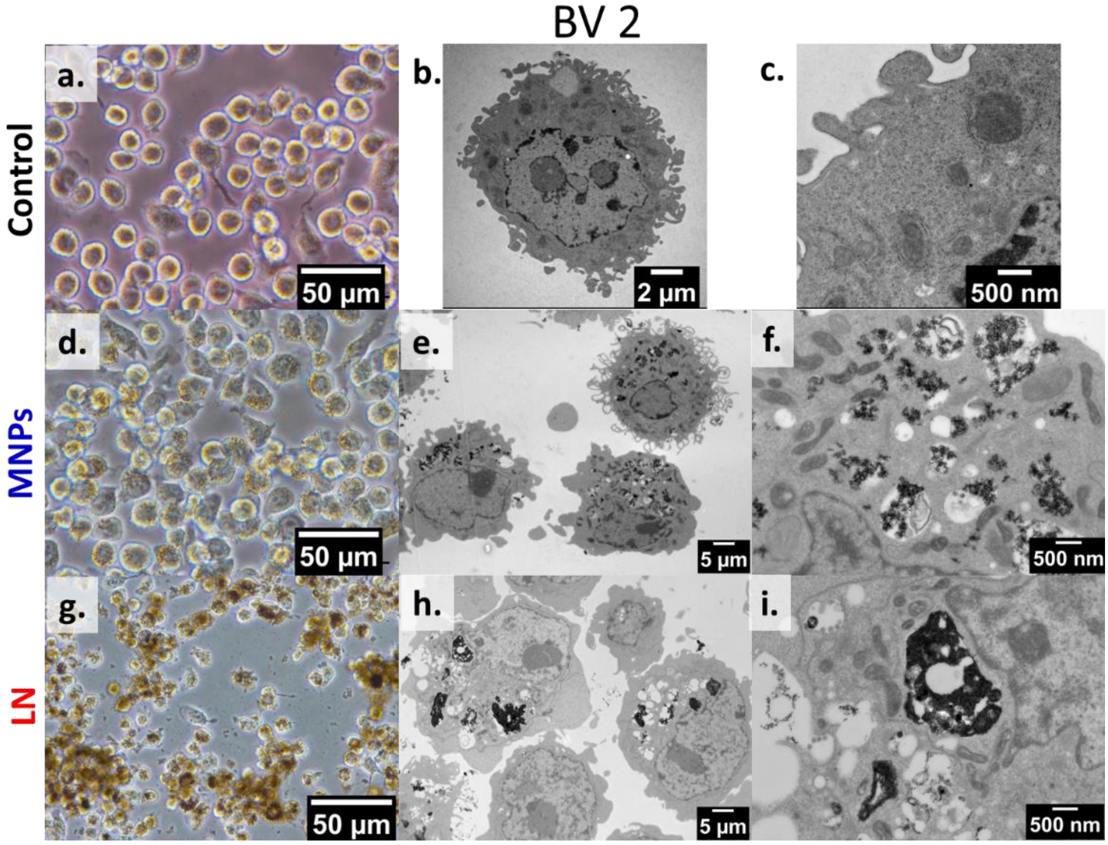

Figure 5.8. BV2 cell line a) control image of optic macroscope. b) TEM image of contrasted cell in resin block. c). A higher magnification of TEM image. BV2 after 6h of MNPs seed, d) Image of optic macroscope. e) TEM image of contrasted cell in resin block. f). A higher magnification of TEM image of internalized MNPs. BV2 cell line after 6h of LN seed, g) Image of optic macroscope. h) TEM image of contrasted cell in resin block. i) A higher magnification of TEM image of internalized LN.

In all TEM images, Figure 5.8 and Figure 5.9, vesicle formation was visible for both cell lines, indicating that BV2 and PAN02 endocytosed MNPs and LN. In the case of BV2, much more vacuoles with MNPs and LN were observed compared to PAN02, a result we have already noted during internalization experiments. In the case of PAN02, a high extracellular interaction with the formulations was evident, with some remaining on the cell surface. A random distribution of MNPs was not observed in both cell lines, instead they distributed in vesicles with agglomerates MNPs. In the case of LN, the endosomes were larger, and the LN maintain their arrangement of MNPs.

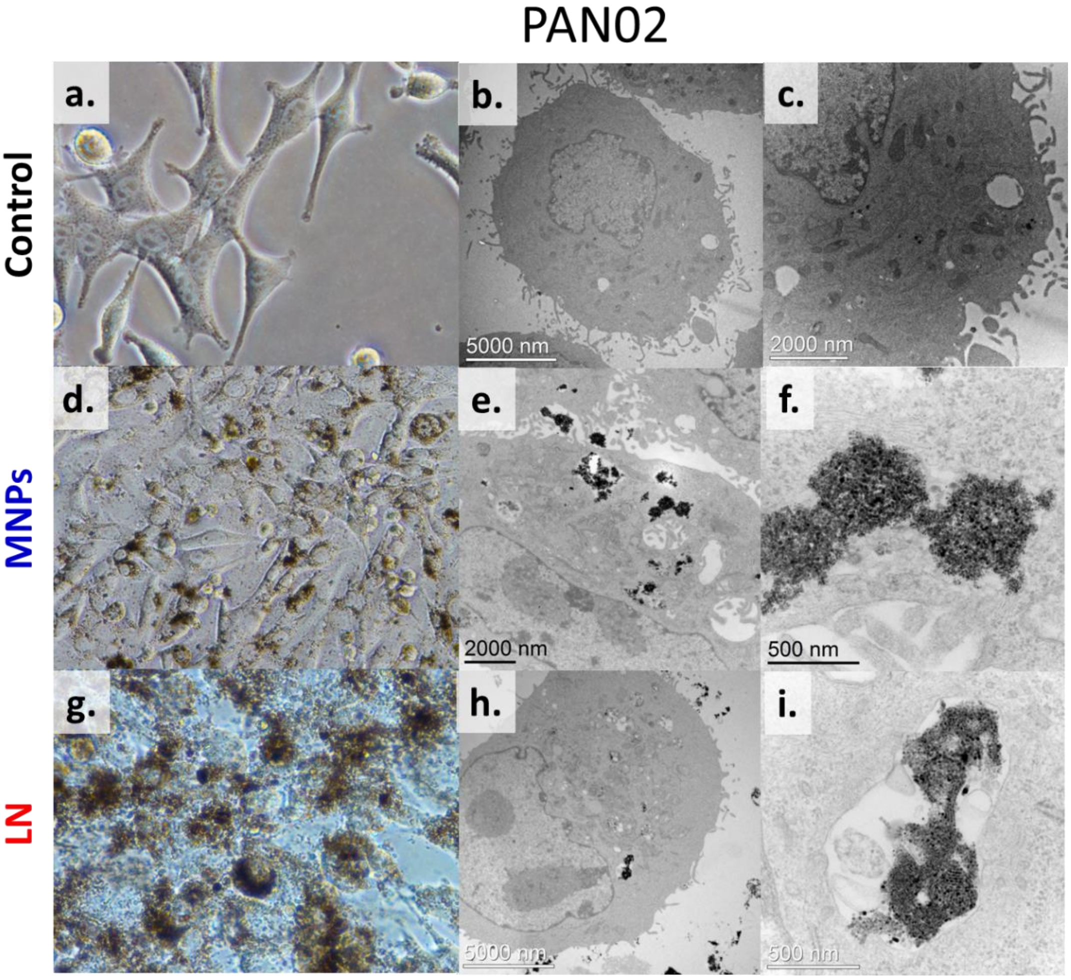

Figure 5.9. PAN02 cell line a) control image of optic macroscope. b) TEM image of contrasted cell in resin block. c). A higher magnification of TEM image. PAN02 with MNPs after 6h of seed, d) Image of optic macroscope. e) TEM image of contrasted cell in resin block. f). A higher magnification of TEM image of internalized MNPs. PAN02 cell line with LN after 6h of seed, g) Image of optic macroscope. h) TEM image of contrasted cell in resin block. i) A higher magnification of TEM image of internalized LN.

5.5. Internalization roads and fate of CisPt

From the optical microscopy images Figure 5.10, no differences were observed when cells were incubated with cisPt and LC. However, in the case of cells incubated for 6 hours with LNC, the nanocarriers, with their large size (≈ 530 nm) and higher contrast of the MNPs, were observed throughout the entire cell cytoplasmic space. Corresponding TEM images from contrasted resin blocks showed no difference between control PAN02 cells and those after 6 hours of incubation with commercial cisPt. This lack of difference was attributed to cisPt being internalized through the membrane (direct translocation) into the cell and not endocytosed, leading to the absence of observed vesicles. As explained in Chapter 1, recent studies suggest that the major copper influx transporter Ctr1 is utilized by the cell for Pt entry into the cytoplasm [179], while copper efflux transporters ATP7A and ATP7B regulate cisPt efflux[51].

In contrast, TEM images of resin blocks of PAN02 cells after 6 hours of incubation with LC and LNC exhibited the formation of vesicles in the cell cytoplasm filled with contrasted liposomal structures. This indicates that the lipid compounds were endocytosed by the PAN02 cell line. This result was significant and differs from approved clinical formulations like Lipoplatin®, where the liposome fuses with the cell membrane, releasing its drug into the cytosol[180]. This discrepancy may be attributed to the mixed composition of the sample formulation (see Table 3.5.). Lipoplatin is a fusogenic liposome mainly composed of dipalmitoyl phosphatidyl glycerol (DPPG) and methoxypolyethylene glycol-distearoyl phosphatidyl-ethanolamine (mPEG2000-DSPE), both lipids favoring liposome-cell membrane fusion. In our case, despite the use of pegylated lipids (18:0 PEG2000-PE), our formulation was predominantly composed of non-fusogenic lipid DPPC and cholesterol, imparting rigidity to the lipid membrane. This suggests that the drug was still encapsulated in liposomes and has not been released yet.

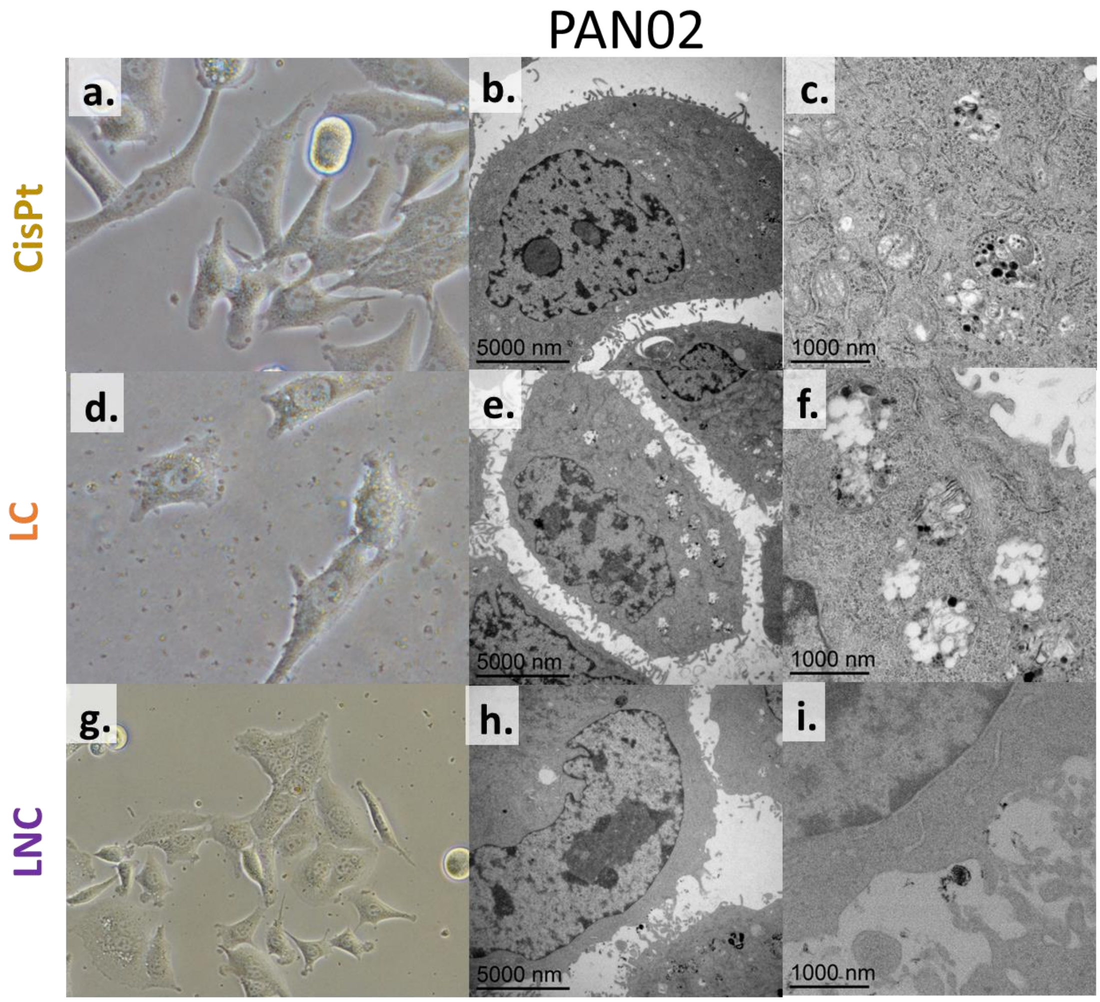

Figure 5.10. PAN02 cell line with CisPt after 6 h of seed, a) Image of optic macroscope. b) TEM image of contrasted cell in resin block. c). A Higher magnification of TEM image. PAN02 cell line with LC after 6 h of seed, d) Image of optic macroscope. e) TEM image of contrasted cell in resin block. f). A Higher magnification of TEM image of internalized liposome. PAN02 cell line with LNC after 6 h of seed, g) Image of optic macroscope. h) TEM image of contrasted cell in resin block. i). A Higher magnification of TEM image of internalized LNC.

Lipid formulations demonstrate higher efficacy in internalization compared to the free drug, not only because they utilize different pathways for internalization but also due to the higher concentration of the drug in the lipid/hydrosoluble compound. Using Atomic Emission Spectrometry (AES), the concentration of cisPt internalized by the cell was quantified for different systems, starting from a concentration of 50 µM (1,8 mg lipid and 0,11 mg MNPs, for the case of LC and LNC), and co-cultured for 2 to 6 hours. Details of the experimental procedure were explained in Chapter 2. In Figure 5.11, the results revealed a significant difference between the uptake of 'free' cisPt (<1 pg/cell of Pt) and the case of LC and LNC nanosystems, where values up to 3,5 pg/cell were observed. This enhanced internalization of LC and LNC compared to commercial cisPt was attributed to the lipid encapsulation of the drug, improving its solubility. Interestingly, the uptake dynamics were different: while cisPt and LC incorporation appeared to reach its maximum after 4 hours, the incorporation of LNC seemed to continue growing after 6 hours. However, additional experiments for longer durations would be needed to confirm this trend.

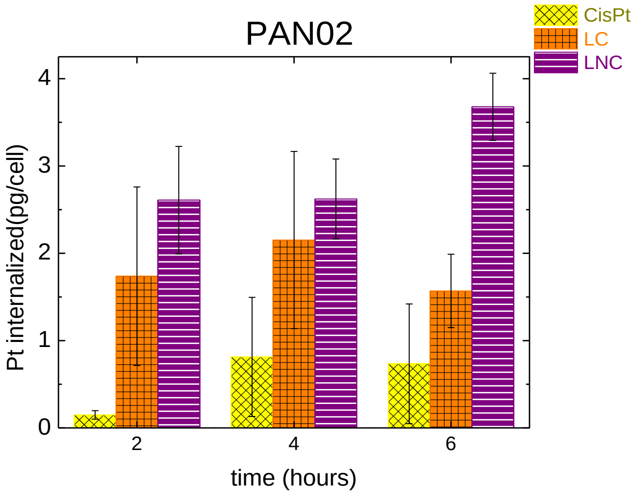

Figure 5.11. PAN02 cellular Uptake of commercial CisPt (yellow with black dots), LC (orange with black square) and LNC (violet straight), as function of incubation time adding 50 µM of CisPt.

In the first two hours of the experiment, no cell death was observed. After 6 hours, cell death represented less than 3% of the population. Consequently, we can conclude that, although cisPt was internalized by the cell, the 6-hour duration was not sufficient for the PAN02 cell line to experience cell death due to the action of the 50 µM cisPt.

A complementary set of experiments was performed to quantify cisPt in PAN02 cells using electron energy loss spectroscopy (EELS) and energy-dispersive X-ray spectroscopy (EDS) on the contrasted resin blocks. Figure 5.12 displays the EELS mapping, and Figure 5.13 shows the EDS spectrum corresponding to the TEM image area. Unfortunately, we were unable to observe the presence of Pt with these techniques, despite the presence of contrast elements U (from Uranyl Acetate), Os (from Osmium tetroxide), and Pb (from Lead citrate), which are used for contrast. The inability to quantify Pt encapsulated in cells is likely due to the molecular dispersed solution form of cisPt. This means that EELS and EDS techniques were not suitable methods for this analysis.

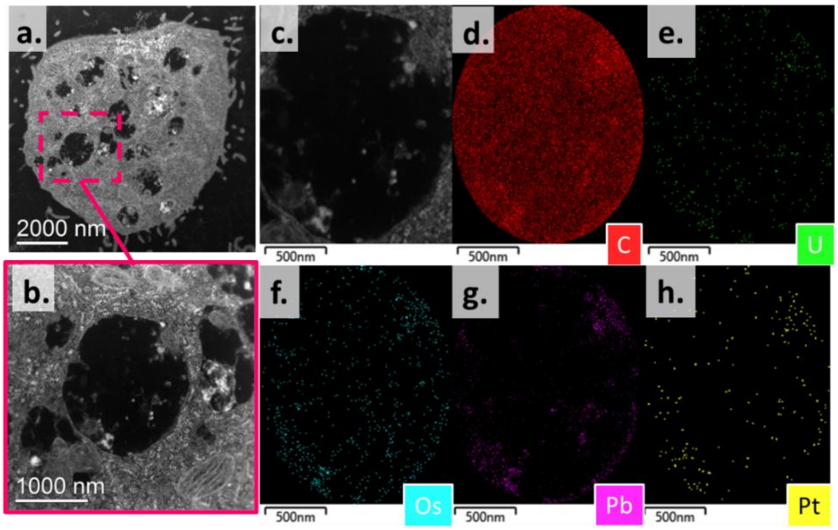

Figure 5.12. a) TEM image of contrasted resin blocks of PAN02 cells line with LC (5 µM) after 6 hours of co-cultivated b) a higher magnification of TEM image of internalized LC. C)Region of interest where elemental mapping was performed by EELS-SI (d) C in red, (e) U in green, (f) Os in cyan, (g) Pb in pynk and (h) Pt in yellow.

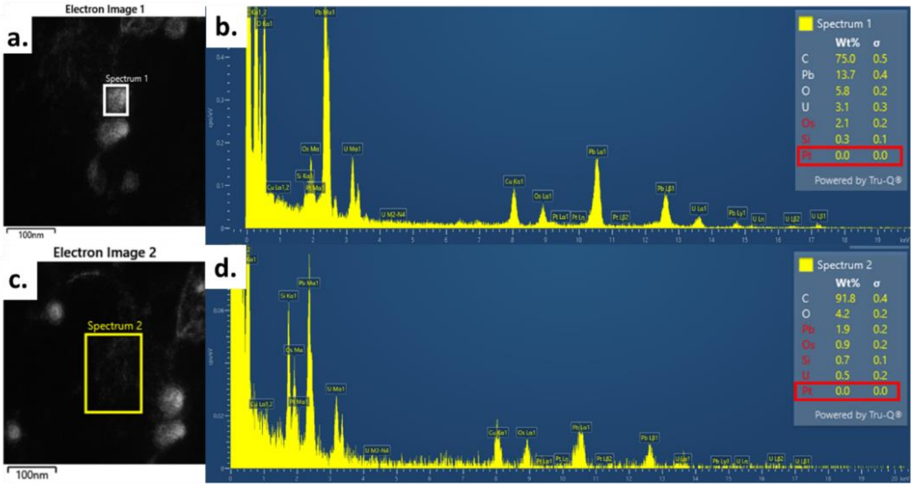

Figure 5.13. a) and c) High magnification of TEM image with the region of interest to analyze.b) and d) EDS spectrum of the respective region of interest, with the relative cuantification of elements. Percentage of Pt is zero in both spectra.

5.6.Synergistic effect of MFH+CT treatment

To assess the potential synergy effects of *simultaneous* MFH adjuvant therapy to CT using our LNC nanovector, the first step was to select the optimal conditions for the combination of treatments, i.e., the region of cell viability close to IC_{50} that granted a workable viability amount for all experiments to be performed. To this end, we used a water bath as an external heating (EH) source to characterize the impact of thermal dose on PAN02 cells and analyzing the viability *after 72 h post treatment* with a presto blue (PB) staining fluorometric assay explained in Chapter 2. We note that this was only an approximation to the actual MFH conditions to be used, since previous research [178] reported that MFH has a more pronounced impact on the cell viability than EH treatments. In any case, the preliminary assessment of thermal tolerance by this strategy proved to be fairly accurate in defining the MFH conditions of target temperature and time (see below).

5.6.1. Thermal effect on cell viability

The temporal evolution of cell viability after EH treatments within the temperature range of $41°C$ £ T £ $46°C$ and times $5\,min \leq t \leq 45\,min$ (Figure 5.14) revealed very low cell viability for T > 44°C after t 10 min. Applying EH treatments at temperatures 41°C and 42°C yielded significant time dependence of the cell viability, ranging from ≈100% after 10 min to ≈40-50% for 45 min. Higher EH temperatures showed the expected decrease of the overall viability, keeping a similar time dependences that for lower temperatures. For EH application at $T = 45 - 46°C$, very low cell viability was observed after 10 min of treatment, making these range unsuitable for analyzing any synergistic effect. The overall time and temperature dependence of cell viability aligns with the expected response from thermotolerant cells. Since the measurement was conducted 72 hours after the experiment, we are capturing the subsequent generation of cells resistant to this temperature. From the previous results, we selected the $39°C$ £ T £ $43°C$ temperature range for $t = 10$ min as the workable window to measure any synergistic effects of MFH and CT therapies.

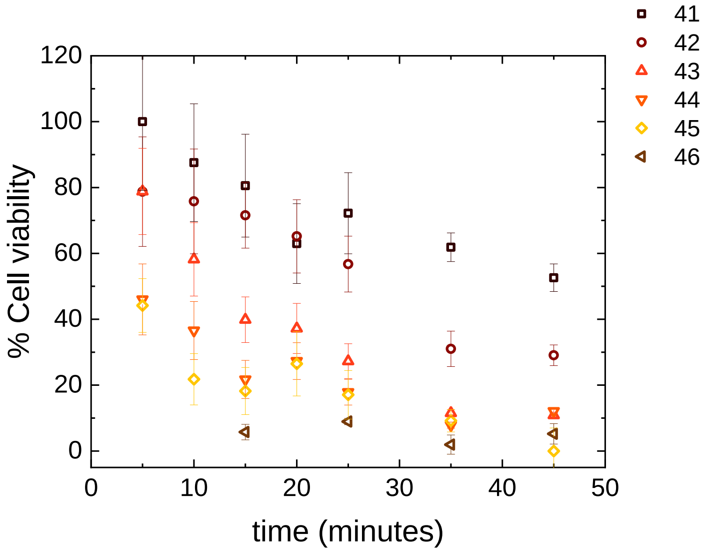

Figure 5.14. Time evolution of cell viability in PAN02 after 72 hours of the EH hyperthermia experiment. Measured from fluorimetry by PB technique, in the range of 41 to 46 °C.

5.6.2. MFH treatment

After the previous setting of optimal thermal conditions, ac magnetic fields ($f = 568\,kHz$) were applied to a 200 µL pellets in a chromatography vial with a fiber optic thermometer centered to measure the temperature increase by the MNPs, LN and LNC nanovectors, and the PID temperature control was adjusted to maintain the target temperature for $t = 10\,min$. Figure 5.15 illustrates a typical curve for this type of experiment, where the time dependence of the temperature (black) and the applied magnetic field (cyan) are shown. Three important regions can be distinguished:

1. Region I. Warm-up region: the time interval where the maximum magnetic field amplitude H_0 is applied to rise the temperature to the target value.

2. Region II. Adjustment region: a short time interval where the PID controller modifies the H_0 to stabilize the at the target (setpoint) value of temperature.
3. Region III. Treatment region: characterized by the application of low H_0 values enough to maintain and stabilize the temperature at the setpoint value.

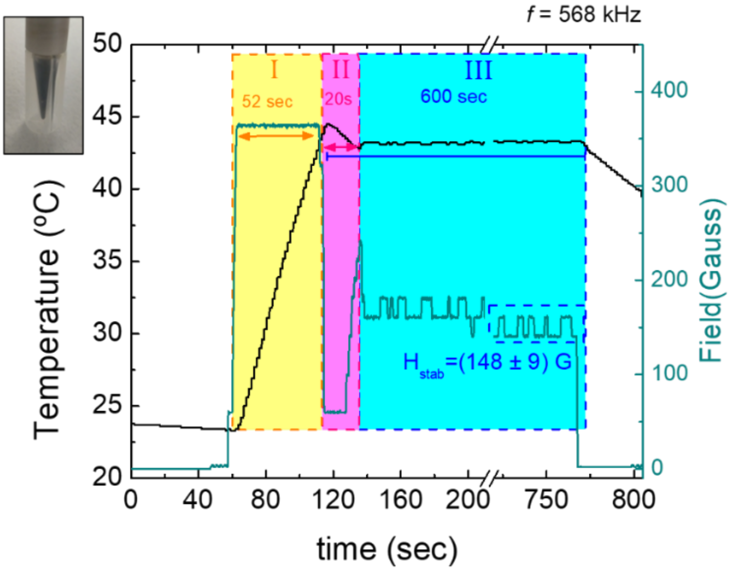

Figure 5.15. Typical heating profile T vs. time to provide 10 min at constant target temperatures under magnetic field ($f = 568\ kHz$). Inset: image of the sample containing PAN02 cells with the nanovector, after the MFH experiment, showing stability with no evidence of precipitate in the pellet.

All treatments were designed to apply a therapeutic dosage time $t_D = 10$ min at constant target temperature (T_{target}), under ac magnetic field ($f = 568\ kHz$). Given the high SLP values in the samples, the initial steep rise in temperature (region I) and short time for stabilization (region II), in all cases the total transient time t_{tr} until T_{target} was attained was $t_{tr} \approx \frac{t_D}{10}$, with an excellent reproducibility of the heating response from all samples. This reproducibility was originated in the detailed standardization protocol to achieve a precise concentration for a given nanovector test in all samples. More important, it can be seen from the profiles (Figure 5.16) that in all instances the overheating beyond the target temperature (region II) was less than 3°C, avoiding undesired cell death from higher temperatures in this short time. In region III, it can be also observed that during the treatment at T_{target} (Figure 5.16) the field amplitudes (H_{stab}) required to stabilize the target temperature during the treatment time t_{tr} for LN and LNC samples were very similar, while it was somewhat higher in the case of MNPs. These differences could be originated in the higher internalization of LN and LNC by the cells, resulting in a larger effective concentration of magnetic material in the measured cell pellet.

The previous results on the temperature profiles hold significance concerning the total thermal dose during hyperthermia experiments. Understanding the concept of thermal dose is crucial in clinical settings, as the time required to reach a target hyperthermic temperature, as well as overheating transients during temperature-control, can significantly impact the overall treatment effect. A precise knowledge of the temperature-profile like we produced is essential to establish an accurate estimate of thermal dosage as the first step for testing combined treatments. In our initial attempt to calculate the thermal dose, we consider the integral of temperature over time. We calculated that the dose acquired during the warm-up and transition phases (regions I and II in Figure 5.16) accounts for less than 5% of the total treatment dose across all cases. This might not appear significant at first glance, given the high absorption capacity of our system, which is not typically observed. However, it becomes more relevant when we refer to Figure 3 in the study conducted by Sapareto and Dewey.[26] In this figure, it is evident that the warm-up phase of the treatment has durations exceeding 10 minutes, highlighting the importance of this observation.

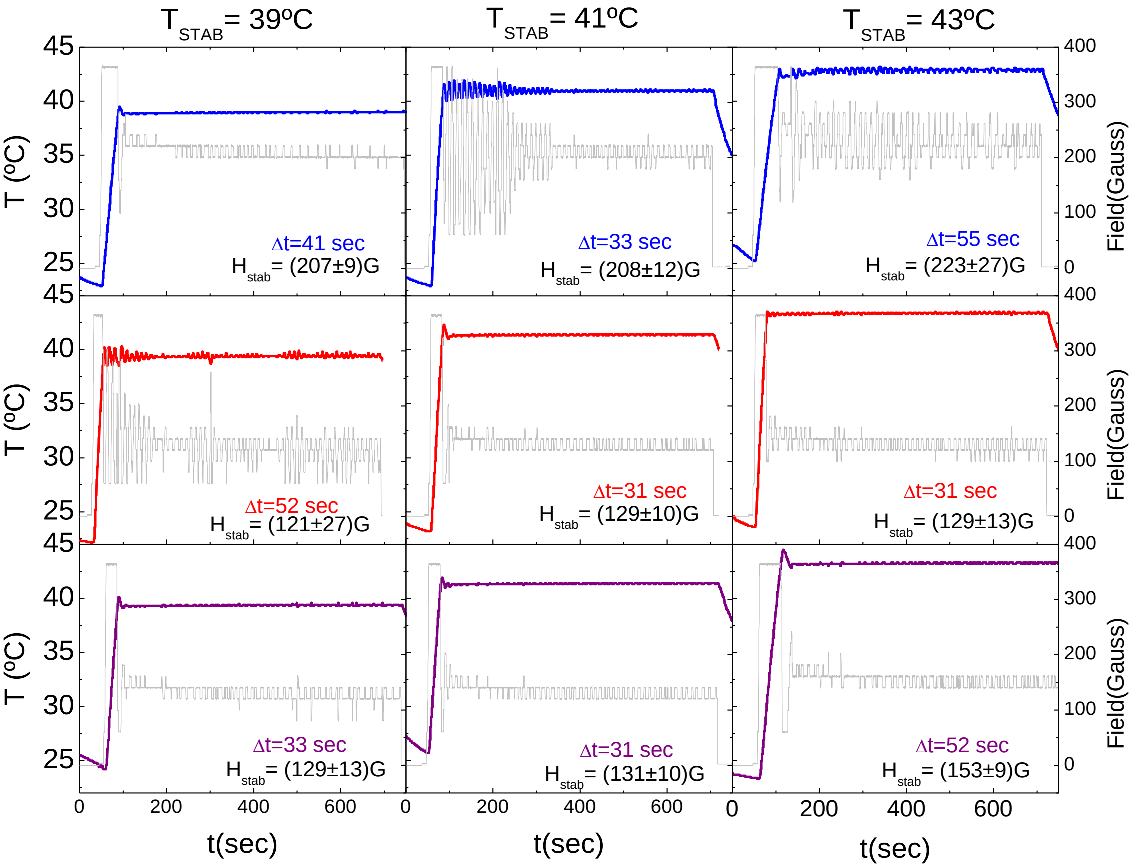

Figure 5.16. Temperature and magnetic field profiles recorded during the experiment for MNPs, LN and LNC, at the treatment temperatures 39°, 41° and 43° C.

5.6.3. Combined effect of MFH + CT: Synergy

Figure 5.17 presents the results from a flow cytometry assay conducted over a 48-hour period following a 10-minute treatment at 39°C, 41°C, and 43°C. The magnetosomes (LN) showed similar toxicity at the lower temperature range compared to MNPs. At T≥41°C the cell death effects of MNPs increased, most likely due to temperature-induced production of reactive oxygen species (ROS) at the MNP's surface that can trigger apoptotic cell pathways. The free radical production at MNPs surfaces is a well-known mechanism [181] and has been reported for many different nanostructured materials.[173], and moreover it has a temperature dependence with a maximum of ROS production at temperatures close to 43°C. Accordingly, Figure 5.17 shows a lesser and constant toxicity of LN at higher temperatures, indicating that this mechanism was partially prevented in the lipid-coated particles of LN samples. The LNC system showed a larger toxicity than the other two at all temperatures, notably increasing its effectivity for T > 40 °C. We therefore analyzed whether this larger effect in LNC corresponded to an additive or synergistic mechanism of cisPt and hyperthermia.

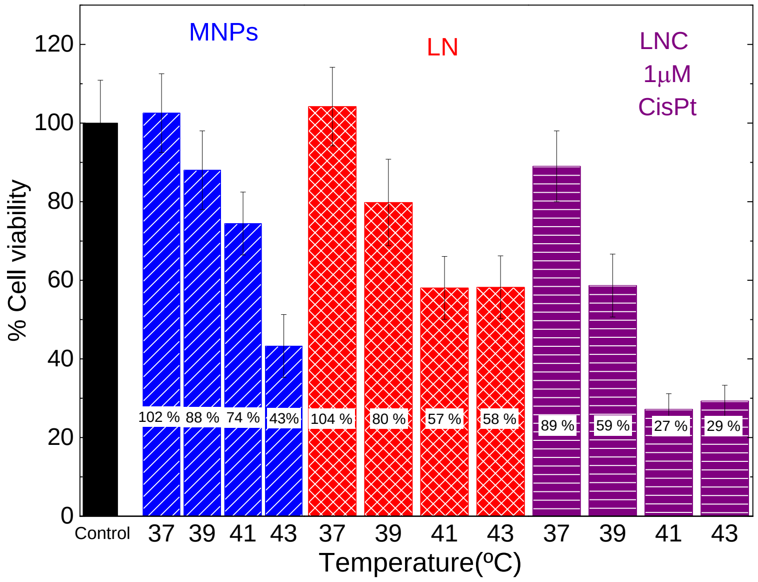

Figure 5.17. Cell viability assay by flow cytometry of the synergic experiments. At left the controls, and in the right the viability after 48 hours of the hyperthermia experiment in function of the treatment temperature.

Considered that $f_i = \frac{100-(\%\,cell\ viability)_i}{100}$ we use the Bliss model defined in equation 0.1, to calculate the co-treatments influence. Data in Table 5.1, confirm the synergic effect for the three temperature treatments.

The limited number of experiments conducted may not provide sufficient data to fully assess the impact of the nanovector LNC under the Lewis model. However, it was feasible to evaluate the outcomes for the lowest treatment temperature. We determined the thermal dose by employing the concept of equivalent minutes at 43 degrees Celsius dose (t_{CEM43}), as defined by Dewey and Sapareto in Chapter 1, and as further elaborated upon in this chapter. This calculation assumes a constant value of R=0,25 for temperatures below 43°C and incorporates it into equation 5.5,

$$\frac{d_A}{D_A} + \frac{d_B}{D_B} \approx \frac{1\,\mu M}{5\,\mu M} + \frac{0{,}15\,min}{0{,}25\,min} = 0{,}44 < 1 \ \rightarrow \text{synergy} \tag{5.9}$$

these results were congruent with the result treated with Bliss model (Table 5.1).

Table 5.1. Evaluation of the combined effect of the MFH-CT treatment with LNC internalization using 1 μM of cisPt (treatment A) at different hyperthermia temperatures (treatment B) for PAN02 cell line according to Bliss method.

CisPt (μM)	T (°C)	f_A (relat %)	f_B (relat %)	f_{AB} (relat%)	Effect
1	39	0,11	0,2	0,41	Synergy
1	41	0,35	0,42	0,73	Synergy
1	43	0,35	0,42	0,71	Synergy

As an additional comment on the effect of particles on cellular structure, we have investigated the condition of the cell morphology and structure after the MFH and combined experiments. As can be seen in the TEM images of Figure 5.18 for post-treated cells embedded in resin blocks after MFH treatment, the presence of apoptotic bodies and the rupture of the cell membrane was evident, as well as the presence of nuclear fragments, all of which indicate apoptotic/necrotic cell death. We emphasize that, even after the MFH treatments producing great cell structural damage, the nanoparticles' arrangement already present in the nanovectors within the cell remains intact. This may suggest greater stability of our nanoparticle vector, which could also help minimize toxic effects after MFH.

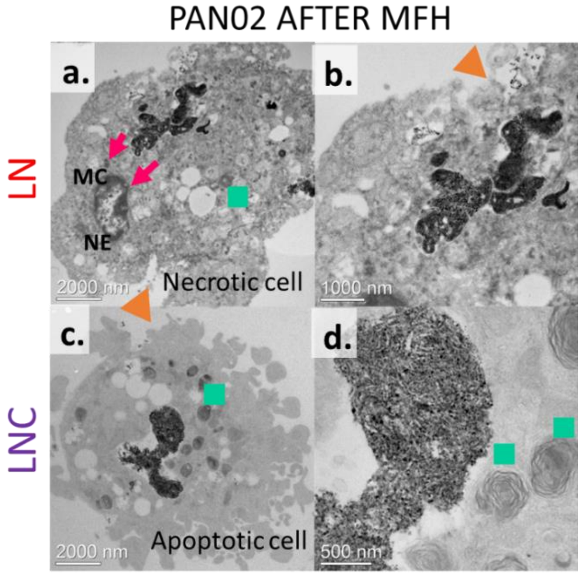

Figure 5.18. TEM image of PAN02 cell after magnetic hyperthermia with LN and LNC. a) Necrotic cell with LN c) Apoptotic cell with LNC. b) and d) zoom of the vesicle containing the LN and LNC treatment, respectively, showing that the arrangement of curved chains is maintained after MFH treatment. We can distinguish residual body (cyan square), nuclear fragments (pink arrow), nuclear environment (NE), marginal chromatin (MC) and rupture of plasmatic membrane (orange triangle).

5.6.4. The 'Universal' thermal dose curve

A crucial requirement in the field of MFH for oncological treatment is a clear definition of the thermal dose, which allows to develop adaptable and user-friendly therapeutic systems to facilitate the transition from laboratory research to real-world application. Since the purpose for any definition of dose is to provide a number which relates to a specific biological response, the definition for our study with adjuvant mechanisms should be adapted to include a diversity of such biological responses. The thermal dose parameter in hyperthermia treatments should predict the outcomes based on the applied treatment and enable comparisons of responses across different treatments conducted at various times and locations. Since we are using very different therapeutic agents, i.e., heat and cisPt, the thermal dose parameter here should not be based on the specific biological processes that elicit the response. Furthermore, the dose parameter should be a quantifiable and well-defined physical quantity, serving as a reliable basis for comparison. As will be shown at this end of this Chapter, there is such an approximation to a general definition of the thermal dose.

We started to study the idea of thermal dose on cell viability over time, following a pioneering study by Sapareto and Dewey [182],[26] who in 1984 proposed the concept of "equivalent minutes at 43 degrees Celsius", as a way to relate the exposure time and temperature in a biological context. This is still used as the definition of thermal dose through the cumulative equivalent minutes at 43°C (CEM43) given by the expression,

$$t_{CEM43} = t\, R^{(43-T)} \qquad 5.10$$

where t_{CEM43} is the cumulative equivalent minutes at 43 °C (the thermal dose), t is the exposure time (in minutes), and T is the actual temperature (in degrees Celsius). The parameter R is a constant for a given cell line, but a function of the absolute temperature, the activation energy and enthalpy ΔH

$$R = e^{-\Delta H/[2T(T+1)]} \qquad 5.11$$

The value of R is often taken as 0,5 for $T > 43°C$ and 0,25 for $T < 43°C$. The transition temperature, $43°C$, appears to be caused by the development of chronic tolerance, probably for the denaturation of a critical protein [182].

Equations 5.12 and 5.13 have been proposed in the '70s after different studies on the biological effectiveness of various types of ionizing radiation, based on absorbed dose and radiation time both *in vitro* and *in vivo*.[183] The term 'radiation' here refers to ionizing radiation from very different sources like electromagnetic waves (X-ray and γ-ray of $\approx 20 - 300\ keV$) to particles like electrons, protons and neutrons (of $\approx 4\ to\ \approx 200\ MeV$), and spanning a broad range of dose fractions, between 1 and 10 Gy. Those studies suggested that the primary damage to cells in different eukaryotes was directly related to the square of the specific energy, ζ, within the nucleus or sensitive areas within it, typically ranging from one to several micrometers in diameter. The equation

$$\varepsilon(\zeta) = k\zeta^2 \qquad 5.12$$

reflects this relationship, indicating that cellular damage arises from the interaction of pairs of sublesions caused by radiation, or more broadly, that primary cellular damage is a result of a second-order reaction to radiation products. This quadratic dependence on specific energy translates to a linear-quadratic relationship with absorbed dose D, expressed as

$$s(D) = k(\zeta D + D^2) \qquad 5.13$$

The linear part of this equation relates to damage within a single particle track, with ζ representing the average increase in specific energy caused by a single charged particle at the site. The quadratic part corresponds to damage from separate particles, signifying intra-track effects in the linear term and inter-track effects in the quadratic term. These relationships are clearly based on a physical radiation-matter interaction considering specific damage to chromosome centers, and it is no evident that this model could be translated into a landscape where cytotoxicity is produced by chemical drugs targeting different metabolic pathways. The same kind of difficulties arise when adapting these models to thermal dose in MFH.

Therefore, we aimed an empirical approach to the phenomenology of MFH and the combination MFH+CT, in terms of the already existent concept of cumulative equivalent minutes at 43 °C (t_{CEM43}) as the thermal dose of interest in potential clinical applications.

From the data obtained along hyperthermia experiments with different heat sources and nanovectors, it was possible to calculate the equivalent t_{CEM43} to deliver a specific thermal dose irrespective of the combination of LN, LNC or LC nanovectors. This was achieved by the generation of a 'universal' curve (Figure 5.19) representing the cell survival registered in each experiment. It can be seen that Figure 5.19 the results collapsed into a universal function of cell viability as a function of an isodose t_{CEM43}, that could be fitted by the linear quadratic expression [184]:

$$S = exp^{(-\alpha\, t_{CEM43} - \beta t_{CEM43}^{2})} \tag{5.14}$$

where S is the fraction of cell survival, α and β are two experimental parameters, whose ratio (α/β) has units of dose and is related to the rate of cell division. The agreement with experimental data is good irrespective of the nanovector or combination employed, suggesting that this model contains very general characteristics that do not depend on specificities in the cell death mechanism. For long t_{CEM43} values the experimental error increased, due to the experimental difficulties of measuring this vary lor survival percentages. The critical temperature was found to be 43,3°C as measured from the IC_{50} points (inset of Figure 5.19). This value is consistent with many previous reports on a variety of cell lines as well as *in vivo* studies. [185] [186] [187]

It is somewhat puzzling that our data follows the same currently accepted model for evaluating radiation response given a specific dose [188] which is in turn an improved version of the linear-quadratic model originally developed empirically more than 40 years ago.

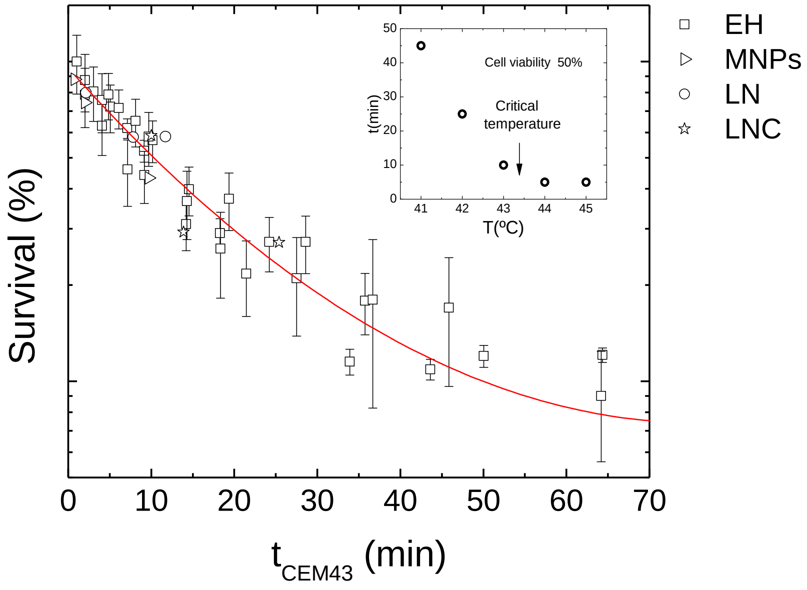

Figure 5.19. Logarithmic survival curve for PAN02 cell line with all the results from hyperthermia experiments as a function of the CEM at 43 °C. EH: Exothermal heating; MNPs: Magnetic Nanoparticles; LN: Synthetic Magnetosome; LNC: CisPt-loaded magnetosomes. All data could be collapse into a quadratic expression of the t_{CEM43}. Inset. Transition temperature obtained from t vs T data for IC_{50} viability points.

In the definition of equation 5.11, R is parameter with arbitrary units asymptotic to 1. This mathematical definition disagrees with the values found experimentally by various authors [182]. In our case, a polynomial dependence adjusts the values of R with the temperature. Comparing the different heating sources, EH, MNPs and LN, whose powers absorption tend to $P_{EH} < P_{MNPs} < P_{LN}$, a slight decrease in the linear parameter (B) and an increase with respect to the quadrat parameter with temperature (C), always being <1, it was observed. But, if we compare with the values obtained in the combined treatment, LNC, we obtain an abrupt change in parameters B and C.

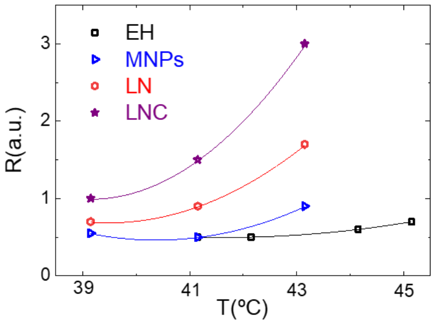

$$R = A + BT + CT^2$$

$Heating\ source$	$B(K^{-1})$	$C(K^{-2})$
EH	$-10{,}5$	$0{,}0167$
$MNPs$	$-34{,}9$	$0{,}0557$
LN	$-46{,}4$	$0{,}0742$
LNC	$-77{,}3$	$0{,}1237$

Figure 5.20. R dependence with temperature for different therapies (EH, MNPs, LN and the combined treatment of the nanocarrier LNC).

5.7. Conclusions

The core conclusion of this Chapter can be condensed in the fact that the new LNC system discussed in previous Chapters was indeed efficient to produce synergistic therapeutic effect, achieved through the simultaneous implementation of MFH and CT treatments on PAN02 cells. This synergy was notably evident after 10 minutes of MFH at temperatures of 39, 41, and 43 °C, combined with 1µM of cisPt. A significant breakthrough of this research, setting it apart from current clinical therapies, is the effective use of a single nanosystem to allow combined MHT-CT therapy.

One of the key results in this chapter is the founding of a universal curve, including results from various hyperthermia treatments. In a single isodose curve, PAN02 cell survival values were plotted against the equivalent thermal dose in minutes (t_{CEM43}) concerning the diverse treatments investigated. The meaning of this universal curve for the clinics is that, irrespective of the active cytotoxic origin (or a combination of many) an equivalent dose can be administered with the standard value of CEM at 43°C. Our proposed R factor introduces a quadratic temperature dependence, adeptly capturing the nuanced efficacy of each treatment. Findings from hyperthermia experiments underscored that $R_{EH}<R_{MNPs}<R_{LN}<R_{LNC}$, signifying that the LNC nanovector required less treatment time to induce equivalent damage compared to other heating sources. Although the R values found here aligned with those previously reported in the literature, some differences regarding its values above $R = 1$ (as compared to the $R < 1$ originally proposed) underscores the necessity for further exploration of this crucial parameter. The universal thermal dose curve emerges as a powerful analytical tool for medical physicists, gaining prominence in treatment planning where diverse approaches are suggested for the same dose, providing varied results applicable based on the patient's unique circumstances. This language and data processing signify a shift from treating MFH as a mere laboratory system to an integrated oncological treatment, effectively bridging the gap between the controlled laboratory environment and the complex dynamics of the hospital setting.

An additional conclusion from our experimental results is related to the fact that the lipid coating of LNC enhances the internalization of its constituent nanoparticles (when compared to the internalization of MNPs alone), and also improves internalization of cisPt (when contrasted with free cisPt and the encapsulated LC version), although LC and LNC formulation shows similar toxicity without the application of MFH. Both cell lines (BV2 and PAN02) showed active internalization of the nanosystems, forming vesicles in the cytoplasm that persisted after the MFH treatments. This turns out to be a relevant characteristic of the nanosystems since, by maintaining these intracellular curved MNPs chains structures, the possibility of subsequent MFH treatments can be contemplated without the need for additional LNC administration. This capability, demonstrated in this Thesis for the specific pancreatic cancer-related cell line PAN02, might also be applicable to various other cancer types.

CHAPTER 6

General Conclusions

"… En algo nos parecemos,
Luna de la soledad.
Yo voy andando y cantando,
que es mi modo de alumbrar…"
A. Yupanqui

A new type of synthetic magnetosome, designed to synergistically combine magnetic hyperthermia and chemotherapy, has been successfully developed. *This achievement was the result of a comprehensive, multidisciplinary approach. Each phase of the research was meticulously designed to meet stringent criteria and requisites for applying MHT and CT synergistic treatments in vitro.*

The LNC in vitro synergistic results in the simultaneous application of magnetic fluid hyperthermia and chemotherapy from a single dose. Comparative analyses revealed the superior efficiency of LNC over individual doses of cisPt or MFH alone, surpassing even the cumulative effects of both treatments. The lipid coating not only enhanced cellular uptake compared to traditional MNPs and free cisPt but also facilitated a reduction in the required dosage.

The heterogeneity of the nanocarrier, comprising liposomes loaded with cisPt and a magnetic component of curved lipid-coated particle chains, allows for on-demand and personalized treatments. This suggests the potential for synthesize the compounds separately and before combining them, showcasing an additional capability of LNC, where in one synthesis we encapsulate drug and MNPs.

The magnetic characteristics of the LN were found to be complex, deriving not only from their curved chain structure but also from the MNPs within them. The optimization of magnetically soft MNPs, particularly Zn-doped ferrites, exhibited unique responses, where power absorption were independent of the medium in which the particle was dispersed, this means, that Néel relaxation is the primary relaxation mechanism. In the LN, these particles form curved chains, increasing the SLP of MNPs up to 3 times. The unexpected increase in the *in vitro* SLP of MNPs, reaching values comparable to LN, was attributed to the formation of chains within cells after interaction with lipids in the cell membrane. The study of the dependence of SLP on the field and frequency highlighted the optimal working conditions for both LN and MNPs at high frequencies, providing crucial insights for the design of magnetic field application equipment.

A universal isodose curve was established, unifying cell survival results following hyperthermia, MFH, and MFH+CT treatments. This isobolographic curve serves as a fundamental tool for treatment planning, enabling a comprehensive comparison of therapies. Analyzing thermal dose data represents a unification with clinical language, minimizing the gap between the laboratory research and potential patient applications.

Future investigations may delve deeper into discerning the specific type of cell death induced by each treatment and exploring the potential of LNC or MNPs to trigger an immune response. This exploration could potentially open new avenues for new, innovative oncological therapies. *In conclusion, the LNC emerges as a highly promising system for combined oncological therapy, and its unique qualities warrant further exploration and dedicated study to unlock its full potential.*

Conclusiones Generales

Se ha desarrollado con éxito un nuevo tipo de magnetosoma sintético, diseñado para combinar sinérgicamente hipertermia magnética (MHT) y quimioterapia (CT). Este logro fue el resultado de un enfoque integral y multidisciplinario. Cada fase de la investigación fue diseñada meticulosamente para cumplir con criterios y requisitos estrictos para aplicar tratamientos sinérgicos de MHT y CT *in vitro*.

Los ensayos in vitro confirmaron la sinergia en la aplicación simultánea de HTM y CT, a partir de una única dosis de LNC. Los análisis comparativos revelaron la eficacia superior de LNC sobre las dosis individuales de cisplatino o HTM, superando incluso los efectos acumulativos de ambos tratamientos. El recubrimiento lipídico no sólo mejoró la internalización celular en comparación con las partículas y el cisplatino libre, posibilitando la reducción de la dosis administrada.

La heterogeneidad del nanotransportador, que comprende liposomas cargados con cisplatino y un componente magnético formado por cadenas de partículas curvadas recubiertas de lípidos, permite tratamientos a demanda y personalizados. Sugiriendo la posibilidad de sintetizar los compuestos por separado y combinarlos, mostrando una capacidad adicional del LNC, donde en una sola síntesis encapsulamos fármaco y nanopartículas magnéticas (MNPs).

Las características magnéticas de los LN son complejas, derivadas no sólo de su estructura de cadena curvada, sino también de las MNPs que lo componen. La optimización de las MNPs magnéticamente blandas, particularmente las ferritas dopadas con Zn, exhibieron respuestas únicas, donde la absorción de potencia fue independiente del medio en el que la partícula estaba dispersa, esto significa, que la relajación de Néel es el principal mecanismo de relajación. En los LN, estas partículas forman cadenas curvas, aumentando hasta 3 veces el SLP de las partículas. El inesperado aumento del SLP de las MNPs en los ensayos *in vitro*, alcanzando valores comparables al de los LN, se atribuyó a la formación de cadenas dentro de las células tras la interacción con los lípidos de la membrana celular. El estudio de la dependencia del SLP en función del campo y la frecuencia manifestó las condiciones óptimas de trabajo tanto para los LN como para las MNPs a altas frecuencias, proporcionando conocimientos cruciales para el diseño de equipos de aplicación de campos magnéticos.

En una curva de isodosis universal se unificaron los resultados de supervivencia celular tras los tratamientos de hipertermia, MHT y MHT+CT. Esta curva isobolográfica sirve como herramienta fundamental para la planificación del tratamiento, permitiendo la comparación de las terapias. El análisis de los datos de dosis térmica representa una unificación con el lenguaje clínico, minimizando la brecha entre el laboratorio y las potenciales aplicaciones en pacientes.

Futuras investigaciones podrían profundizar en discernir el tipo específico de muerte celular inducida por cada tratamiento y explorar el potencial de los LNC o las MNPs para desencadenar una respuesta inmunitaria. Esta exploración podría potencialmente abrir nuevas vías para terapias oncológicas innovadoras. *En conclusión, la LNC emerge como un sistema muy prometedor para la terapia oncológica combinada, y sus cualidades únicas justifican una mayor exploración y un estudio dedicado para explotar todo su potencial.*

References

1. *World Health Organization*. 2023; Available from: https://www.who.int/.
2. AIARC-WHO, A., UICC. *Cancer Atlas*. 2023; Available from: https://canceratlas.cancer.org/.
3. Sung, H., et al., *Global Cancer Statistics 2020: GLOBOCAN Estimates of Incidence and Mortality Worldwide for 36 Cancers in 185 Countries.* CA Cancer J Clin, 2021. **71**(3): p. 209-249.
4. Jain, K., *Advances in the field of nanooncology.* BMC Medicine, 2010. **8**(1): p. 83.
5. Chow, E.K.-H. and D. Ho, *Cancer Nanomedicine: From Drug Delivery to Imaging.* Science Translational Medicine, 2013. **5**(216).
6. Wicki, A., D. Witzigmann, V. Balasubramanian, and J. Huwyler, *Nanomedicine in cancer therapy: Challenges, opportunities, and clinical applications.* Journal of Controlled Release, 2015. **200**: p. 138-157.
7. Stathopoulos, G.P., et al., *Comparison of liposomal cisplatin versus cisplatin in non-squamous cell non-small-cell lung cancer.* Cancer Chemother Pharmacol, 2011. **68**(4): p. 945-50.
8. Anselmo, A.C. and S. Mitragotri, *Nanoparticles in the clinic.* Bioengineering & Translational Medicine, 2016. **1**(1): p. 10-29.
9. Anselmo, A.C. and S. Mitragotri, *Nanoparticles in the clinic: An update.* Bioengineering & Translational Medicine, 2019. **4**(3).
10. Hou, X., T. Zaks, R. Langer, and Y. Dong, *Lipid nanoparticles for mRNA delivery.* Nature Reviews Materials, 2021. **6**(12): p. 1078-1094.
11. Huang, Y., J.C. Hsu, H. Koo, and D.P. Cormode, *Repurposing ferumoxytol: Diagnostic and therapeutic applications of an FDA-approved nanoparticle.* Theranostics, 2022. **12**(2): p. 796-816.
12. Rubia-Rodríguez, I., et al., *Whither Magnetic Hyperthermia? A Tentative Roadmap.* Materials, 2021. **14**(4): p. 706.
13. Bangham, A.D., M.M. Standish, and J.C. Watkins, *Diffusion of univalent ions across the lamellae of swollen phospholipids.* Journal of Molecular Biology, 1965. **13**(1): p. 238-IN27.
14. Quinn, J.A., *Notes on the Development of a Critical Packing Parameter routine for Molecular Modeling Pro Plus®*, I. Norgwyn Montgomery Software, Editor. 2018.
15. Baccile, N., et al., *Self-assembly, interfacial properties, interactions with macromolecules and molecular modelling and simulation of microbial bio-based amphiphiles (biosurfactants). A tutorial review.* Green Chemistry, 2021. **23**(11): p. 3842-3944.
16. Anjan Motamarry, D.A.a.D.H., *Thermosensitive liposomes*, in *Liposome*. 2017, IntechOpen.
17. Yatvin, M.B., J.N. Weinstein, W.H. Dennis, and R. Blumenthal, *Design of liposomes for enhanced local release of drugs by hyperthermia.* Science, 1978. **202**(4374): p. 1290-1293.
18. Ta, T. and T.M. Porter, *Thermosensitive liposomes for localized delivery and triggered release of chemotherapy.* Journal of Controlled Release, 2013. **169**(1-2): p. 112-125.
19. Abarca-Cabrera, L., P. Fraga-García, and S. Berensmeier, *Bio-nano interactions: binding proteins, polysaccharides, lipids and nucleic acids onto magnetic nanoparticles.* Biomaterials Research, 2021. **25**(1).
20. Shinkai, M., et al., *Intracellular Hyperthermia for Cancer Using Magnetite Cationic Liposomes:<i>In vitro</i>Study.* Japanese Journal of Cancer Research, 1996. **87**(11): p. 1179-1183.

21. Yanase, M., et al., *Intracellular Hyperthermia for Cancer Using Magnetite Cationic Liposomes: An<i>in vivo</i>Study.* Japanese Journal of Cancer Research, 1998. **89**(4): p. 463-470.
22. Shinkai, M., et al., *Targeting Hyperthermia for Renal Cell Carcinoma Using Human MN Antigenspecific Magnetoliposomes.* Japanese Journal of Cancer Research, 2001. **92**(10): p. 1138-1146.
23. Hamaguchi, S., et al., *Selective hyperthermia using magnetoliposomes to target cervical lymph node metastasis in a rabbit tongue tumor model.* Cancer Science, 2003. **94**(9): p. 834-839.
24. Matsuoka, F., et al., BioMagnetic Research and Technology, 2004. **2**(1): p. 3.
25. García-Hevia, L., et al., *Magnetic lipid nanovehicles synergize the controlled thermal release of chemotherapeutics with magnetic ablation while enabling non-invasive monitoring by MRI for melanoma theranostics.* Bioactive Materials, 2022. **8**: p. 153-164.
26. Sapareto, S.A. and W.C. Dewey, *Thermal dose determination in cancer therapy.* International Journal of Radiation Oncology*Biology*Physics, 1984. **10**(6): p. 787-800.
27. Sapareto, S.A., *Thermal isoeffect dose: addressing the problem of thermotolerance.* Int J Hyperthermia, 1987. **3**(4): p. 297-305.
28. Gilchrist, R.K., et al., *Selective Inductive Heating of Lymph Nodes.* Annals of Surgery, 1957. **146**(4): p. 596-606.
29. Jordan, A., et al., *Presentation of a new magnetic field therapy system for the treatment of human solid tumors with magnetic fluid hyperthermia.* Journal of magnetism and magnetic materials, 2001. **225**(1-2): p. 118-126.
30. *NanoTherm*. Available from: https://project-nanotherm.com/.
31. *nB Nanoscale Biomagnetics*. Available from: https://www.nbnanoscale.com/.
32. *Nanotech solutions*. Available from: https://www.ntsol.es/.
33. Etemadi, H. and P.G. Plieger, *Magnetic Fluid Hyperthermia Based on Magnetic Nanoparticles: Physical Characteristics, Historical Perspective, Clinical Trials, Technological Challenges, and Recent Advances.* Advanced Therapeutics, 2020. **3**(11): p. 2000061.
34. Brezovich, I.A., *Low frequency hyperthermia: Capacitive and ferromagnetic thermoseed methods.* Med. Phys. Monogr, 1988. **16**: p. 82-111.
35. Cullity, B.D., *INTRODUCTION TO MAGNETIC MATERIALS.* 1972.
36. McCurrie, R.A., *Ferromagnetic materials: structure and properties.* (No Title), 1994.
37. Venkateshvaran, D., et al., *Epitaxial ${\text{Zn}}_{x}{\text{Fe}}_{3\ensuremath{-}x}{\text{O}}_{4}$ thin films: A spintronic material with tunable electrical and magnetic properties.* Physical Review B, 2009. **79**(13): p. 134405.
38. Tejera-Centeno, C., R. Rico, and S. Gallego, *Multiplicity of Zn coordination sites at cubic spinel ferrites: magnetism and influence of the Zn d band.* Journal of Materials Science, 2023. **58**(13): p. 5658-5677.
39. Kiwada, H., J. Sato, S. Yamada, and Y. Kato, *Feasibility of magnetic liposomes as a targeting device for drugs.* Chem Pharm Bull (Tokyo), 1986. **34**(10): p. 4253-8.
40. De Cuyper, M. and M. Joniau, *Magnetoliposomes.* European Biophysics Journal, 1988. **15**(5): p. 311-319.
41. Garnier, B., et al., *Optimized synthesis of 100 nm diameter magnetoliposomes with high content of maghemite particles and high MRI effect.* Contrast Media & Molecular Imaging, 2012. **7**(2): p. 231-239.
42. Bonnaud, C., et al., *Insertion of Nanoparticle Clusters into Vesicle Bilayers.* ACS Nano, 2014. **8**(4): p. 3451-3460.
43. Floris, A., et al., *SPION@liposomes hybrid nanoarchitectures with high density SPION association.* Soft Matter, 2011. **7**(13): p. 6239-6247.
44. Monnier, C.A., et al., *Magnetoliposomes: opportunities and challenges.* European Journal of Nanomedicine, 2014. **6**(4).

45. Fortin-Ripoche, J.P., et al., *Magnetic targeting of magnetoliposomes to solid tumors with MR imaging monitoring in mice: feasibility.* Radiology, 2006. **239**(2): p. 415-24.
46. Bleehen, N.M., *Hyperthermia in the treatment of cancer.* Br J Cancer Suppl, 1982. **5**: p. 96-100.
47. Yang, S.J., et al., *The Synergistic Effect of Hyperthermia and Chemotherapy in Magnetite Nanomedicine-Based Lung Cancer Treatment.* Int J Nanomedicine, 2020. **15**: p. 10331-10347.
48. Phung, D.C., et al., *Combined hyperthermia and chemotherapy as a synergistic anticancer treatment.* Journal of Pharmaceutical Investigation, 2019. **49**(5): p. 519-526.
49. Wang, K., J. Lu, and R. Li, *The events that occur when cisplatin encounters cells.* Coordination Chemistry Reviews, 1996. **151**: p. 53-88.
50. El-Khateeb, M., et al., *Reactions of cisplatin hydrolytes with methionine, cysteine, and plasma ultrafiltrate studied by a combination of HPLC and NMR techniques.* Journal of Inorganic Biochemistry, 1999. **77**(1-2): p. 13-21.
51. Kuo, M.T., et al., *The roles of copper transporters in cisplatin resistance.* Cancer and Metastasis Reviews, 2007. **26**(1): p. 71-83.
52. Aldossary, S.A., *Review on Pharmacology of Cisplatin: Clinical Use, Toxicity and Mechanism of Resistance of Cisplatin.* Biomedical and Pharmacology Journal, 2019. **12**(1): p. 07-15.
53. Boulikas, T. and M. Vougiouka, *Cisplatin and platinum drugs at the molecular level. (Review).* Oncol Rep, 2003. **10**(6): p. 1663-82.
54. Sun, S., et al., *Monodisperse MFe2O4 (M = Fe, Co, Mn) Nanoparticles.* Journal of the American Chemical Society, 2003. **126**(1): p. 273-279.
55. Kwon, S.G. and T. Hyeon, *Formation Mechanisms of Uniform Nanocrystals via Hot-Injection and Heat-Up Methods.* Small, 2011. **7**(19): p. 2685-2702.
56. Molina, T.E.T., *Power absorption mechanisms in high anisotropy cofe2o4 magnetic nanoparticles*, in *Meteria condensada*. 2015, Zaragoza. p. 245.
57. Hatakeyama, M., et al., *A two-step ligand exchange reaction generates highly water-dispersed magnetic nanoparticles for biomedical applications.* Journal of Materials Chemistry, 2011. **21**(16).
58. Adams, P.E., *Determining Iron Content in Foods by Spectrophotometry.* Journal of Chemical Education, 1995. **72**(7).
59. Stewart, J.C.M., *Colorimetric determination of phospholipids with ammonium ferrothiocyanate.* Analytical Biochemistry, 1980. **104**(1): p. 10-14.
60. Basotra, M., S.K. Singh, and M. Gulati, *Development and Validation of a Simple and Sensitive Spectrometric Method for Estimation of Cisplatin Hydrochloride in Tablet Dosage Forms: Application to Dissolution Studies.* ISRN Analytical Chemistry, 2013. **2013**: p. 1-8.
61. Yoshida, M., et al., *Feasibility of chemohyperthermia with docetaxel-embedded magnetoliposomes as minimally invasive local treatment for cancer.* Int J Cancer, 2010. **126**(8): p. 1955-1965.
62. Toro-Cordova, A., et al., *Liposomes Loaded with Cisplatin and Magnetic Nanoparticles: Physicochemical Characterization, Pharmacokinetics, and In-Vitro Efficacy.* Molecules, 2018. **23**(9): p. 2272.
63. Garcia-Pinel, B., et al., *Biomimetic Magnetoliposomes as Oxaliplatin Nanocarriers: In Vitro Study for Potential Application in Colon Cancer.* Pharmaceutics, 2020. **12**(6): p. 589.
64. Wang, L., C.-q. Yang, and J. Wang, *Effects of loading procedures of magnetic nanoparticles on the structure and physicochemical properties of cisplatin magnetic liposomes.* Journal of Microencapsulation, 2012. **29**(8): p. 781-789.
65. Pradhan, P., et al., *Targeted temperature sensitive magnetic liposomes for thermo-chemotherapy.* Journal of Controlled Release, 2010. **142**(1): p. 108-121.

66. Fdez-Gubieda, M.L., et al., *Magnetite Biomineralization in Magnetospirillum gryphiswaldense: Time-Resolved Magnetic and Structural Studies.* ACS Nano, 2013. **7**(4): p. 3297-3305.
67. Faivre, D. and D. Schüler, *Magnetotactic Bacteria and Magnetosomes.* Chemical Reviews, 2008. **108**(11): p. 4875-4898.
68. Torres, T.E., *Power absorption mechanisms in high-anisotropy CoFe2O4 magnetic nanoparticles*, in *Departamento de Fisica de la Maeria Condensada*. 2015, Universidad de Zaragoza.
69. Obaidat, I., B. Issa, and Y. Haik, *Magnetic Properties of Magnetic Nanoparticles for Efficient Hyperthermia.* Nanomaterials, 2015. **5**(1): p. 63-89.
70. Guardia, P., N. Pérez, A. Labarta, and X. Batlle, *Controlled Synthesis of Iron Oxide Nanoparticles over a Wide Size Range.* Langmuir, 2009. **26**(8): p. 5843-5847.
71. Roca, A.G., *PREPARACION DE NANOPARTÍCULAS MAGNÉTICAS DE ALTA CRISTALINIDAD PARA BIOMEDICINA*, in *Insitituto de Ciencias de Materiales de Madrid,CSIC* 2009, Departamento de Materiales Particulados & Universidad Complutenese de Madrid,Quimica Fisica I.
72. Venkateshvaran, D., et al., *Epitaxial Zn x Fe 3− x O 4 thin films: a spintronic material with tunable electrical and magnetic properties.* Physical Review B, 2009. **79**(13): p. 134405.
73. Zhou, W. and Z.L. Wang, *Scanning microscopy for nanotechnology : techniques and applications*. 2007, New York: Springer. xiv, 522 p., 12 p. of plates.
74. Bielicka, M., et al., *Role of the synthesis procedure on the physicochemical properties of doped magnetite.* Advanced Powder Technology, 2023. **34**(2).
75. Fujii, T., et al., *<i>In situ</i>XPS analysis of various iron oxide films grown by<mml:math xmlns:mml="http://www.w3.org/1998/Math/MathML" display="inline"><mml:mrow><mml:msub><mml:mrow><mml:mi mathvariant="normal">NO</mml:mi></mml:mrow><mml:mrow><mml:mn>2</mml:mn></mml:mro.* Physical Review B, 1999. **59**(4): p. 3195-3202.
76. Fabris, F., et al., *Annealing effects on the magnetic and magnetotransport properties of iron oxide nanoparticles self-assemblies.* Nanotechnology, 2023. **34**(45).
77. Grosvenor, A.P., B.A. Kobe, M.C. Biesinger, and N.S. McIntyre, *Investigation of multiplet splitting of Fe 2p XPS spectra and bonding in iron compounds.* Surface and Interface Analysis, 2004. **36**(12): p. 1564-1574.
78. Biesinger, M.C., et al., *Resolving surface chemical states in XPS analysis of first row transition metals, oxides and hydroxides: Cr, Mn, Fe, Co and Ni.* Applied Surface Science, 2011. **257**(7): p. 2717-2730.
79. Biesinger, M.C., L.W.M. Lau, A.R. Gerson, and R.S.C. Smart, *Resolving surface chemical states in XPS analysis of first row transition metals, oxides and hydroxides: Sc, Ti, V, Cu and Zn.* Applied Surface Science, 2010. **257**(3): p. 887-898.
80. Hong, R.Y., et al., *On the Fe3O4/Mn1−xZnxFe2O4 core/shell magnetic nanoparticles.* Journal of Alloys and Compounds, 2009. **480**(2): p. 947-953.
81. Morozov, I.G., et al., *Structural, optical, XPS and magnetic properties of Zn particles capped by ZnO nanoparticles.* Journal of Alloys and Compounds, 2015. **633**: p. 237-245.
82. Fabris, F., et al., *Adjusting the Néel relaxation time of Fe₃O₄/Zn<i> _x </i>Co_{1−<i>x</i>}Fe₂O₄ core/shell nanoparticles for optimal heat generation in magnetic hyperthermia.* Nanotechnology, 2021. **32**(6): p. 065703.
83. Zélis, P.M., et al., *Structural and magnetic study of zinc-doped magnetite nanoparticles and ferrofluids for hyperthermia applications.* Journal of Physics D: Applied Physics, 2013. **46**(12): p. 125006.
84. Castellanos-Rubio, I., et al., *Shaping Up Zn-Doped Magnetite Nanoparticles from Mono- and Bimetallic Oleates: The Impact of Zn Content, Fe Vacancies, and Morphology on*

Magnetic Hyperthermia Performance. Chemistry of Materials, 2021. **33**(9): p. 3139-3154.

85. Guardia, P., et al., *Surfactant effects in magnetite nanoparticles of controlled size.* Journal of Magnetism and Magnetic Materials, 2007. **316**(2): p. e756-e759.
86. Cullity, B.D., *INTRODUCTION TO MAGNETIC MATERIALS*. 1997.
87. Li, S., et al., *Solvothermal synthesis and characterization of monodisperse superparamagnetic iron oxide nanoparticles.* Journal of Magnetism and Magnetic Materials, 2015. **379**: p. 226-231.
88. Abu-Noqta, O.A., A.A. Aziz, and A.I. Usman, *Colloidal Stability of Iron Oxide Nanoparticles Coated with Different Capping Agents.* Materials Today: Proceedings, 2019. **17**: p. 1072-1077.
89. Gonzalez-Martinez, D.A., et al., *Efficient capture of recombinant SARS-CoV-2 receptor-binding domain (RBD) with citrate-coated magnetic iron oxide nanoparticles.* Nanoscale, 2023. **15**(17): p. 7854-7869.
90. Guo, C.X., S. Huang, and X. Lu, *A solventless thermolysis route to large-scale production of ultra-small hydrophilic and biocompatible magnetic ferrite nanocrystals and their application for efficient protein enrichment.* Green Chemistry, 2014. **16**(5): p. 2571.
91. Ozel, F., et al., *Superparamagnetic iron oxide nanoparticles: effect of iron oleate precursors obtained with a simple way.* Journal of Materials Science: Materials in Electronics, 2013. **24**(8): p. 3073-3080.
92. Kwon, S.G., et al., *Kinetics of monodisperse iron oxide nanocrystal formation by "heating-up" process.* J Am Chem Soc, 2007. **129**(41): p. 12571-84.
93. Zhao, H., R. Liu, Q. Zhang, and Q. Wang, *Effect of surfactant amount on the morphology and magnetic properties of monodisperse ZnFe 2 O 4 nanoparticles.* Materials Research Bulletin, 2016. **75**: p. 172-177.
94. Guo, C.X., S. Huang, and X. Lu, *A solventless thermolysis route to large-scale production of ultra-small hydrophilic and biocompatible magnetic ferrite nanocrystals and their application for efficient protein enrichment.* Green Chemistry, 2014. **16**(5).
95. Maherani, B., et al., *Liposomes: A Review of Manufacturing Techniques and Targeting Strategies.* Current Nanoscience, 2011. **7**(3): p. 436-452.
96. Tharad, S., Ö. Üzülmez, B. Promdonkoy, and J. Toca-Herrera, *Cholesterol Increases Lipid Binding Rate and Changes Binding Behavior of Bacillus thuringiensis Cytolytic Protein.* International Journal of Molecular Sciences, 2018. **19**(12).
97. Tucci, S.T., et al., *Tumor-specific delivery of gemcitabine with activatable liposomes.* Journal of Controlled Release, 2019. **309**: p. 277-288.
98. Torres, M., et al., *Raman and Infrared Studies of Platinum-Based Drugs: Cisplatin, Carboplatin, Oxaliplatin, Nedaplatin, and Heptaplatin.* The Journal of Physical Chemistry A, 2018. **122**(34): p. 6934-6952.
99. Lai, Y.-L., C.-C. Lin, S.-R. Hsu, and S.-K. Yen, *Electrochemical Deposition of Cisplatin on Pure Magnesium.* Journal of The Electrochemical Society, 2018. **165**(5): p. D196-D205.
100. Koynova, R. and M. Caffrey, *Phases and phase transitions of the phosphatidylcholines.* Biochimica et Biophysica Acta (BBA) - Reviews on Biomembranes, 1998. **1376**(1): p. 91-145.
101. Demetzos, C., *Differential Scanning Calorimetry (DSC): A Tool to Study the Thermal Behavior of Lipid Bilayers and Liposomal Stability.* Journal of Liposome Research, 2008. **18**(3): p. 159-173.
102. Matsingou, C. and C. Demetzos, *The perturbing effect of cholesterol on the interaction between labdanes and DPPC bilayers.* Thermochimica Acta, 2007. **452**(2): p. 116-123.
103. Speelmans, G., et al., *The interaction of the anti-cancer drug cisplatin with phospholipids is specific for negatively charged phospholipids and takes place at low chloride ion concentration.* Biochimica et Biophysica Acta (BBA) - Biomembranes, 1996. **1283**(1): p. 60-66.

104. Maswadeh, H., et al., *A molecular basis explanation of the dynamic and thermal effects of vinblastine sulfate upon dipalmitoylphosphatidylcholine bilayer membranes.* Biochim Biophys Acta, 2002. **1567**(1-2): p. 49-55.
105. Mady, M.M., M.W. Shafaa, E.R. Abbase, and A.H. Fahium, *Interaction of Doxorubicin and Dipalmitoylphosphatidylcholine Liposomes.* Cell Biochemistry and Biophysics, 2011. **62**(3): p. 481-486.
106. Renault-Mahieux, M., et al., *Co-Encapsulation of Fisetin and Cisplatin into Liposomes for Glioma Therapy: From Formulation to Cell Evaluation.* Pharmaceutics, 2021. **13**(7): p. 970.
107. Velez-Saboyá, C.S., J.R. Guzmán-Sepúlveda, and J.C. Ruiz-Suárez, *Phase transitions of liposomes: when light meets heat.* Journal of Physics: Condensed Matter, 2022. **34**(12).
108. Perinelli, D.R., et al., *Heating treatments affect the thermal behaviour of doxorubicin loaded in PEGylated liposomes.* International Journal of Pharmaceutics, 2017. **534**(1-2): p. 81-88.
109. Michel, N., et al., *Determination of phase transition temperatures of lipids by light scattering.* Chemistry and Physics of Lipids, 2006. **139**(1): p. 11-19.
110. Kirschvink, J.L., *Paleomagnetic evidence for fossil biogenic magnetite in western Crete.* Earth and Planetary Science Letters, 1982. **59**(2): p. 388-392.
111. Muela, A., et al., *Optimal Parameters for Hyperthermia Treatment Using Biomineralized Magnetite Nanoparticles: Theoretical and Experimental Approach.* The Journal of Physical Chemistry C, 2016. **120**(42): p. 24437-24448.
112. Shokri, B., M. Abbasi-Firouzjah, and S.I. Hosseini, *FTIR analysis of silicon dioxide thin film deposited by Metal organic-based PECVD.* Proceedings of 19th International Symposium on Plasma Chemistry Society, 2009.
113. Cullity, B.D., *INTRODUCTION TO MAGNETIC MATERIALS.* 1972: Addison-Wisley Publishing Company, Inc., Menlo Park. . 666.
114. Goya, G., V. Grazu, and M.R. Ibarra, *Magnetic nanoparticles for cancer therapy.* Current nanoscience, 2008. **4**(1): p. 1-16.
115. Kittel, C., *Theory of the Structure of Ferromagnetic Domains in Films and Small Particles.* Physical Review, 1946. **70**(11-12): p. 965-971.
116. Brown, W.F., Jr., *The Fundamental Theorem of Fine-Ferromagnetic-Particle Theory.* Journal of Applied Physics, 2003. **39**(2): p. 993-994.
117. Butler, R.F. and S.K. Banerjee, *Theoretical single-domain grain size range in magnetite and titanomagnetite.* Journal of Geophysical Research (1896-1977), 1975. **80**(29): p. 4049-4058.
118. Moon, T.S., *Domain states in fine particle magnetite and titanomagnetite.* Journal of Geophysical Research: Solid Earth, 1991. **96**(B6): p. 9909-9923.
119. Mojica Pisciotti, M.L., *Desarrollo de nanopartículas magnéticas para su utilización en el tratamiento médico: hipertermia*, in *Fisica*. 2015, Instituto Balseiro - Universidad Nacional de Cuyo.
120. Zysler, R.D., *Propiedades magnéticas a escala nanométrica II*. Laboratorio de resonancias magnéticas. Centro Atómico Bariloche. Instituto Balseiro - Universidad Nacional de Cuyo. p. 27-41.
121. Torres, T.E., *Ph D Thesis. Power absorption mechanisms in high-anisotropy CoFe2O4 magnetic nanoparticles*, in *Departamento de Fisica de la Maeria Condensada*. 2015, Universidad de Zaragoza.
122. Andreu, I. and E. Natividad, *Accuracy of available methods for quantifying the heat power generation of nanoparticles for magnetic hyperthermia.* International Journal of Hyperthermia, 2013. **29**(8): p. 739-751.
123. Lemal, P., et al., *Measuring the heating power of magnetic nanoparticles: an overview of currently used methods.* Materials Today: Proceedings, 2017. **4**: p. S107-S117.

124. Valdés, D.P., et al., *Role of Anisotropy, Frequency, and Interactions in Magnetic Hyperthermia Applications: Noninteracting Nanoparticles and Linear Chain Arrangements.* Physical Review Applied, 2021. **15**(4).
125. Ruta, S., et al., *A device-independent approach to evaluate the heating performance during magnetic hyperthermia experiments: peak analysis and zigzag protocol.* arXiv pre-print server, 2023.
126. Torres, T.E., et al., *The relevance of Brownian relaxation as power absorption mechanism in Magnetic Hyperthermia.* Scientific reports, 2019. **9**(1): p. 3992.
127. Rosensweig, R.E., *Heating magnetic fluid with alternating magnetic field.* Journal of Magnetism and Magnetic Materials, 2002. **252**: p. 370-374.
128. Lima, E., et al., *Relaxation time diagram for identifying heat generation mechanisms in magnetic fluid hyperthermia.* Journal of Nanoparticle Research, 2014. **16**(12).
129. Carrey, J., B. Mehdaoui, and M. Respaud, *Simple models for dynamic hysteresis loop calculations of magnetic single-domain nanoparticles: Application to magnetic hyperthermia optimization.* Journal of Applied Physics, 2011. **109**(8).
130. Chen, S., C.-l. Chiang, and S. Hsieh, *Simulating physiological conditions to evaluate nanoparticles for magnetic fluid hyperthermia (MFH) therapy applications.* Journal of Magnetism and Magnetic Materials, 2010. **322**(2): p. 247-252.
131. Wells, J., et al., *Challenges and recommendations for magnetic hyperthermia characterization measurements.* International Journal of Hyperthermia, 2021. **38**(1): p. 447-460.
132. *Nanotechnologies—Magnetic Nanomaterials—Part 1: Specification of Characteristics And Measurements for Magnetic Nanosuspensions*. 2019: International Organisation for Standardisation: Geneva, Switzerland.
133. Ortega, D. and Q.A. Pankhurst, *Magnetic hyperthermia*, in *Nanoscience*. 2012. p. 60-88.
134. Mamiya, H., et al., *Estimation of Magnetic Anisotropy of Individual Magnetite Nanoparticles for Magnetic Hyperthermia.* ACS Nano, 2020. **14**(7): p. 8421-8432.
135. Aghazadeh, M., *Zn-doped magnetite nanoparticles: development of novel preparation method and evaluation of magnetic and electrochemical capacitance performances.* Journal of Materials Science: Materials in Electronics, 2017. **28**(24): p. 18755-18764.
136. Cullity, B.D., *INTRODUCTION TO MAGNETIC MATERIALS*. 1972.
137. Krupička, S. and P. Novák, *Chapter 4 Oxide spinels*, in *Handbook of Ferromagnetic Materials*. 1982, Elsevier. p. 189-304.
138. Guardia, P., A. Labarta, and X. Batlle, *Tuning the size, the shape, and the magnetic properties of iron oxide nanoparticles.* The Journal of Physical Chemistry C, 2011. **115**(2): p. 390-396.
139. Dunin-Borkowski, R.E., et al., *Off-axis electron holography of magnetic nanowires and chains, rings, and planar arrays of magnetic nanoparticles.* Microscopy research and technique, 2004. **64**(5-6): p. 390-402.
140. Molcan, M., et al., *Magnetic hyperthermia study of magnetosome chain systems in tissue-mimicking phantom.* Journal of Molecular Liquids, 2020. **320**.
141. Serantes, D., et al., *Multiplying Magnetic Hyperthermia Response by Nanoparticle Assembling.* The Journal of Physical Chemistry C, 2014. **118**(11): p. 5927-5934.
142. Walker, M., et al., *The magnetic properties of single-domain particles with cubic anisotropy. I. Hysteresis loops.* Journal of Physics: Condensed Matter, 1993. **5**(17): p. 2779.
143. Paulus, P., et al., *Low-temperature study of the magnetization reversal and magnetic anisotropy of Fe, Ni, and Co nanowires.* Journal of Magnetism and Magnetic Materials, 2001. **224**(2): p. 180-196.
144. Usov, N. and Y.B. Grebenshchikov, *Hysteresis loops of an assembly of superparamagnetic nanoparticles with uniaxial anisotropy.* Journal of Applied Physics, 2009. **106**(2).

145. Nunes, W.C., W.S.D. Folly, J.P. Sinnecker, and M.A. Novak, *Temperature dependence of the coercive field in single-domain particle systems.* Physical Review B, 2004. **70**(1).
146. Liu, X.L., et al., *Optimization of surface coating on Fe3O4 nanoparticles for high performance magnetic hyperthermia agents.* Journal of Materials Chemistry, 2012. **22**(17).
147. Kim, D.H., K.N. Kim, K.M. Kim, and Y.K. Lee, *Targeting to carcinoma cells with chitosan- and starch-coated magnetic nanoparticles for magnetic hyperthermia.* Journal of Biomedical Materials Research Part A, 2008. **88A**(1): p. 1-11.
148. Atkinson, W.J., I.A. Brezovich, and D.P. Chakraborty, *Usable frequencies in hyperthermia with thermal seeds.* IEEE Transactions on Biomedical Engineering, 1984(1): p. 70-75.
149. Brezovich, I.A., W.J. Atkinson, and M.B. Lilly, *Local hyperthermia with interstitial techniques.* Cancer research, 1984. **44**(10_Supplement): p. 4752s-4756s.
150. Herrero de la Parte, B., et al., *Proposal of new safety limits for in vivo experiments of magnetic hyperthermia antitumor therapy.* Cancers, 2022. **14**(13): p. 3084.
151. Mérida, F., et al., *Optimization of synthesis and peptization steps to obtain iron oxide nanoparticles with high energy dissipation rates.* Journal of Magnetism and Magnetic Materials, 2015. **394**: p. 361-371.
152. Nishimoto, K., et al., *High intrinsic loss power of multicore magnetic nanoparticles with blood-pooling property for hyperthermia.* AIP Advances, 2019. **9**(3).
153. Bender, P., et al., *Relating Magnetic Properties and High Hyperthermia Performance of Iron Oxide Nanoflowers.* The Journal of Physical Chemistry C, 2018. **122**(5): p. 3068-3077.
154. Avugadda, S.K., et al., *Esterase-Cleavable 2D Assemblies of Magnetic Iron Oxide Nanocubes: Exploiting Enzymatic Polymer Disassembling To Improve Magnetic Hyperthermia Heat Losses.* Chemistry of Materials, 2019. **31**(15): p. 5450-5463.
155. Albarqi, H.A., et al., *Biocompatible Nanoclusters with High Heating Efficiency for Systemically Delivered Magnetic Hyperthermia.* ACS Nano, 2019. **13**(6): p. 6383-6395.
156. Branquinho, L.C., et al., *Effect of magnetic dipolar interactions on nanoparticle heating efficiency: Implications for cancer hyperthermia.* Scientific Reports, 2013. **3**(1).
157. Schwab, E. and K.J. Pienta, *Cancer as a complex adaptive system.* Medical hypotheses, 1996. **47**(3): p. 235-241.
158. Derbal, Y., *The adaptive complexity of cancer.* BioMed Research International, 2018. **2018**.
159. Salgia, R. and P. Kulkarni, *The genetic/non-genetic duality of drug 'resistance'in cancer.* Trends in cancer, 2018. **4**(2): p. 110-118.
160. Dewey, W.C., L.E. Hopwood, S.A. Sapareto, and L.E. Gerweck, *Cellular Responses to Combinations of Hyperthermia and Radiation.* Radiology, 1977. **123**(2): p. 463-474.
161. Kolašinac, R., et al., *Delivery of the Radionuclide 131I Using Cationic Fusogenic Liposomes as Nanocarriers.* International Journal of Molecular Sciences, 2021. **22**(1): p. 457.
162. Rawla, P., T. Sunkara, and V. Gaduputi, *Epidemiology of pancreatic cancer: global trends, etiology and risk factors.* World journal of oncology, 2019. **10**(1): p. 10.
163. Swayden, M., J. Iovanna, and P. Soubeyran, *Pancreatic cancer chemo-resistance is driven by tumor phenotype rather than tumor genotype.* Heliyon, 2018. **4**(12).
164. Roell, K.R., D.M. Reif, and A.A. Motsinger-Reif, *An Introduction to Terminology and Methodology of Chemical Synergy—Perspectives from Across Disciplines.* Frontiers in Pharmacology, 2017. **8**.
165. Bliss, C.I., *The Toxicity of Poisons Applied Jointly1.* Annals of Applied Biology, 1939. **26**(3): p. 585-615.
166. Loewe, S., *Die quantitativen probleme der pharmakologie.* Ergebnisse der Physiologie, 1928. **27**(1): p. 47-187.
167. Loewe, S., *Effect of combinations: mathematical basis of problem.* Arch. Exp. Pathol. Pharmakol., 1926. **114**: p. 313-326.

168. Demidenko, E. and T.W. Miller, *Statistical determination of synergy based on Bliss definition of drugs independence.* PLoS One, 2019. **14**(11): p. e0224137.
169. Fraser, T.R., *5. An experimental research on the antagonism between the actions of physostigma and atropia.* Proceedings of the Royal Society of Edinburgh, 1872. **7**: p. 506-511.
170. Blasi, E., et al., *Immortalization of murine microglial cells by a v-raf / v-myc carrying retrovirus.* Journal of Neuroimmunology, 1990. **27**(2): p. 229-237.
171. Calatayud, M.P., et al., *Cell damage produced by magnetic fluid hyperthermia on microglial BV2 cells.* Scientific Reports, 2017. **7**(1).
172. León Félix, L., et al., *Gold-decorated magnetic nanoparticles design for hyperthermia applications and as a potential platform for their surface-functionalization.* Scientific Reports, 2019. **9**(1).
173. Moreno Maldonado, A.C., et al., *Free-Radical Formation by the Peroxidase-Like Catalytic Activity of MFe2O4 (M = Fe, Ni, and Mn) Nanoparticles.* The Journal of Physical Chemistry C, 2019. **123**(33): p. 20617-20627.
174. Corbett, T.H., et al., *Induction and Chemotherapeutic Response of Two Transplantable Ductal Adenocarcinomas of the Pancreas in C57BL/6 Mice1.* Cancer Research, 1984. **44**(2): p. 717-726.
175. Mowshowitz, L.C.a.D., *Introduction to Molecular and cellular biology*, D.o.B.S.C. University, Editor. 2001, Columbia Center for New Media Teaching and Learning: New York, NY.
176. Torres, M.P., et al., *Novel Pancreatic Cancer Cell Lines Derived from Genetically Engineered Mouse Models of Spontaneous Pancreatic Adenocarcinoma: Applications in Diagnosis and Therapy.* PLoS ONE, 2013. **8**(11): p. e80580.
177. Online, D.B., *Cisplatin*. 2023: Drug Bank Online.
178. Sanz, B., et al., *Magnetic hyperthermia enhances cell toxicity with respect to exogenous heating.* Biomaterials, 2017. **114**: p. 62-70.
179. Miyashita, H., et al., *Expression of copper-transporting P-type adenosine triphosphatase (ATP7B) as a chemoresistance marker in human oral squamous cell carcinoma treated with cisplatin.* Oral Oncology, 2003. **39**(2): p. 157-162.
180. Boulikas, T., *Molecular mechanisms of cisplatin and its liposomally encapsulated form, Lipoplatin™. Lipoplatin™ as a chemotherapy and antiangiogenesis drug.* Cancer Therapy. **5**: p. 351-376.
181. Gao, L., et al., *Intrinsic peroxidase-like activity of ferromagnetic nanoparticles.* Nature Nanotechnology, 2007. **2**(9): p. 577-583.
182. Dewey, W.C., *Arrhenius relationships from the molecule and cell to the clinic.* International Journal of Hyperthermia, 2009. **25**(1): p. 3-20.
183. Thames Jr, H.D., H.R. Withers, L.J. Peters, and G.H. Fletcher, *Changes in early and late radiation responses with altered dose fractionation: implications for dose-survival relationships.* International Journal of Radiation Oncology* Biology* Physics, 1982. **8**(2): p. 219-226.
184. Mouratidis, P.X., et al., *Relationship between thermal dose and cell death for "rapid" ablative and "slow" hyperthermic heating.* International Journal of Hyperthermia, 2019.
185. Piazena, H., P. Vaupel, and A.R. Thomsen, *Clinical wIRA-hyperthermia: heating properties and effectiveness in lower trunk regions and its accordance with ESHO quality criteria for superficial hyperthermia.* International Journal of Hyperthermia, 2023. **40**(1): p. 2244208.
186. van Rhoon, G.C., *Is CEM43 still a relevant thermal dose parameter for hyperthermia treatment monitoring?* International Journal of Hyperthermia, 2016. **32**(1): p. 50-62.
187. Thrall, D., et al., *Using units of CEM 43 C T90, local hyperthermia thermal dose can be delivered as prescribed.* International journal of hyperthermia, 2000. **16**(5): p. 415-428.

188. Liu, J., D.A. Hormuth, J. Yang, and T.E. Yankeelov, *A Multi-Compartment Model of Glioma Response to Fractionated Radiation Therapy Parameterized via Time-Resolved Microscopy Data.* Frontiers in oncology, 2022. **12**: p. 811415.

List of publications

1) “Free-Radical Formation by the Peroxidase-Like Catalytic Activity of MFe2O4 (M = Fe, Ni, and Mn) Nanoparticles.” Ana Carolina Moreno Maldonado, Elin L. Winkler, Mariana Raineri,Alfonso Toro Córdova, Luis M. Rodríguez, Horacio E. Troiani, Mary Luz Mojica Pisciotti, Marcelo Vasquez Mansilla, Dina Tobia,Marcela S. Nadal, Teobaldo E. Torres, Emilio De Biasi, Carlos A. Ramos, Gerardo F. Goya, Roberto D. Zysler, and Enio Lima, Jr. J. Phys. Chem. C 2019, 123, 20617−20627.

2) Reply to “Comment on “Free-Radical Formation by the Peroxidase like Catalytic Activity of MFe2O4 (M = Fe, Ni and Mn) Nanoparticules.”” Ana Carolina Moreno Maldonado, Elin L Winkler, Mariana Raineri, Alfonso Toro Cordova, Luis M. Rodriguez, Horacio E. Troiani, Mary Luz Mojica Pisciotti, Marcelo Vasquez Mansilla, Dina Tobia, Marcela S Nadal,Teobaldo Torres, Emilio De Biasi, Carlos A. Ramos, Gerardo F. Goya, Roberto D Zysler, and Enio Lima. J. Phys. Chem. C. 2019

3) “Simple Sonochemical Method to Optimize the Heating Efficiency of Magnetic Nanoparticles for Magnetic Fluid Hyperthermia” Jesús Antonio Fuentes-García, Alex Carvalho Alavarse, Ana Carolina Moreno Maldonado, Alfonso Toro-Córdova, Manuel Ricardo Ibarra, and Gerardo Fabián Goya. ACS Omega 2020, 5, 26357−26364.

4) “Thermographical Method to Assess the Performance of Magnetic Nanoparticles in Hyperthermia Experiments through Spatiotemporal Temperature Profiles” D.P. Valdés, T.E. Torres, A.C. Moreno Maldonado, G. Urretavizcaya, M.S. Nadal , M. Vasquez Mansilla, R.D. Zysler, G.F. Goya, E. De Biasi, and E. Lima Jr. PHYSICAL REVIEW APPLIED 19, 014042 (2023).

5) “The effect of ultrafine WO3 nanoparticles on the organization of thylakoids enriched in photosystem II and energy transfer in photosystem II complexes” S. Krysiak, M. Gotic, E. Madej, A. C. Moreno Maldonado, G. F. Goya, N. Spiridis, K. Burda. Microsc Res Tech. 2023;1–16.

6) Comment on “Local Temperature Increments and Induced Cell Death in Intracellular Magnetic Hyperthermia” Ana Carolina Moreno Maldonado and Gerardo F. Goya. ACS Nano 2023, 17, 15217−15218.

7) “Cyto-Genotoxic and Physicochemical Assessment of $Fe_{3-x}V_xO_4$ Nanoparticles for Human Health Applications.” Beatriz Sanz-Sagué, Amaia Sáenz Hernández, A.C. Moreno Maldonado, Jesús A. Fuentes-García, J. Martín Nuñez, Bojana Zegura, Alja Stern, Katja Kolosa, Iza Roman, Teobaldo E.Torres and Gerardo F. Goya. Summited